Low-Frequency Oscillations of the Solar Atmosphere

A thesis submitted for the degree of
Doctor of Philosophy

by

R. T. James M^{c}Ateer, M Sci. (QUB 2000)

Faculty of Science and Agriculture

Department of Pure and Applied Physics
Queen's University Belfast
Belfast, Northern Ireland

2003 November 14

‘ I’m not the only one,
Staring at the Sun,
Afraid of what you’d find,
If you took a look inside.’
–Staring at the Sun, U2

For Mum and Dad

Acknowledgements

To try to thank everyone who has helped me in writing this thesis would be folly. I've had the best support possible - financially, scientifically and socially.I've been exceptionally lucky to have travelled to Zambia to watch the solar eclipse in 2001, to have been all over the USA, west coast to east, and to have visited several wonderful Mediterranean Islands. This thesis is the result of three years hard graft of mine, and several more years of other people, not to mention nearly £60,000 (thats about £400 per page, so although I am aware that some people may not read past this page, enjoy every single one you do read). More importantly, everyone has helped me in a multitude of ways, some of which they themselves may never be aware of.

So, to Mihalis and Francis - your continued financial support, scientific input, and, most importantly, the knowledge to just let me get on with it, were invaluable. To Peter - your enthusiasm is contagious, your knowledge of the subject area is expert, your eagerness to get me involved in so many projects overwhelming and your hospitality undeserved. I hope Emma and Whinger didn't mind me intruding.

To Dave and Shaun - despite my multitude of stupid questions ('no stupid questions, only stupid people'), your willingness to drop your own work to help me is a quality above and beyond that required of office mates. I can only hope I was as much help to both of you in your work. Good times in Lusaka, Santorini, Mallorca, Big Bear, Sacramento Peak, Washington DC, and New York will not be forgotten. Along with Gerry, Gary, and Dermot, you've all had to suffer 'other James' more often than most. I think we managed to solve all the problems of the world over a few pints of the black stuff (Arthur, you are the one true genius). To Cathy, Colin, Darko, Carrie, and others - thanks for the many discussions (arguments?) and your continued ability to play 'James wins' in the face of adversity.

To Robert and Thanassis - why anyone would ever want to be a computer systems administrator is beyond my comprehension. My computer skills are all the more better for your ability to explain complicated procedures in simple language.

To my aunts and uncles, to Joanna, Pamela, Rhonda, and others housemates during my undergraduate years, to members of the APS past and present, to my old school teachers (especially Mr McNeice and Mr Headden, without whom I would not have ventured to university), to the APS lecturers who led me from physics to astrophysics,

to all the members of the QUOTC, to the Common room bar staff, John, Paddy, and Jim, to all the Friday night regulars - you all helped me in you own way. To the wonderful city of Belfast and amazing people of Ireland - I will return, whether you like it or not.

To Ann, Linda, and William - a person could not ask for better siblings. Finally to Mum and Dad - I can only hope you are as proud of me as I am of you.

I would be lying if, like many thesis I note, I said that I've been interested in astronomy since I was a boy, or that I've always wondered about the Sun. Truth is, I prefer to just sit back and see what develops. It's not a lack of ambition, more just the acceptance that, as I learned in QUOTC, even the best plans will inevitably fall apart. The ability to bend in the wind is what ensures success. I've been told I have a habit of always landing on my feet, and falling into interests more often than choosing them. It turns out these are not bad habits after all. I think I'll stick with them and see where they take me.

Abstract

This thesis presents detections of intensity oscillations in multi-wavelength image sequences of the quiet-Sun chromosphere, and interprets these oscillations in terms of various chromospheric wave-heating theories. Oscillations in network bright points (NBPs) are studied in the light of Ca II K_3 as a function of radial distance from the centre of each NBP. It is shown that low frequencies (1 – 4 mHz) tend to dominate, especially in the central portions, suggesting a magnetic component in any waves present.

Correlations between wavelet power density maps of light curves in four optical passbands is used to search for vertically propagating wave packets. In each NBP studied, observational evidence is found for transverse-mode magnetohydrodynamic (MHD) waves (1.3 mHz, 1.9 mHz) propagating upwards from the low- to mid- chromosphere, where they couple to longitudinal-mode MHD waves at twice the originally frequency (2.6 mHz, 3.8 mHz), which then shock in the high-chromosphere. There is also further evidence of other upward- and downward- propagating waves in the 1.3 – 4.6 mHz range.

An automated wavelet analysis routine is developed to compare, in frequency and duration, network and internetwork oscillations, in ultraviolet image sequences of the quiet Sun. The tendency of the network to contain lower frequencies (peak at 3.5 mHz, with an extended tail down to 1 mHz) is discussed in terms of transverse-mode MHD waves. In contrast, the internetwork contains frequencies around 4 mHz, with oscillations tending to contain a higher degree of spatial memory. These are interpreted as persistent flashers. The network tends to contain more oscillations below 3.3 mHz than the internetwork in the low-chromosphere, with this cross-over frequency increasing to 4 mHz in the upper chromosphere. However, below this cross-over frequency, the in-

ternetwork still contains a larger number of oscillations, but with short lifetimes. Both regions also contain a small number of non-recurring long-lived oscillations.

Contents

List of Tables

List of Figures

Publications

A list of publications resulting from work presented in this thesis is given below.

Refereed Publications

1. M^{c}Ateer, R. T. J., Gallagher, P. T., Bloomfield, D. S.,
Williams, D. R., Mathioudakis, M., Keenan, F. P.
Ultraviolet Oscillations in the Chromosphere of the Quiet Sun
2004, ApJ, **604**, in press

2. M^{c}Ateer, R. T. J., Gallagher, P. T., Williams, D. R.,
Mathioudakis, M., Bloomfield, D. S., Phillips, K. J. H., Keenan, F. P.
Observational Evidence for Mode-Coupling in the Chromospheric Network
2003, ApJ, **587**, 806

3. M^{c}Ateer, R. T. J., Gallagher, P. T., Williams, D. R.,
Mathioudakis, M., Phillips, K. J. H., Keenan, F. P.
Long-Period Chromospheric Oscillations in Network Bright Points
2002, ApJ, **567**, L165

Non-refereed Publications

1. M^{c}Ateer, R. T. J., Gallagher, P. T., Williams, D. R.,
Bloomfield, D. S., Mathioudakis, M., Keenan, F. P.
An Automated Wavelet Analysis Approach to TRACE Quiet Sun Oscillations
2003, Proc. '*SoHO* 13: Waves, oscillations and small scale transient events in the solar atmosphere. A joint view of *SoHO* and *TRACE*', ESA-SP **547**, in press

2. M^{c}Ateer, R. T. J., Gallagher, P. T., Williams, D. R.,
Mathioudakis, M., Phillips, K. J. H., & Keenan, F. P.
Detection of Propagating Waves throughout the Chromosphere in Network Bright Points
2002, Proc. 'SOLMAG: Magnetic Coupling of the Solar Atmosphere Euroconference and IAU Colloquium 188', ESA-SP **505**, 305

Chapter 1

Introduction

1.1 Solar Observations Throughout History

The Sun has always been the most important celestial object in our sky, and remains so to this day. All the major ancient civilisations worshiped a Sun god in some form; the Egyptians worshiped Re, the Babylonians worshiped Shamash, the early Greeks worshiped Helios and later Pheobus Apollo. The study of the Sun, planets and stars led the Greek philosophers to the first big step in astronomy of removing the earth from the centre of the universe, and suggesting it, along with all the other planets, revolved around the Sun. Since then solar observations have played a central role in many major scientific achievements throughout the ages

Galileo used the Sun as the most obvious light source to test his new instrument in 1610. The development of this instrument, the telescope, would be a big breakthrough for physics and would be the main experimental driving force behind other important seventeenth century scientific advances. Kepler's observations of the Sun and planets would later lead to Newton's *Principia* (1687) and hence the theory of Gravitation was born. In his investigation of colours Newton (1672) used sunlight directed through a prism to discover the colour constituents of white light. Wollaston (1802) used sunlight through a narrow slit to discover dark lines, which he incorrectly identified as the borders between colours. Fraunhofer (1817) used a more sensitive setup to discover hundreds of these dark absorption lines which would later be named after him (Figure 1.1).

He made the important step of identifying the lines as a property of the sunlight itself, and not a property of the earth's atmosphere as previously thought (although some lines are due to absorption by oxygen molecules in the earth's atmosphere). His labelling system of the lines (Table 1.1) based on relative strengths, is still used today to some extent (e.g., the sodium D doublet and ionized calcium H and K lines). The positions of these dark lines were soon equated with similar bright lines from earth based experiments. The jump to inferring the existence of certain elements in the Sun

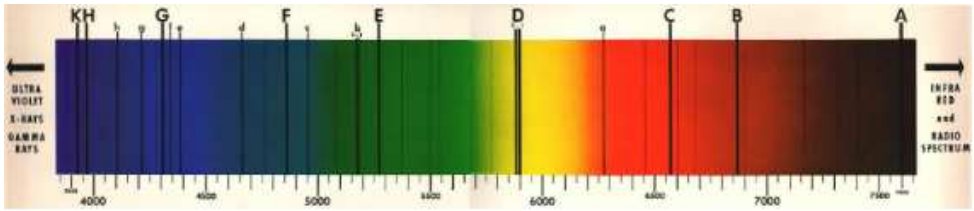

Figure 1.1: The Fraunhofer lines on the solar spectrum

Table 1.1: Identification of Fraunhofer lines. Most lines are of solar origin, but a few are due to absorption in the earth's atmosphere.

Fraunhofer Line	Element	Wavelength (Å)
A - (band)	O_2	7594 - 7621
B - (band)	O_2	6867 - 6884
C	H	6563
a - (band)	O_2	6276 - 6287
D - 1, 2	Na	5896 & 5890
E	Fe	5270
b - 1, 2	Mg	5184 & 5173
c	Fe	4958
F	H	4861
d	Fe	4668
e	Fe	4384
f	H	4340
G	Fe & Ca	4308
g	Ca	4227
h	H	4102
H	Ca	3968
K	Ca	3934

from their corresponding dark lines was soon made. Indeed in 1868 one such line led to the discovery of 'helium' (named after the Greek god Helios) in the Sun 30 years before it was discovered on earth. The following years saw many new scientific theories with solar observations at their centre: Kirchhoff's law for radiation was based on fully explaining the Fraunhofer lines; the explanation of the Doppler shift originated from studying the Fraunhofer lines at the solar limb; the solar eclipse of 1919 provided confirmation of Einstein's Theory of Relativity.

The start of the twentieth century also saw the realisation of quantum physics and the atom. These theories would explain the origins of the dark Fraunhofer lines. The

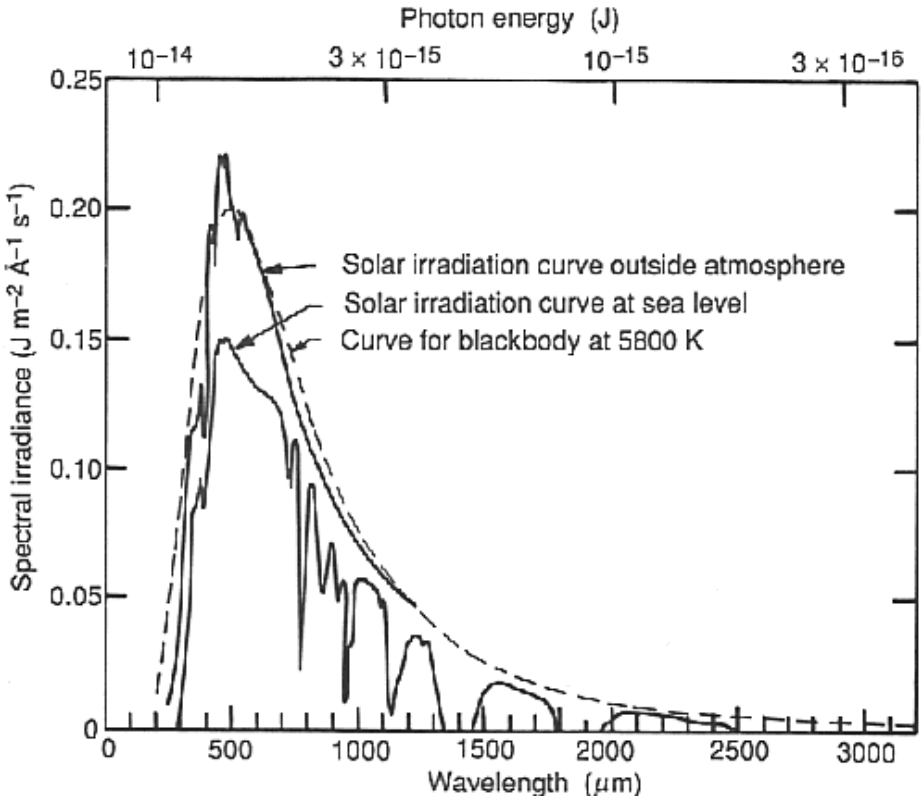

Figure 1.2: A blackbody curve at a temperature of 5800 K is overplotted on the solar irradiance curve.

continuous solar spectrum was explained by Planck (1900), and further by Einstein (1905), by approximating the solar surface (photosphere) to a black body at a temperature of 5800 K (Figure 1.2). Bohr (1913), using Planck's ideas and Rutherford's atomic model, explained the atom in terms of discrete electrons orbit, where photons of light were emitted when any electron jumped from one orbit to another. Radiation from the photosphere with exactly the right amount of energy could be absorbed by an electron, exciting it to a higher orbit. The 'flash spectrum' viewed during the initial stages of an eclipse could be explained as the re-emission of light as the electron decays to the lower orbit. Viewed against the brighter solar surface this would normally appear as dark lines in the solar spectrum. In the last few decades, the role of solar observations has moved into new areas. It still has a vital role to play in astronomy, as our only spatially resolvable star, in physics as the most stable and readily available example of plasma, the fourth state of matter, and in the commercial areas of military and communication.

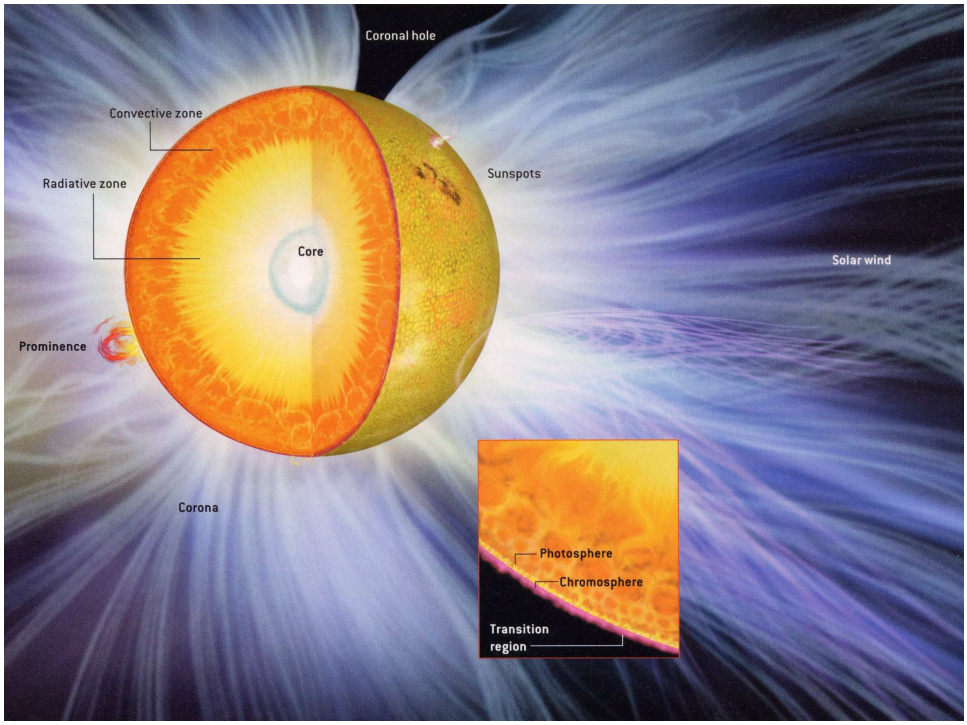

Figure 1.3: A 3-dimensional view of the Sun showing the interior, photosphere, chromosphere and corona (Scientific American 2003)

1.2 The Solar Atmosphere

The visible surface of the Sun is a thin layer of plasma known as the photosphere, denotes the top of the solar interior (Figure 1.3) and is the depth limit of direct observations. As such the photosphere is best defined using optical depth, τ,

$$\tau_\lambda = \int_{-\infty}^{z} a_\lambda dz \ , \tag{1.1}$$

where a_λ is the extinction coefficient at a wavelength λ and z is a depth coordinate such that $z \rightarrow -\infty$ outside the Sun. The optical depth is essentially the number of mean free paths along the line of sight. For a large τ, photons are absorbed and re-emitted numerous times along the line of sight, and so the plasma is described as optically thick. This applies to the deep lying layers of the Sun. Photons originating in the core pass through the radiative and convective zones, with the respective transport mechanism dominating in each zone, before reaching the photosphere (Figure 1.3). The photosphere has

a small τ, so most photons can travel directly to earth without being absorbed. The common definition of the photosphere is the layer from which the bulk of the visible photons are emitted, $0.1 \leq \tau_\lambda \leq 3.0$. As optical depth is a function of wavelength, it is reasonable to refer to the visible photosphere, the infrared-red photosphere, *et cetera*. Hence for the Sun, where the majority of photons are emitted in the visible wavelength, the photosphere is often defined as the layer where light emitted at 5000 Å (green) has an optical depth of 2/3, ($\tau_{5000} = 2/3$). The optical opacity of the photosphere and upper solar interior is mainly due to the negative hydrogen ion, where the second electron is only loosely attached. A photon with a large range of energies can hence remove the electron by absorption.

Above the photosphere the conditions change rapidly (Figure 1.4). Moving up through the chromosphere the electron density drops off, while the temperature drops to a minimum of 4200 K then gradually increases again. At a height of about 2000 km above the photosphere the electron density decreases sharply, and temperature increases dramatically from 25,000 K to a coronal temperature of 10^6 K in a transition region only a few hundred kilometers thick. This layer acts as an interface between the cool chromosphere and the hot tenuous corona. The corona, only viewable from earth when the photosphere is blocked out by a total eclipse or coronagraph, extends out though the solar system past Earth and on to the gas giants.

By careful comparison of atomic data with modelling of the solar atmosphere it is possible to estimate the height of formation of the Fraunhofer lines (Figure 1.4). The VAL model (Vernazza, Avrett, & Loeser 1981) is the most widely used and complete model of the origin of the absorption lines. This model is derived by semi-empirically inverting the observed extreme ultraviolet (EUV) line intensities. The cores of the stronger lines (Balmer lines, ionized calcium and magnesium) form mostly in the chromosphere, whereas weaker lines (e.g., G-band) originate from the low chromosphere/photosphere. The transition region mostly emits in ultraviolet (UV) wavelengths below 2000 Å, which is strongly absorbed by the earth's atmosphere. The corona has

increased UV, EUV and X-ray emission due to its high temperature. However the corona also emits a pair of visible continua, the K and F coronae. The low-intensity K corona, which dominates nearer the Sun, is due to electron scattered light. Doppler broadening due to the fast motion of the electrons removes the Fraunhofer lines from this continuum and polarizes the light. These scattering electrons must have extremely high temperatures ($\sim 2\times10^6$ K). The F corona comes from light scattered by dust particles and does contain the Fraunhofer lines. Several optical lines which could not be attributed to any element known on earth were detected in the eclipse of 1869. They were attributed to a new element, 'coronium'.The brightest lines were the green line (5303 Å) and the red line (6374 Å), with a few dozen fainter lines also discovered. The actual source of these was finally explained by Edlin (1942) and Grotian (1939) as due to forbidden transitions in highly ionized iron (Fe XIV and Fe X respectively). The high temperatures necessary to create these ionisation states, and the low densities to ensure the forbidden transition from the metastable states, provided further evidence of the extraordinary conditions in the corona.

1.3 The Fraunhofer Lines

1.3.1 Photospheric Lines

By the equation of radiative transfer,

$$\frac{dI_\lambda}{dx} = J_\lambda - K_\lambda I_\lambda \ , \tag{1.2}$$

the change in intensity, I, at any wavelength, λ, over a distance, *x*, is dependant on two processes, absorption and emission. The *absorption coefficient*, K_λ, is essentially the fraction of energy removed from a beam, either by absorption or scattering, per unit length. The *emission coefficient*, J_λ, is a measure of the amount of energy added to the

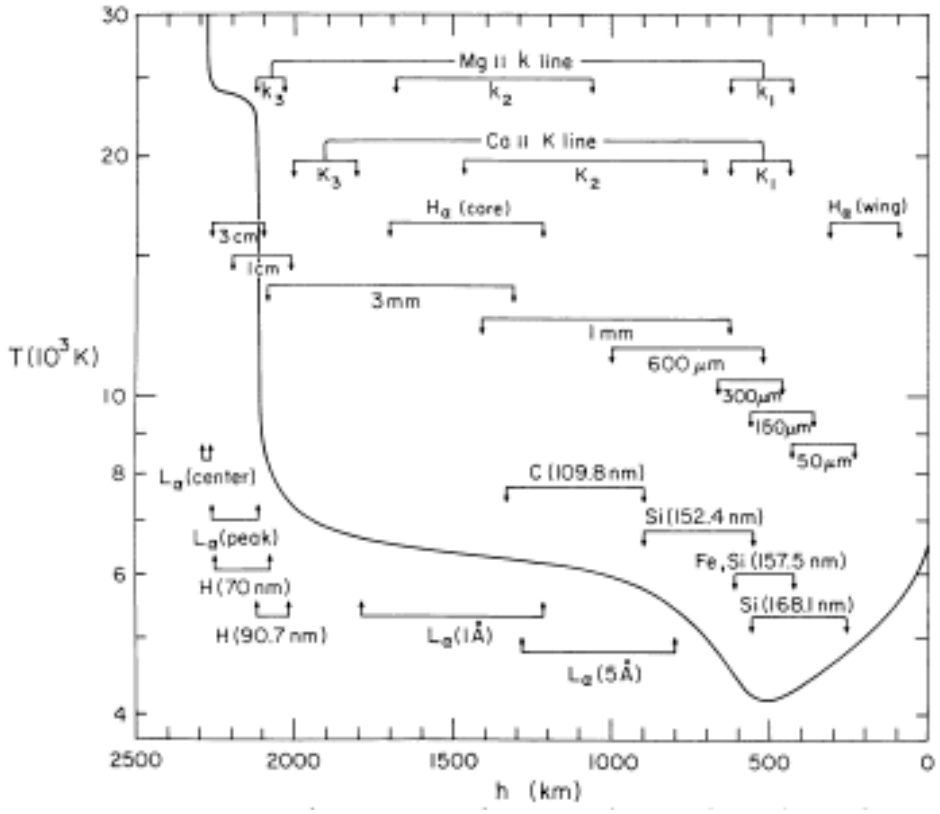

Figure 1.4: Temperature stratification of the quiet Sun. Heights of formation of several Fraunhofer lines are indicated. (Vernazza, Avrett, & Loeser 1981)

beam. The *source function*, S_λ, is then the ratio of emission to absorption,

$$S_\lambda = \frac{J_\lambda}{K_\lambda} \, . \tag{1.3}$$

In an ideal situation, where the atoms and photons of a gas are completely interacting, the Sun can be equated to a black body and hence the source function can be equated to the Planck function. However for the Sun, where some radiation escapes, this can only be achieved through the local thermodynamic equilibrium (LTE) approximation. Here the source function is approximated to the Planck function at the local temperature value. This is equivalent to the 'grey atmosphere' approximation where the absorption coefficient is independent of wavelength. The departure of the solar continuum curve from that of a black body (Figure 1.2) is due to the fact that the absorption coefficient is dependent on wavelength. For larger absorption coefficients, radiation is emitted from

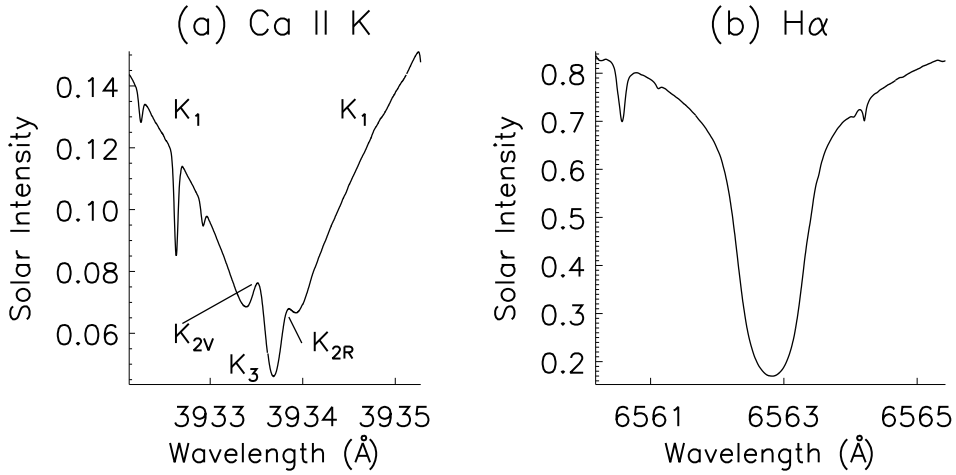

Figure 1.5: Line profiles of (a) Ca II K and (b) Hα. The K_3 core, K_2 peaks, and K_1 wings of the Ca II K are also noted in (a). The solar spectrum was obtained from the BASS2000 database and is normalised to continuum intensity.

higher in the atmosphere, where the temperature is cooler (i.e., as far up as the temperature minimum). This applies to the wavelengths of the Fraunhofer lines. Conversely for other parts of the spectrum, radiation comes from lower in the atmosphere where the temperature is hotter. As a result of this temperature difference the total flux emitted from the Sun in the Fraunhofer lines is lower than the continuum, hence the lines appear dark.

1.3.2 Chromospheric Lines

Although this simple explanation works well for weak and medium strength lines, as well as for the wings of stronger lines, the cores of the stronger lines must be explained differently. These lines are formed above the temperature minimum in the mid and high chromosphere (Figure 1.4). At these increased temperatures, the local temperature, describing the speeds of atoms and ions, can be several hundred degrees higher than the the radiation temperature. Hence the source function cannot be equated to the Planck function and the LTE approximation cannot be assumed. Lines here fall into one of two categories, either photoelectrically or collisionally controlled. The Balmer Hα line is

a good example of a photoelectrically controlled line. As such, the Hα line strength is dominated by photon excitations, and hence is governed by radiation from the photosphere, rather than the local temperature. Moving out from the photosphere, the source function steadily decreases, resulting from the increasing amount of radiation escaping into space (and hence decreasing emission coefficient). The line profile of Hα (Figure 1.5b) is purely in absorption at line centre (formed around 1500 km) and moving away from line centre corresponds to moving down through the atmosphere, where the emission coefficient, and hence source function, is higher. The ionized calcium (Ca II) H and K lines are good examples of collisionally controlled lines. Here the line is dominated by electron collisions with the atom and hence reflects the local temperature. As the temperature increases moving out through the chromosphere, the source function also increases (due to increased emission). Around a height of 1900 km the source function decreases again, due to scattering. Hence the line core, denoted K_3, is formed at 1900 km, the self reversed peaks on either side (K_2) are mid-chromosphere, and the line wings (K_1) are formed around the temperature minimum (Figure 1.5a).

1.3.3 Magnetograms

Magnetic fields exist throughout the solar atmosphere and can be imaged and measured using the Zeeman splitting of Fraunhofer lines. The Zeeman splitting comes from the interaction of the external field with the magnetic field created by the electron motion, resulting in a small positive or negative energy transfer to the photons emitted. As such, a single Fraunhofer line is split into two components, with the separation proportional to the field strength (discussed further in Chapter 3). Iron is the most popular choice for magnetograms, imaging the photospheric magnetic field, but other Fraunhofer lines can also be used to image magnetic fields throughout the solar atmosphere. The splitting increases linearly with wavelength, giving obvious benefits from imaging in the red and infrared wavelengths. Solar magnetic fields are most conspicuous as sunspots in white light images, but smaller scale magnetic features can

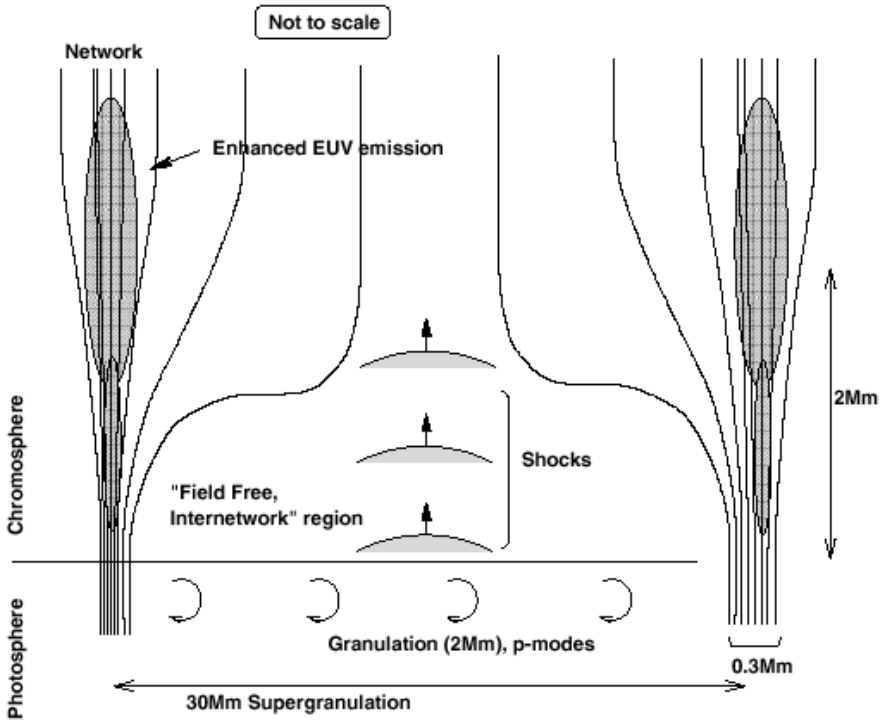

Figure 1.6: Diagram of the magnetic canopy effect as the field lines spread out. When the field lines from neighbouring network regions meet, the entire atmosphere is magnetic. Also shown are p-modes and the formation of acoustic shocks, discussed in Chapter 2. (Schmieder 2001)

also be viewed in the wings of Hα or line centre of the G-band (the molecular band head of the CH molecule). Typically sunspots have a field strength of 3000 G, and the smaller structures around 1000 G. These structures are in pressure balance with the surrounding environment, therefore the gas pressure inside must be smaller than the surrounding atmosphere, as the magnetic field exerts an additional pressure. Hence the structures are confined by the surrounding gas pressure and the photosphere is locally depressed within. For sunspots this is viewed as the Wilson depression. To compensate for the reduced gas pressure in the upper atmosphere the magnetic structures fan out (Figure 1.6). Eventually around the high chromosphere neighbouring structures meet, and the entire atmosphere is magnetic (Kopp & Kuperus 1968). Recent work by Schrijver & Title (2003) question the validity of this type of canopy. They suggest an alternative whereby field lines from the network connect with weaker fields in the nearby internetwork.

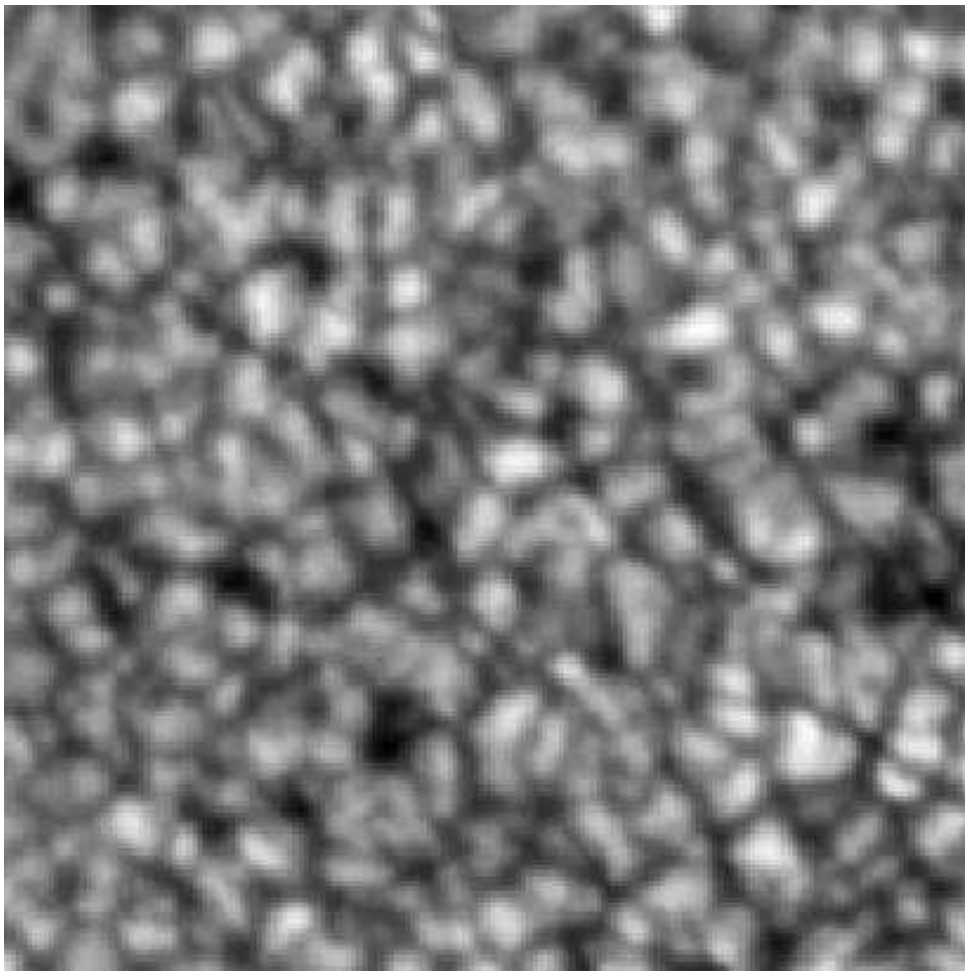

Figure 1.7: Granulation of the solar photosphere taken by the Dunn Solar Telescope, Sacramento Peak. This image, taken in a broad band visible light filter, covers an area of $30''$ by $30''$ on the solar disk. Typically, granules have a diameter of $\sim 1.5''$, corresponding to 1100 km

1.4 Photospheric Features

1.4.1 Granulation

Viewed in white light or in the wings of strong Fraunhofer lines the photosphere is covered in an irregular polygonal pattern known as granulation (Figure 1.7). The granular formation is due to the convective motion of the gas in the sub-photospheric layers, with the bright centre as upward flows and the dark lanes as downward flows. This overturning fluid carries heat bodily to the solar surface. As the hot opaque gas approaches the photosphere it is exposed to the interstellar vacuum, cools suddenly and

becomes transparent. This loss in energy corresponds with a rise in density and the vertical motion is decelerated and diverted into a horizontal motion. Further radiation of energy leads to further increases in density and eventually gravity pulls the parcel back down, along the intergranular lanes. In response to this, hot gas flows up to replace it, and so the convective cycle is complete. This convective flow is dominated by the cooling at the photosphere. The increased density at the bottom of the convective zone, 10^6 greater than at the photosphere, means the acceleration of convective flow here is 10^6 times less than at the photosphere. This is unlike normal convection (e.g., boiling water), where the top and bottom of the flow contributes equally.

Granules vary in size from 150 km (current ground based limit of observation) to 2500 km, with the majority around 1100 km diameter. Ground based observations require careful selection of observation sights, using realtime frame selection (taking a burst of hundreds of images and selecting the best images) or by speckle interferometry. The convective motion exhibits vertical flows (measured by Doppler shifts) of around 2 km s^{-1} peak to peak. The centre of the granules are typically 30% brighter than the intergranular lanes, which corresponds to $\sim$400 K temperature difference by the Stefan-Boltzmann law. Granules are born from fragments of other larger granules or from the merging of smaller granules. After expansion, they die either by fragmentation, merging, shrinking or dissolution. and have a typical lifetime, birth to death, of around 8–20 minutes (Spruit, Nordlund, & Title 1990).

Larger scale convective cells have been the topic of much debate (Hathaway *et al.* 2000). A second, larger, supergranular cell was discovered by Hart (1954) and later associated with convection by Leighton, Noyes, & Simon (1962). It was discovered in the Doppler shifted velocity images of Fraunhofer lines. These images suggested horizontal velocities parallel to the surface of around 0.4 km s^{-1}, leading to large cells of around 30,000 km with a lifetime of about one day. Recent work by Hagenaar, Schrijver, & Title (1997) suggest this may be overestimated, and propose a typical cell diameter of around 15,000 km. These larger cells carry the smaller granules like flotsam

carried along a river, and hence the horizontal flows can be viewed by measuring the granular motion. This motion also carries magnetic flux tubes, which meet at the supergranular boundaries and fall. Some flux remains which moves along the boundaries to vertices, where the downflow is concentrated into small plumes, often with a vortex motion. Due to this concentration of magnetic flux, supergranular cells are spatially related to high chromospheric structure (Section 1.5.3), but theory places their origins below that of granulation. Simon & Weiss (1968) suggested different cell sizes on the Sun are each excited by various ionisation/recombination layers. Granulation was attributed to recombination of hydrogen at a depth of 1,000 km below the surface and supergranules attributed to recombination of helium at a depth of 15,000 km. Two further cells sizes were predicted, a 5000 km cell due to recombination of helium at 5,000 km depth and a much larger cell due to recombination of metals at 200,000 km depth (the base of the convection zone). These were later found as *mesogranules* (November *et al.* 1981) and *giant cells* (Beck, Duvall & Scherrer 1998). The mesogranular flow can be observed as regions of converging and diverging horizontal flow of around 5,000 to 10,000 km. Bright, long-lived, rapidly expanding granules, normally with dark centres, are preferentially found in upflowing mesogranular centres, where horizontal flows diverge. Small, faint, short-lived granules are preferentially found in downflowing mesogranular boundaries, where horizontal flows converge. New observations and simulations suggest cells are more 'pancake shaped' with structure depth to around 1/4 to 1/2 of their diameter (Simon 2001). As such, granules are formed around 100 km depth and supergranules around 5000 – 10,000 km. Some authors (e.g., Roudier *et al.* 1999) argue that the the fact that mesogranular parameters (e.g., velocity, lifetime) are dependant on the chosen filters suggests that mesogranulation may purely be an artifact of the data reduction. Hathaway *et al.* (2000) have further suggested that mesogranules are simply large granules (or small supergranules) and giant cells are large supergranules. The driving mechanism behind these large convection cells, and factors determining their size (or various sizes) remain unanswered.

1.4.2 Magnetic Structure

The sunspots which blemish the solar surface are areas of high magnetic flux, and can be classified according to their appearance, complexity and magnetic structure. They are cooler than the surrounding photosphere so appear dark on images taken in the visible continuum. A record of the monthly total number of sunspots led to the discovery of the well known eleven–year active–cycle of the Sun. Sunspots are part of a group of larger areas known as *active regions*. Active regions comprise all phenomena associated with emergent flux and many active regions exist without producing sunspots. Sunspots and active regions generally occur at low latitudes, whereas shorter lived, smaller scale, magnetic areas known as *ephemeral* active regions are evident over a higher latitude spread. The organisational quality of the supergranular flow tends to concentrate the magnetic field into the cell boundaries. But the finite efficiency of this process means there is some remnant field. This left over field eventually reaches an equilibrium with the convective and turbulent motions and this creates a third scale of magnetic field known as the *intranetwork* or *internetwork*, studies of which can only be achieved with deep magnetograms which have high spatial resolution and long exposure times. Unfortunately the small structures also evolve over short timespans so further progress in this field will require achieving the desired spatial resolution without trading off temporal resolution.

Images in the cores of weak lines, especially the G-band, show small features associated with increased magnetic field. A pattern of strings of small bright points can be found strung along intergranular lanes. These *filigree* can be found in the quiet Sun at supergranular boundaries, and in active regions as *faculae*. Each bright point can be spatially associated with a magnetic element of nearly the same size. Magnetic tubes of around 1000 G are concentrated by compression of converging granules in a diameter of around 400 km. This results in a large flux of 10^{17}Mx. Because of this strong interaction with energetic granules, filigree are unstable with a mean lifetime of around five minutes, and usually appearing in a dark junction of several granules, concentrat-

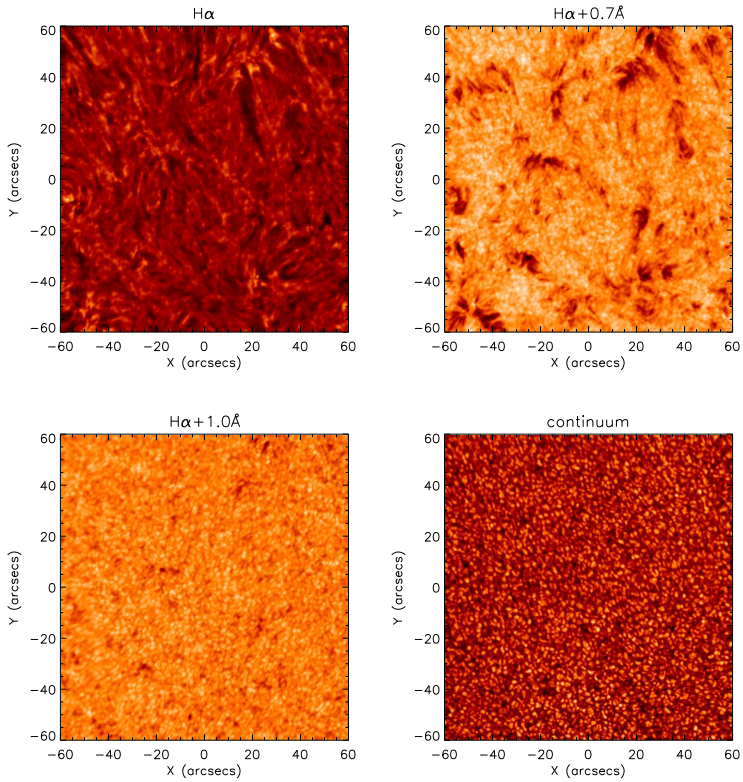

Figure 1.8: Imaging throughout the solar atmosphere. All images were taken by the Dunn Solar Telescope, Sacramento Peak and are of the same region at disk centre with a field of view of 120″ by 120″. Images in the core of the Hα line are chromospheric. However moving away from disk centre, images are increasingly photospheric. At 1Å into the blue wing, granulation dominates the images, similar to images taken in the continuum

ing the field further. The gas inside the filigree is heated by the gas outside, due to its higher pressure. A combination of this along with the fact that deeper layers are viewed creates the brightness. The strong correlation with magnetic elements means filigree can be used to track chaotic flux. Magnetic waves, transverse to the field, are generated by this chaotic motion at the top of the convection zone and move up through to the corona with an exponential growth of amplitude. Dissipation of energy by these magnetohydrodynamic waves is suggested as a possible coronal heating mechanism.

1.5 Chromospheric Features

1.5.1 Fine Structure

The most useful lines for imaging the chromosphere are Hα and Ca II H and K. As explained in Section 1.3.2, moving from line centre to the wings of these lines corresponds to imaging different heights in the atmosphere (Figure 1.8). Images in K_3 show a series of bright and dark patches over the surface. The bright features are known as *mottles*. These are areas of large brightness contrast which link together to form a quasi-regular pattern around and above supergranules. The larger features are coarse mottles, also known in literature as *flocculi*. They combine to form the chromospheric network (Section 1.5.3). Each mottle consists of several bright fine mottles, around 7000 km long and 700 km in diameter. Images in Hα contain additional contribution from higher levels (due to higher excitation energy). In Hα line centre, fine mottles can be bright (low-lying) or dark (height$\sim$ 3000 km), the latter sometimes showing fragmentation. In the wing of this line (Figure 1.8), fine mottles are always dark. *Rosettes* are formed when alternate dark and bright fine mottles radiate from a common centre, where the common centre makes up part of the network. Typical fine mottles have a lifetime of 12-20 minutes. They are sites of upward and downward motions which can be regarded as cylinders less than 1000 km thick, with a temperature in the range of 5000 – 15000 K. The dark/bright contrast is due to an increase in gas pressure. *Spicules* are limb structures of $\sim$10,000 K, up to 1500 km across which extend 10,000 km into the corona, with a typical upward velocity of 20 km s^{-1}. This upflow could fill the corona in three hours, and so requires a mass flow back down into the chromosphere. Often spicules, and the downflow corresponding to them, are attributed to mottles on the limb. In the centre of each cell smaller features can be found. The Hα violet wing shows small (1000 km) dark features associated with upward flow. In Ca II lines, *bright grains* are found which increase and decrease in brightness periodically over a few minutes. In the network, these are found to be spatially coherent with small mag-

netic elements which collide and reconnect. The brightness may be due to heating after magnetic reconnection, where magnetic flux is turned into heat (Chapter 2).

1.5.2 Active Regions

Across the solar disk, bright *plages* are found in a granular structure in the vicinity of active regions. These are areas of higher temperature and density than the surrounding areas, caused by the enhanced magnetic field of the active region. Fine dark *fibrils* are found arranged in a radial or spiral pattern around sunspots, with a clockwise rotation in the southern hemisphere, and a counter-clockwise pattern in the northern hemisphere. These are much longer ($\sim$20,000 km) than quiet-Sun mottles. The fibrils have been shown to connect areas of opposite magnetic polarity, and are aligned with the local magnetic field. On the other hand, long dark *filaments* mark lines of magnetic inversion. They can be found winding throughout active regions, often with one end close to a sunspot. An active region starts as a brightening in the network mottles, followed by plage filling in the network cell. Sunspots and flares follow within a few days. Newly emerging bipolar regions are connected by low-lying arch filaments. The arch filaments bring up the denser material from the lower atmosphere. At the ends of these loops the material is pulled back down, due to gravity. This is viewed as small bright *Ellerman bombs* which show up in the wing of Hα (with the rapid changes associated with quiet and active region chromospheric fine structure it is important to remember many of the structures will be Doppler shifted to the wings of absorption lines). Shearing and twisting of flux tubes in and around active regions also sets up currents along field lines. On a larger scale, the differential rotation of the Sun induces an extended current system. A third system of currents is due to the large conductivity of the atmosphere such that field structures cannot relax to a current free state.

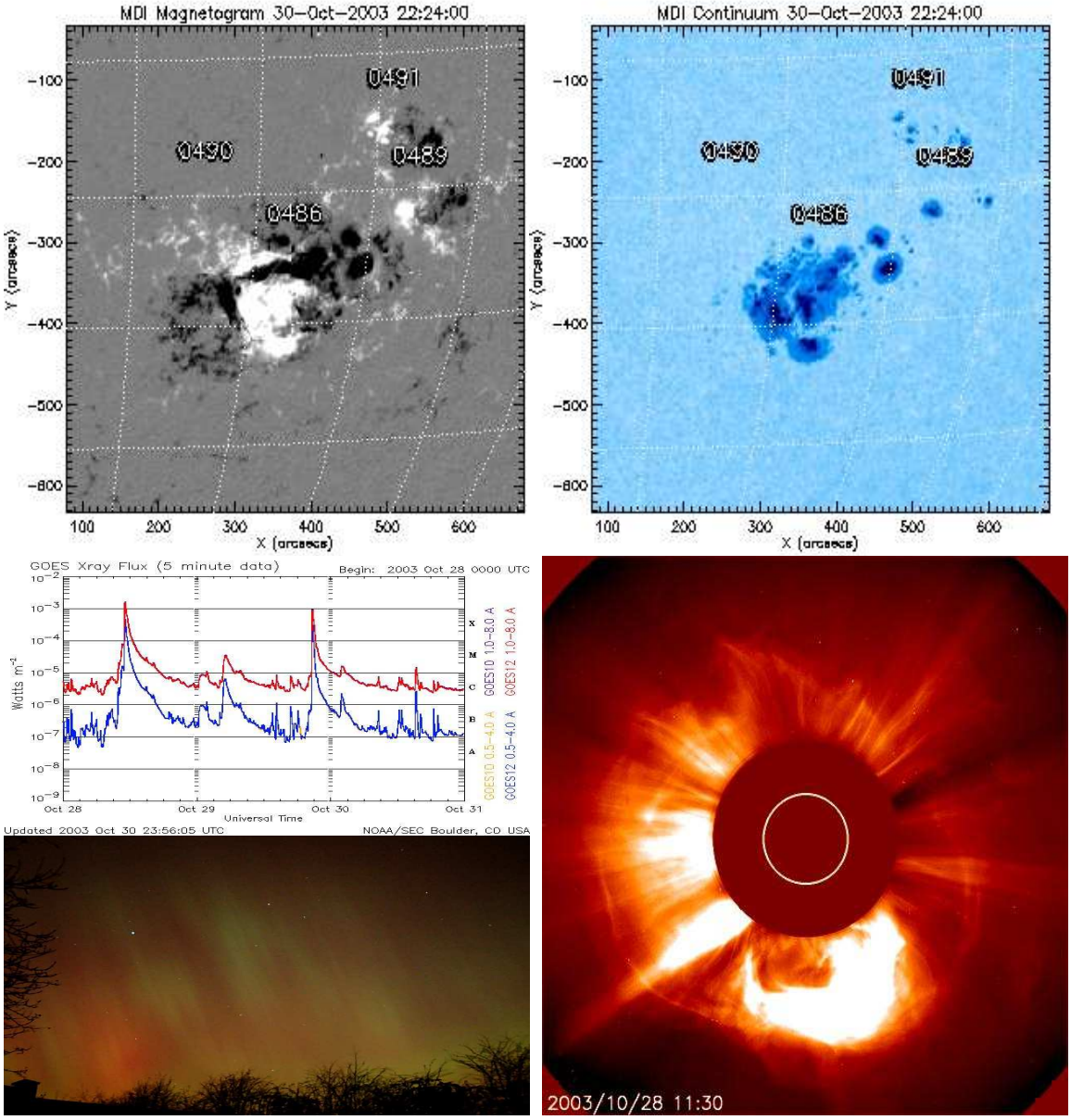

Figure 1.9: Top row[1]:*SoHO* MDI magnetogram and continuum image of active region NOAA 10486 - the magnetic mixing around (350,-350) means this region was assigned a $\beta\gamma\delta$ classification. Middle left[2]: *GOES* X-ray flux. The large X-class (X17.2) flare on 28 Oct 2003 came from NOAA 10486. Middle right [3]:*SoHO* LASCO C2 image of the CME associated with the X17.2 flare. Bottom left[4]: Aurora in Glengormley, N.Ireland as particles from the CME slammed into the earth's atmosphere.

[1]Images from *SoHO* and courtesy of Peter Gallagher. (http://http://beauty.nascom.nasa.gov/arm/)
[2]Data from Space Environment Centre. (http://sec.noaa.gov/)
[3]*SoHO* image. (http://sohowww.nascom.nasa.gov/)
[4]Image courtesy of A. Fitzsimmons.

The magnetic field above active regions extends into the corona, where reconnection between twisted field lines can lead to solar flares (Priest & Forbes 2002), and occasionally to coronal mass ejections (CMEs). When earth-directed these can cause severe damage to satellites, astronauts and power grids, and cause the aurora in the earth's atmosphere. Figure 1.9 shows how the Michelson Doppler Imager (MDI; Scherrer *et al.* 1995) and Large Angle Spectroscopic Coronagraph (LASCO; Brueckner *et al.* 1995) on board the Solar and Heliospheric Observatory(*SoHO*; Fleck, Domingo, & Poland 1995) can be used to study these explosive events.

1.5.3 Chromospheric Network

The chromospheric network is highly co-spatial with the photospheric supergranulation and dynamic over a timescale of hours. Evolution occurs by the appearance of new field in the centre, migration to the boundaries, further migration along the boundaries and eventual disappearance (Schrijver, Hagenaar, & Title 1997; Hagenaar *et al.* 1999). The cell is dominated the appearance of many small, upflowing centres of magnetic field, known as the internetwork (Section 1.4.2). Lites, Rutten, & Kalkofen (1993) point out that the network viewed is not a mosaic of regular cells, instead it is a system of irregular patterns without actual well-defined insides. As such, the use of the terms 'intranetwork', along with 'cell boundary' and 'cell interior', are not appropriate. However the use of these terms is still in common practice. On the granulation scale, granular buffeting moves these magnetic regions in a random walk. Across the supergranules the flow patterns have a longer lifetime, hence the magnetic regions are eventually collected in the network and move along it. Along the network these regions may interact; opposite polarities may meet and reconnect, and so vanish; some may split into two or more regions (fragmentation); two regions of the same polarity may meet and merge.

The precise co-spatiality with the photospheric magnetic network can be used to

find the polarity of the network regions in the chromosphere. They tend to be mixed in the quiet Sun and unipolar at the poles, near active regions, or near previous active regions. The K index (the strength of the central K_3 line in a 1 Å band) is a measure of the intensity of regions in the chromosphere. In quiet regions the K index increases linearly with magnetic flux density. In the network regions (highly magnetized) the K index increases with magnetic flux density with an index less than unity. This is an indication of these regions spreading out horizontally with increasing height. (Figure 1.6). Eventually the field lines form a canopy over internetwork regions at a height of 2000 km (Section 1.3.3).

1.6 The Chromospheric Heating Problem

The increase in temperature in the chromosphere, transition region and corona must be explained by some non-radiative form of energy. If radiation was the only energy being transported through the atmosphere, the temperature should decrease further out from the core, as more energy is escaping. An extra heating mechanism must exist, which will provide energy for atoms to become excited and decay. This process of absorption and decay acts as a thermostat for the lower chromosphere, and is mainly provided by hydrogen atoms (providing the red chromosphere during eclipse totality in Hα). When the supply of hydrogen atoms runs out the temperature increases sharply, marking the transition zone. A further thermostat is provided in the corona by the large number of highly ionized atoms. This provides a second temperature plateau.

One of the most controversial areas in solar physics at the moment is the necessity of the existence of a temperature minimum at all (Figure 1.10). The rise in temperature around 500 km is a direct result of the VAL model (Vernazza *et al.* 1981) and later in the FAL model (Fontenla, Avrett, & Loeser 1993) to explain the chromospheric emission in EUV lines and was generally accepted for many years. Ulmschneider (1970) suggested short period ($\sim$ 30 s) waves shocking in the chromosphere to explain this,

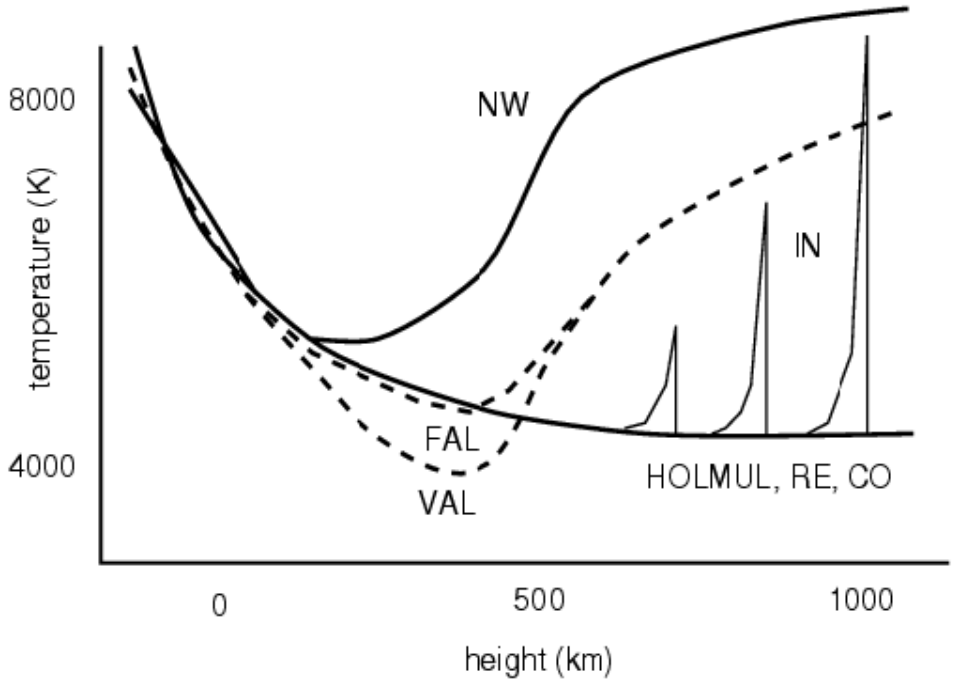

Figure 1.10: Depiction of temperature stratification of various models of the lower solar atmosphere. Both the VAL and FAL models require a rise in temperature to account for excess EUV emission in the internetwork (IN). The HOLMUG, RE and CO models suggest a cool atmosphere. The network (NW) still requires a (deeper) temperature rise. (Rutten 1998)

but no observation evidence could be found. In contrast, previous stellar-like classical radiative equilibrium (RE) models (e.g., Gustafsson & Jorgensen 1994), and the HOLMUL model (Holweger & Müller 1974) showed no need for a temperature rise.

Modelling of internetwork grains (Carlsson & Stein 1992; 1995; 1997) suggested the temperature rise was purely a inversion technique artifact. They suggested that acoustic shocks in the internetwork may intermittently heat the chromosphere, without significantly increasing the average temperature. However, at UV wavelengths, they may be sufficiently bright to as to require a temperature rise when inverted as in the VAL and FAL models. The idea of a cool atmosphere with intermittent shocks also agrees with models derived from the CO line formation (e.g., Ayres 1981). Other authors (e.g., Kalkofen, Ulmschneider, & Avrett 1999) question the validity of this model.

1.6.1 Network Heating

Although the Carlsson & Stein model explains the internetwork grains, it is still apparent the network requires an extra heating mechanism. Proposed heating mechanisms can broadly be divided into two categories, namely *alternating current* (AC) and *direct current* (DC). Direct current (DC) mechanisms involve current sheets with timescales longer than the dissipation time, whereby the energy stored in the magnetic field is directly dissipated. DC mechanisms can be further subdivided into those which dissipate energy by field aligned currents (Spicer 1991) and those where currents are perpendicular to the field (e.g., nanoflares - Parker 1988). AC mechanisms involve waves which are guided by the magnetic field and dissipated in timescales comparable to the period. These have three common factors, namely the generation, propagation and dissipation of waves. The various modes of waves and how they may influence the plasma through which they propagate are described in the next chapter (also see reviews by Rutten & Uitenbroek 1991; Rutten 1999).

1.7 Outline of this Thesis

The aim of the work for this thesis was to use multi-wavelength narrowband images of the chromosphere to search for the possible oscillatory signals of AC heating mechanisms. There are several reasons for specifically studying the chromosphere. From a theoretical perspective, it is the boundary between the interior (dominated by fluid motions and gas pressure) and the magnetically dominated corona. As an introduction to this background theory, Chapter 2 contains a summary of the equations which explain the various modes of waves possible in a stratified, magnetised plasma such as the chromosphere. A brief overview of the fundamental equations is provided, along with a description of wave propagation in homogeneous and inhomogeneous plasmas.

From an observational aspect, the chromosphere provides several optical Fraun-

hofer lines, and UV continuum. Chapter 3 contains a description of the experimental set-up used in an observing run at Dunn Solar Telescope / National Solar Observatory, designed to observe the same region of the quiet Sun in as many optical wavelengths as possible, whilst still maintaining a sufficiently high cadence. As the earth's atmosphere absorbs UV continuum, it is necessary to use data from space-based instrument to observe the Sun in this part of the electromagnetic spectrum. Hence Chapter 3 also contains a description of the *TRACE* spacecraft, and imaging in the UV.

Chapter 4 discusses novel image segmentation and statistical analysis techniques used to study oscillations in the chromospheric network imaged in Ca II K_3. Specifically the 'contour and contrast' technique is used to separate oscillations in network bright points from those of other solar (e.g., internetwork), or of non-solar (e.g., earth's atmosphere) origin. This work is extended to search for oscillations at several heights in the chromosphere in Chapter 5. Wavelet analysis routines are used to search for correlated oscillations across all frequencies, which may result from waves travelling through the chromosphere. This is used to test several chromospheric heating theories.

Chapter 6 uses an automated wavelet analysis technique to search for intensity oscillations in UV passband data. This extends previous Fourier analysis of this work into the time-localised domain. Differing oscillatory signals in the network and the internetwork at various atmospheric heights are found to be indicative of differing wave modes and heating mechanisms in these two regions. The recurrence of oscillations of various periodicities and lifetimes are discussed in terms of previous work.

Finally, Chapter 7 summarises the conclusions of this thesis, and suggests future directions of this project.

Chapter 2

Wave Heating of the Chromosphere

If the Sun did not have a magnetic field it would be as uninteresting a star as most night time observers believe it to be

- R. Leighton

The majority of solar structure and phenomena are a result of the interaction of the solar plasma with the magnetic field (Osterbrock 1961). Such interactions are governed by a set of equations known collectively as magnetohydrodynamics (MHD). These are a combination of the equations of electric and magnetic fields, and those of fluid dynamics. Using simple approximations and combining linearised versions of these equations leads to wave dispersion relationships which describe the behaviour of a plasma in a magnetic field. This chapter contains a brief summary of these equations and the properties of the wave modes which arise from them in both a homogeneous and inhomogeneous plasma.

2.1 Maxwell's Equations

The set of equations describing the behaviour of the electric field, **E**, magnetic field, **B** (actually **B** is magnetic induction but is commonly referred to as magnetic field in astrophysics), and current density, **j**, were first combined by Maxwell (1873). These are as follows. Firstly, Poisson's equation,

$$\nabla.\mathbf{E} = \frac{\rho^c}{\varepsilon_0} \ , \tag{2.1}$$

where ρ^c is charge density and ε_0 is the permittivity of free space. This states that a net charge will act as a source for an electric field. Secondly, Faraday's law,

$$\nabla \times \mathbf{E} = -\frac{\partial \mathbf{B}}{\partial t} \ , \tag{2.2}$$

which states that a change in magnetic field with time will produce an electric field. Thirdly, Ampere's law,

$$\nabla \times \mathbf{B} = \mu_0 \mathbf{j} + \frac{1}{c^2}\frac{\partial \mathbf{E}}{\partial t} \ , \tag{2.3}$$

which states that either a current, or time-varying electric field will produce a magnetic field. In this equation μ_0 is the magnetic permeability of free space, related to the speed of light, c, by,

$$c^2 = \frac{1}{\mu_0 \varepsilon_0} \ . \tag{2.4}$$

Under the MHD approximation, whereby plasma velocities, **v**, are much less than the speed of light, the second term on the RHS of Eqn. 2.3 is ignored. Finally, Gauss' law,

$$\nabla . \mathbf{B} = 0 \ , \tag{2.5}$$

such that there are no magnetic monopoles. In addition to the four Maxwell's equations above, Ohm's law states that, in a frame of reference moving with the plasma, the current density is proportional to the sum of the electric field due to the movement of the plasma ($\mathbf{v} \times \mathbf{B}$) plus the electric field which would act on it at rest, **E**, i.e.,

$$\mathbf{j} = \sigma(\mathbf{E} + \mathbf{v} \times \mathbf{B}) \ , \tag{2.6}$$

where σ is electrical conductivity.

2.1.1 The Induction Equation

The electric field can be eliminated between Faraday's law and Ohm's law to give,

$$\frac{\partial \mathbf{B}}{\partial t} = \nabla \times (\mathbf{v} \times \mathbf{B}) - \nabla \times \frac{\mathbf{j}}{\sigma} \ . \tag{2.7}$$

This reduces, by Ampere's law, to,

$$\frac{\partial \mathbf{B}}{\partial t} = \nabla \times (\mathbf{v} \times \mathbf{B}) - \nabla \times (\eta \nabla \times \mathbf{B}) \ , \tag{2.8}$$

where $\eta = 1/(\mu_0 \sigma)$ is magnetic diffusivity. By simple use of a vector identity, using Gauss's law, and assuming constant[1] η this further reduces to,

$$\frac{\partial \mathbf{B}}{\partial t} = \nabla \times (\mathbf{v} \times \mathbf{B}) + \eta \nabla^2 \mathbf{B} \ , \tag{2.9}$$

which is known as the induction equation. This states that a local change in the magnetic field is due to both convection and diffusion. The magnetic Reynolds number is the ratio of the convective to the diffusive term,

$$R_m = \frac{\nabla \times (\mathbf{v} \times \mathbf{B})}{\eta \nabla^2 \mathbf{B}} \ , \tag{2.10}$$

and is an indication of the coupling between the plasma flow and the magnetic field. This can simply be approximated to,

$$R_m = \frac{\mathrm{v}_0 l_0}{\eta} \ , \tag{2.11}$$

for length scale, l_0, and plasma speed, v_0.

For large R_m ($\gg 1$), as found in most astrophysical cases, the convective term dominates in Eqn. 2.9, and the field lines move as if they are frozen into the plasma (Alfvén, 1943) with typical timescale, $t_c = l_0/\mathrm{v}_0$. For small R_m ($\ll 1$), typically found in laboratory plasmas, the diffusion term dominates and flux 'leaks' with typical ohmic diffusion timescales then given by $t_d = l^2/\eta$. For typical solar photospheric values ($\mathrm{v}_0 \sim 10$ m s^{-1}, $\eta \sim 10^3$ m^2 s^{-1}), R_m becomes less than unity ($t_d \sim t_c$) for $l_0 \sim 100$ m, ohmic dissipation becomes important, and magnetic reconnection may occur.

[1] In fact η varies with both temperature and density, from $\sim 10^3$ m^2 s^{-1} in the photosphere to ~ 1 m^2 s^{-1} in the corona (Priest 1982).

2.2 Fluid Dynamics

This section describes the three basic equations of fluid dynamics. In each case the equation is initially stated in its *material time derivative* (D/Dt) form, and changed into the *partial derivative* ($\partial/\partial t$) form via,

$$\frac{D}{Dt} \equiv \frac{\partial}{\partial t} + \mathbf{v}.\nabla \ , \tag{2.12}$$

where $\mathbf{v}$ is plasma velocity as before.

2.2.1 Equation of Mass Continuity

The equation of mass conservation is,

$$\frac{D\rho}{Dt} + \rho\nabla.\mathbf{v} = 0 \ , \tag{2.13}$$

By use of a vector identity, Eqn. 2.13 may be expressed as,

$$\frac{\partial\rho}{\partial t} + \nabla.\rho\mathbf{v} = 0 \ . \tag{2.14}$$

This simply states that, at any point, the density increases if there is material flow into the region ($\partial\rho/\partial t > 0$ for $\nabla.\rho\mathbf{v} < 0$) and decreases with material flow away from the region (i.e., positive divergence).

2.2.2 Equation of Energy Conservation

The fundamental heat equation is given as,

$$\rho T\frac{Ds}{Dt} = -L \ , \tag{2.15}$$

where s is entropy per unit mass, and simply states that the rate of increase of heat is due to L, the net effect of all sources and sinks of energy. By using the first law of thermodynamics it can be shown that Eqn. 2.15 can be rewritten in a concise form,

$$\frac{\rho^{\gamma}}{\gamma-1}\frac{D}{Dt}\left(\frac{p}{\rho^{\gamma}}\right) = -L \ , \tag{2.16}$$

where p is pressure and γ is the ratio of specific heats (polytropic index). For a thermally isolated plasma such that no heat is exchanged ($L = 0$), Eqn. 2.16 reduces to,

$$\frac{D}{Dt}\left(\frac{p}{\rho^{\gamma}}\right) = 0 \ . \tag{2.17}$$

which may be expressed as,

$$\frac{\partial P}{\partial t} + \mathbf{v}.\nabla P - c_S^2\left(\frac{\partial \rho}{\partial t} + \mathbf{v}.\nabla\rho\right) = 0 \ . \tag{2.18}$$

2.2.3 Equation of Momentum Conservation

By Newton's second law the equation of motion may be written as,

$$\rho\frac{D\mathbf{v}}{Dt} = -\nabla p + \mathbf{j}\times\mathbf{B} + F_g \ , \tag{2.19}$$

where F_g is the force due to gravity (viscosity is neglected). Thus, the force per unit volume (LHS) is equal to the summation of forces given by a pressure gradient, a Lorentz force, and gravity. This equation connects the fluid motions to Maxwell's equations via the $\mathbf{j}\times\mathbf{B}$ term. By assuming a gravitational force of the form $F_g = -\rho g(\hat{\mathbf{z}})$ (where $\hat{\mathbf{z}}$ is the outward normal from the solar surface) this becomes,

$$\rho\frac{D\mathbf{v}}{Dt} = -\nabla p + \mathbf{j}\times\mathbf{B} - \rho g\hat{\mathbf{z}} \ . \tag{2.20}$$

By simple use of Ampere's law (Eqn. 2.3) and a vector identity, the Lorentz force

in Eqn. 2.20 reduces to,

$$\mathbf{j} \times \mathbf{B} = \frac{(\mathbf{B}.\nabla)\mathbf{B}}{\mu_0} - \nabla \frac{B^2}{2\mu_0} \,. \tag{2.21}$$

The first term on the RHS represents a force due to magnetic tension, parallel to **B**, which results from the curvature of the magnetic field lines. The second term on the RHS is a scalar magnetic pressure force. The plasma β parameter is the ratio of the the plasma pressure to this magnetic pressure and is given by,

$$\beta = \frac{2\mu_0 p}{B^2} \,. \tag{2.22}$$

So for $\beta > 1$ pressure dominates, whereas for $\beta < 1$ magnetism dominates.

When the plasma flow speed is less than the sound speed, Alfvén speed and free-fall speed, magnetohydrostatic equilibrium exists and the forces in Eqn. 2.20 balance. In a direction perpendicular to the field lines, **n**, and substituting for the Lorentz force from Eqn. 2.21, Eqn. 2.20 reduces to,

$$\frac{\partial}{\partial n}\left(p + \frac{B^2}{2\mu_0}\right) = 0 \,. \tag{2.23}$$

Define a thin flux tube such that the internal and external pressures are p_i and p_e respectively, such that the *total* pressure inside and outside the tube is the same, i.e.,

$$p_e = p_i + \frac{B^2}{2\mu_0} \,. \tag{2.24}$$

Hence p_i will be less than p_e, the internal mass density will also be lower than the external mass density, and (assuming thermal balance) the flux tube will rise. Thus magnetic buoyancy will cause magnetic flux tubes in the convection zone to rise to the surface.

2.3 Waves

Waves in a medium are the direct result of periodic perturbations. The basic modes of waves are classified by their restoring forces, which in a non-viscous, perfectly conducting plasma are gravity, pressure, and magnetism. As well as acting individually, these may act in three sets of pairs or all at once. This section contains a brief summary of the general dispersion relation for each mode of wave, followed by a qualitative description of the multi-force modes. For a more detailed description the reader is referred to any MHD textbook (e.g., Priest 1982, Choudhuri 1998) or Stein & Leibacher (1974).

2.3.1 Acoustic Velocity & the Klein Gordon Equation

Initially I will neglect the magnetic field, and concentrate on the effects of sound waves in a stratified atmosphere (i.e., set **B**=0). Assume a simple adiabatic expansion of the form,

$$p = A\rho^{\gamma}, \tag{2.25}$$

where A is a constant. Taking the gradient of both sides of this equation leads to,

$$\nabla p = c_S^2 \nabla \rho, \tag{2.26}$$

where the acoustic velocity, c_S, is given by,

$$c_S^2 = \frac{\gamma p}{\rho} = \frac{\gamma K_B T}{\mu m_p}\ , \tag{2.27}$$

where K_B is the Boltzmann constant, μ is the mean molecular weight, and m_p is the proton mass. Hence $c_S \propto T^{0.5}$ and varies from around 9 km s^{-1} in the photosphere to over 200 km s^{-1} in the corona.

Under hydrostatic equilibrium conditions, Eqn. 2.20 becomes,

$$\nabla p = -\rho g \hat{\mathbf{z}} \, . \tag{2.28}$$

Using the ideal gas equation, and for an isothermal medium stratified in the z axis, this can simply be integrated to obtain (Roberts 2003),

$$p(z) = p(0) e^{-\frac{z}{H}} \, , \tag{2.29}$$

$$\rho(z) = \rho(0) \frac{H(0)}{H(z)} e^{-\frac{z}{H}} \, , \tag{2.30}$$

where H is the pressure scale height,

$$H = \frac{p_0}{\rho_o g} = \frac{RT}{g} \, , \tag{2.31}$$

typically around 150 km in the photosphere. Hence pressure and density both fall off exponentially with height. Furthermore, by considering small temporal perturbations in the z axis, it can be shown that acoustic type waves will obey the Klein Gordon equation (Lamb 1909; Roberts 2003) whereby,

$$\frac{\partial^2 Q}{\partial t^2} - c_S^2 \frac{\partial^2 Q}{\partial z^2} + \Omega^2 Q = 0 \, , \tag{2.32}$$

where Ω has frequency dimensions, and the initial perturbation, u, is directly proportional to the new term, Q, such that $|u| \propto \mathrm{p}^{-0.5}|Q|$. Hence a typical photospheric velocity of around 1 km s^{-1} will rapidly increase to a value approaching the sound speed within 600 km (4 scale heights approximates to a $2e$ increase), leading to the possibility of damping mechanisms (e.g., wave shocks (Section 2.5)).

The Ω term in the Klein Gordon equation (2.32) introduces a timescale onto the perturbations. Assume a solution to Eqn. 2.32 of the form,

$$Q(z,t) = Q e^{i(k_z z - \omega t)} \, , \tag{2.33}$$

where ω is the angular frequency ($= 2\pi\nu$) and k_z is the wavenumber ($= 2\pi/\lambda$). Hence $\frac{\partial}{\partial t} \rightarrow -i\omega$ and $\nabla \rightarrow i\mathbf{k}$ in Eqn. 2.32, which becomes,

$$\omega^2 = k_z^2 c_S^2 + \Omega^2 \ . \tag{2.34}$$

From Eqn. 2.34, it is clear that real solutions only exist for values of ω greater than Ω, otherwise waves are evanescent (i.e., $k_z < 0$). This *acoustic cut-off frequency* is defined as,

$$\Omega = \frac{c_S}{2H} \ = 2\pi\nu_{ac} \tag{2.35}$$

which leads to $\nu_{ac} \ \sim$ 5 mHz around temperature minimum.

The increased temperature in the solar interior forms a refractive boundary for acoustic waves. A second boundary is formed at the photosphere due to a sharp density gradient. Waves with a frequency above the acoustic cutoff can escape the photospheric boundary, otherwise they will be reflected back toward the resonant cavity and form a standing wave (and studied as p-modes in helioseismology).

It can be shown (e.g., Lamb 1932; Erdélyi 1954) that the impulsive generation of a wave will lead to a wavefront propagating with velocity c_S. Ahead of this wavefront the medium will be at rest, but the trailing wake of the wavefront will be oscillating at the characteristic frequency, Ω. In addition the amplitude of this oscillation will decay in time as the wavefront moves through the medium. This is directly analogy with the inhomogeneous case (Section 2.4).

2.3.2 Acoustic, Gravity, & Acoustic-Gravity Waves

Assume a plasma with no magnetic field (**B**=0) at rest with constant density, ρ_0, undergoes a small perturbation (subscripts 1) resulting in a plasma flow such that,

$\rho = \rho_0 + \rho_1$,

$\mathbf{v} = \mathbf{v}_1$,

Differentiating Eqn. 2.20 with respect to time, substituting linearised forms of Eqn. 2.14 and Eqn. 2.18, and assuming an isothermal, gravitationally stratified atmosphere as before leads to a generalised wave equation,

$$\frac{\partial^2 \mathbf{v}_1}{\partial t^2} - c_S^2 \nabla(\nabla.\mathbf{v}_1) + (\gamma - 1) g\hat{\mathbf{z}}(\nabla.\mathbf{v}_1) + g\nabla \mathbf{v}_{1z} = 0 \ . \tag{2.36}$$

Once again plane wave solutions for $\mathbf{v}_1$ exist of of the form,

$$\mathbf{v}_1(\mathbf{r}, t) = \mathbf{v}_1 e^{i(\mathbf{k}.\mathbf{r} - \omega t)} \ , \tag{2.37}$$

where propagation is along the wavevector $\mathbf{k}$ ($= k\hat{\mathbf{k}}$). Hence, as before, $\frac{\partial}{\partial t} \rightarrow -i\omega$ and $\nabla \rightarrow i\mathbf{k}$ in Eqn. 2.36, which becomes,

$$\omega^2 \mathbf{v}_1 - c_S^2 \mathbf{k}(\mathbf{k}.\mathbf{v}_1) - i(\gamma - 1) g\hat{\mathbf{z}}(\mathbf{k}.\mathbf{v}_1) + ig\mathbf{k}\mathbf{v}_{1z} = 0 \ , \tag{2.38}$$

which forms the basis for discussing acoustic and gravity waves.

2.3.2.1 Acoustic waves

When pressure is the only restoring force (i.e., g=0), Eqn. 2.38 becomes,

$$\omega^2 \mathbf{v}_1 - c_S^2 \mathbf{k}(\mathbf{k}.\mathbf{v}_1) = 0 \ , \tag{2.39}$$

and assuming a compressible gas (i.e., $\nabla.\mathbf{v}_1 \neq 0$), this simplifies by taking the square root of the dot product with $\mathbf{k}$ to,

$$\omega = k c_S, \tag{2.40}$$

the dispersion relation for acoustic waves. Hence acoustic waves are longitudinal ($\mathbf{v}_1$ is along $\mathbf{k}$), non-dispersive (phase velocity $\mathrm{v}_p = \frac{\omega}{k} = c_S$, and group velocity $\mathrm{v}_g = \frac{d\omega}{dk} = c_S$ are equal), and isotropic (phase speed does not vary with $\mathbf{k}$).

2.3.2.2 Gravity Waves

When gravity is the only restoring force, Eqn. 2.38, after taking the dot product with **k** and with $\hat{\mathbf{z}}$, and some rearrangement becomes,

$$\omega^2 c_S^2 = (\gamma - 1) g^2 (1 - \frac{k_z^2}{k^2}) \ , \tag{2.41}$$

where k_z is the component of **k** along **z**, and which further simplifies to,

$$\omega = \omega_{BV} sin\theta_z \ , \tag{2.42}$$

where θ_z is the angle between **k** and **z**, and ω_{BV} is the Brunt-Väisälä frequency,

$$\omega_{BV}^2 = \frac{(\gamma - 1) g^2}{c_S^2} \ . \tag{2.43}$$

It is clear from Eqn. 2.42 that gravity waves are dispersive (v_p varies with wavelength), and anisotropic (v_p varies with **k**). In addition gravity waves can only propagate with angular frequencies less than ν_{BV} and cannot propagate vertically ($\theta \neq 0$). The group velocity is also perpendicular to the phase velocity such that when waves are upwardly-propagating, energy is downwardly-propagating.

2.3.2.3 Acoustic-Gravity Waves

Under the combined forces of pressure and gravity, the two modes remain distinct. Figure 2.1 shows the dispersion relation for waves propagating in the vertical direction (i.e., along the z axis). Acoustic waves propagate for $\omega > \omega_{ac}$, with group and phase velocity greater and less than the sound speed respectively, and approaching zero and infinity at ω_{ac} respectively. At high frequencies, the waves are purely acoustic. Gravity waves are propagating for $\omega < \omega_{BV}$, with phase and group velocity less than the sound speed. For large k_x, the waves are purely gravitational. The acoustic cut-off is larger

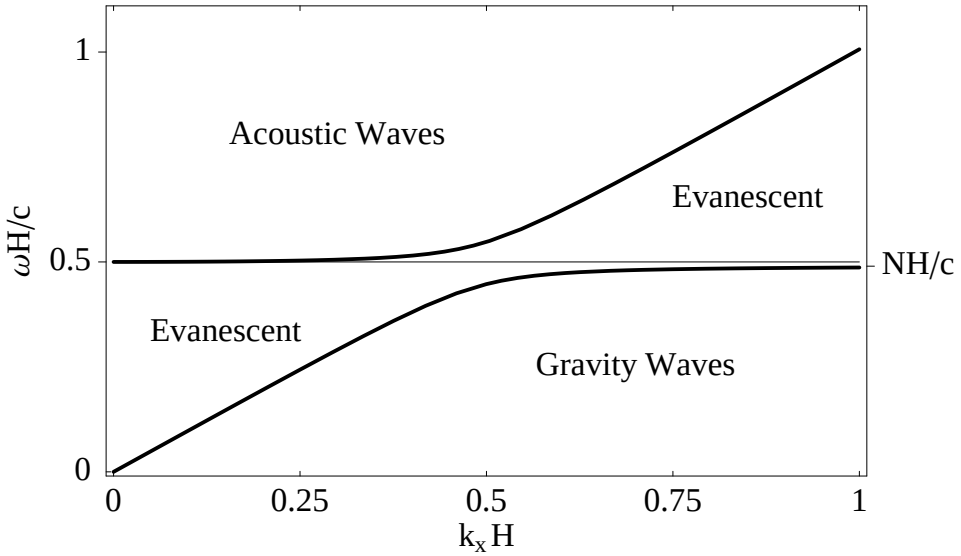

Figure 2.1: Acoustic-gravity dispersion diagram (courtesy of Paul Cally). Waves are propagating in the acoustic and gravity dominated regimes. Between these, waves are evanescent.

than the Brunt-Väisälä frequency by a factor,

$$\frac{\omega_{ac}}{\omega_{BV}} = \frac{c_S}{2H} \times \frac{c_S}{(\gamma-1)^{1/2} g} = \frac{\gamma}{2(\gamma-1)^{1/2}} \ , \tag{2.44}$$

which is ~ 1.02 for $\gamma = 5/3$. Between the acoustic and gravity dominated regimes, waves are evanescent.

2.3.3 Magnetic Waves

By neglecting gravity, but now including magnetism, a plasma at rest with constant density, ρ_o, and uniform magnetic field, $\mathbf{B}_0$, undergoes a small perturbation (subscripts 1) resulting in a plasma flow such that

$\mathbf{B} = \mathbf{B}_0 + \mathbf{B}_1$

$\rho = \rho_0 + \rho_1$

$\mathbf{v} = \mathbf{v}_1$

Differentiating Eqn. 2.20 with respect to time, and substituting linearised forms of Eqns. 2.9 (with a large R_m), 2.14 & 2.18 leads to a second generalised wave equation,

$$\frac{\partial^2 \mathbf{v}_1}{\partial t^2} - c_S^2 \nabla(\nabla.\mathbf{v}_1) - (\nabla\times(\nabla\times(\mathbf{v}_1\times\mathbf{B_0})))\times\frac{\mathbf{B_0}}{\mu\rho_0} = 0 \ . \tag{2.45}$$

Assuming a plane wave solution, as for Eqn. 2.36, leads to,

$$\omega^2\mathbf{v}_1 - c_S^2\mathbf{k}(\mathbf{k}.\mathbf{v}_1) - (\mathbf{k}\times(\mathbf{k}\times(\mathbf{v}_1\times\mathbf{B_0})))\times\frac{\mathbf{B_0}}{\mu\rho_0} = 0 \ . \tag{2.46}$$

2.3.3.1 Alfvén Waves

As discussed in Section 2.2.3 the Lorentz force can be interpreted as the sum of a magnetic tension (B^2/μ_0) and a magnetic pressure ($B^2/2\mu_0$). By analogy with a string under tension, this will permit transverse waves with an Alfvén velocity, v_A, given by,

$$v_A = \left(\frac{tension}{density}\right)^{1/2} = \left(\frac{B^2}{\mu_0\rho}\right)^{1/2} \ . \tag{2.47}$$

When the magnetic field is the only restoring force, Eqn. 2.46 reduces to,

$$\omega^2\mathbf{v}_1 = (\mathbf{k}\times(\mathbf{k}\times(\mathbf{v}_1\times\hat{\mathbf{B}}_\mathbf{0})))\times v_A^2\hat{\mathbf{B}}_\mathbf{0} \ , \tag{2.48}$$

which can be reduced by vector identity to,

$$(\mathbf{k}.\mathbf{v}_1)(\omega^2 - k^2 v_A^2) = 0 \ , \tag{2.49}$$

which has two distinct solutions. For $\mathbf{k}.\mathbf{v}_1$ = 0, Eqn. 2.48 (after multiplying out the vector products) becomes

$$\omega = k v_A cos\theta_B \ , \tag{2.50}$$

where θ_B is the angle between $\mathbf{k}$ and $\mathbf{B_0}$. This is the shear Alfvén wave, with a phase velocity which is just the Alfvén velocity along the magnetic field and zero perpendicular

to it, and a group velocity which is always directed along the magnetic field. The $\mathbf{k}.\mathbf{v}_1 = 0$ property means that the velocity is perpendicular to the direction of propagation, hence the waves are transverse. The second solution, $\omega = k\mathrm{v}_A$, is the compressional Alfvén wave, which propagates isotropically.

2.3.3.2 Magneto-Acoustic Waves

By taking the scale product of Eqn. 2.46 with $\mathbf{k}$ and $\mathbf{B}_0$ in turn leads to a pair of equations which combine to give,

$$\omega^4 - \omega^2(c_S^2 + \mathrm{v}_A^2)\mathbf{k}^2 + c_S^2\mathrm{v}_A^2\mathbf{k}^4 cos^2\theta_B = 0 \ , \tag{2.51}$$

and (for $\mathbf{k}.\mathbf{v}_1 = 0$) the Alfvén wave of Eqn. 2.50. As Eqn. 2.51 is quadratic in (ω^2/k^2) the solutions are simply,

$$\left(\frac{\omega}{k}\right)^2 = \frac{1}{2}(c_S^2 + \mathrm{v}_A^2) \pm \frac{1}{2}[(c_S^2 + \mathrm{v}_A^2)^2 - 4c_S^2\mathrm{v}_A^2 cos^2\theta_B]^{1/2} \ , \tag{2.52}$$

yielding two outwardly propagating waves termed the fast-mode and the slow-mode (defined by their phase velocity) in addition to the Alfvén wave. The characteristics of each type of wave in a strong and weak magnetic field are summarised in Table 2.1. Essentially, the fast- and slow-mode waves may be regarded as a sound wave modified by the magnetic field, and an Alfvén wave modified by the pressure. In the limits of $\mathbf{B} = 0$ or $\rho = 0$, the fast-mode becomes a sound wave or Alfvén wave respectively and the slow-mode vanishes.

2.3.3.3 Magneto-Gravity Waves

Under the combined forces of magnetism and gravity the two modes again remain distinct. Gravity waves can propagate at frequencies less than ω_{BV} at small horizontal wavevector (essentially the Lorentz force opposes the transverse variation), and at fre-

Table 2.1: Summary of magneto-acoustic modes. Direction of propagation, and dominant restoring force and velocity of waves with strong and weak magnetic fields are given. (after Stein & Leibacher 1974)

Mode of Wave	Propagation Direction	Magnetic Field Strong	Magnetic Field Weak
Alfvén	along **B**	Magnetic Tension, v_A	
Fast	Isotropic	Magnetic Pressure $\sim v_A$	Gas Pressure $\sim c_S$
Slow	approximately along **B**	Gas Pressure $\sim c_S$	Magnetic Tension $\sim v_A$

quencies greater than $v_A^2 \mathbf{k}_x^2$ (Lou 1995). There are also a pair of upward- and downward-propagating waves at frequencies greater and less than ω_{BV} respectively.

2.3.3.4 Magneto-Acoustic-Gravity Waves

When all three forces act together the behaviour is much more complicated. In general, at high frequencies ($\omega > \omega_{BV}$) the modes are similar to the fast and slow mode magneto-acoustic waves, with the frequency cut-off dependant on the magnetic field. At low frequencies, the gravity mode is cut-off at large k_x by the magnetic field (as in magneto-gravity), and at small k_x by pressure (as in acoustic-gravity waves) (Stein & Leibacher 1974).

2.4 Inhomogeneous Plasmas

For a homogeneous plasma, the velocity, v_M, of magneto-acoustic wave propagation normal to the magnetic field, is obtained by analogy with Eqn. 2.23 and Eqn. 2.26, as,

$$\nabla \left(p + \frac{B_0^2}{2\mu_0} \right) = v_M^2 \nabla \rho \ , \tag{2.53}$$

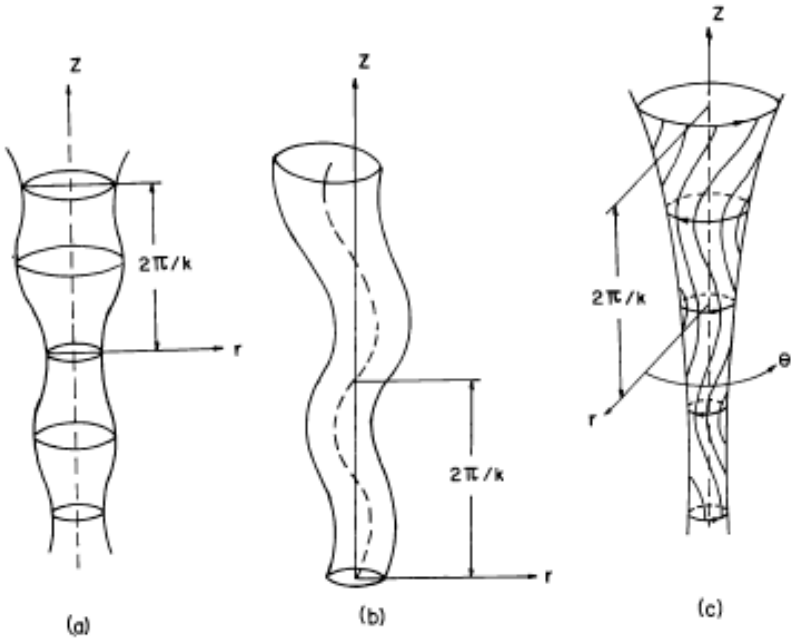

Figure 2.2: The three modes of waves in a thin flux tube. Left to Right: The sausage (longitudinal) mode, the kink (transverse) mode and the Alfvén (rotational) mode. In each case the magnetic field is directed along the z axis (Narain & Agarwal 1994)

which reduces to (Narain & Agarwal 1994),

$$v_M^2 = c_S^2 + v_A^2 \, . \tag{2.54}$$

In general, MHD waves in a homogeneous plasma may be anisotropic, but will always be non-dispersive.

Although MHD waves are extremely complex in the chromosphere (Rosenthal *et al.* 2002), much progress has been made in the study of thin flux tubes in this region of the atmosphere (e.g., Spruit 1981a; 1981b). This is achieved by assuming magnetic field lines are confined in thin tubes creating an inhomogeneous plasma in which various waves modes may exist. These wave modes are dispersive, which will allow for formation of wave packets and dissipation.

The three basic modes for waves in a flux tube are described in Figure 2.2. The sausage-mode wave is a longitudinal wave whereby the tube cross-section expands and contracts due to compressions and rarefactions of the gas. These, acoustic-like, waves

propagate along the tube with characteristic speed, c_λ, given by (Roberts 2000),

$$\frac{1}{c_\lambda^2} = \frac{1}{c_S^2} + \frac{1}{v_A^2} \ , \tag{2.55}$$

which can be also be written as (Kalkofen 1997),

$$c_\lambda^2 = c_S^2 \frac{2}{2+\gamma\beta} \ . \tag{2.56}$$

The kink-mode wave is a transverse wave whereby the field lines in the tube are displaced laterally. It can be thought of as an Alfvén wave which is reduced in speed by the inertia of the tube surroundings. It has a characteristic speed, c_K, given by (Roberts 2000),

$$c_K^2 = \frac{\rho_0 v_A^2 + \rho_e v_{Ae}^2}{\rho_0 + \rho_e} \ , \tag{2.57}$$

where subscript e refers to external parameters (i.e., outside the flux tube). For an isolated flux tube such as found under photospheric conditions, $\rho_0 v_A^2 \gg \rho_e v_{Ae}^2$, and Eqn. 2.57 can be expressed as (Kalkofen 1998),

$$c_K^2 = c_S^2 \frac{2}{\gamma(1+2\beta)} \ . \tag{2.58}$$

Both modes follow a dispersion relation similar to Eqn. 2.34, of the form (Spruit & Roberts 1983),

$$\omega^2 = c_P^2 \mathbf{k}^2 + \Omega^2 \ , \tag{2.59}$$

where c_P is the mode's speed of propagation (c_K or c_λ), and Ω is the mode cut-off frequency. For each mode the wave will be propagating for $\omega > \Omega$ (i.e., $\mathbf{k}^2 > 0$) and evanescent for $\omega < \Omega$ (i.e., $\mathbf{k}^2 < 0$). The cut-off frequencies are given in Kalkofen (1998) as,

$$\nu_\lambda = \nu_{ac} \sqrt{\frac{63+48\beta}{60+50\beta}} \ , \tag{2.60}$$

$$\nu_k = \nu_{ac}\sqrt{\frac{1}{2\gamma(1+2\beta)}}\ . \tag{2.61}$$

As in Section 2.3.1, impulsive wave generation will result in a wave front moving at the respective tube speed, with a trailing wake which will oscillate at the respective cut-off frequency. The third mode is the torsional Alfvén wave, which is a rotational oscillation of the tube.

The flux tubes will spread horizontally with height, due to the pressure stratification, so that somewhere in the high chromosphere they fill out to occupy the whole space and create the magnetic canopy. In the canopy the field can once again be thought of as homogeneous, the torsional wave goes over into the Alfvén wave and the sausage and kink waves go over into the slow and fast waves. Furthermore non-linear mode conversion (mode-coupling) is expected to occur in the canopy.

2.5 Heating Theories

The most important factors in any heating theory involving waves are initially creating a wave and then transferring the energy to the upper chromosphere where the energy has to be deposited. These factors are generally discussed as follows.

• Generation

Flux tube waves can be generated at the photosphere in a number of ways: transverse buffeting by granules can create kink waves; pressure changes can create sausage waves; twists in the tube may create torsional waves.

• Propagation

Only oscillations with frequencies above the respective cut-off will propagate, otherwise waves will be evanescent.

• Dissipation

When waves reach the required height in the atmosphere the mechanical energy has to be transferred to heat energy in the surrounding plasma. This can be achieved in a

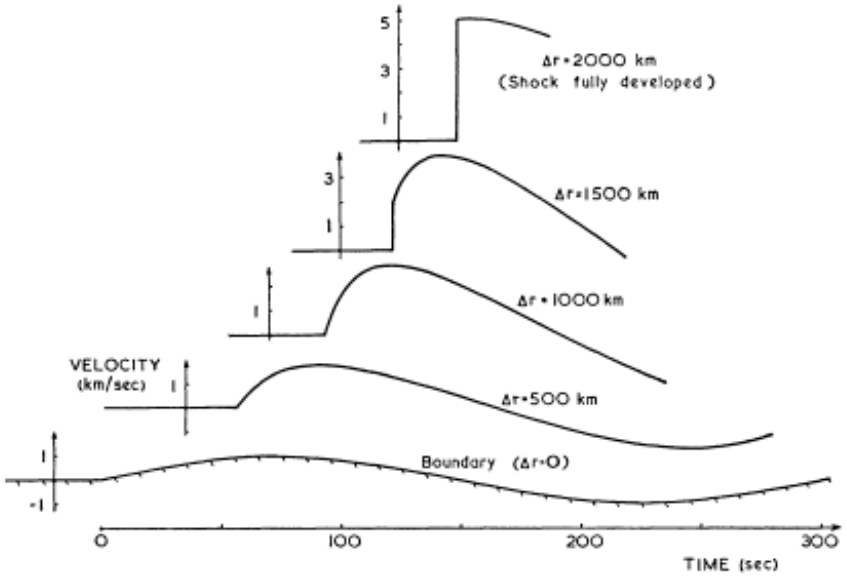

Figure 2.3: A sinusoidal wave changes shape with increasing height in a stratified atmosphere. As the compressed regions travel faster, a wave shock front is gradually formed. (Bird 1964)

variety of ways, the most common of which is by the wave shocking.

For longitudinal modes, the waves cannot directly heat the surrounding gas, instead they cause the plasma to vibrate. As they move up through the atmosphere ρ decreases and the wave amplitude, V, increases so the total wave energy, ρV^2, remains constant. In effect, the sinusoidal form of the original wave is distorted such that compressed regions travel faster than rarefied regions. Eventually, when the amplitude reaches the sound velocity a shock front is formed (Figure 2.3). The rise in both density and temperature behind the shock wave increases the rate of radiation, hence creating an important dissipation mechanism. This form of heating is found to be efficient in the lower chromosphere for acoustic waves (Phillips 1992). In the presence of a magnetic field shocks are much more complicated but, similar to acoustic waves, MHD waves in general shock when any disturbance within the wave moves faster than the characteristic wave speed. In recent years further theories (e.g., phase mixing, resonant absorbtion) have also been proposed as possible heating mechanisms.

Throughout Chapters 4 – 6 I discuss various AC chromospheric heating theories

based on the equations and wave modes described above. The generation, propagation and dissipation of different wave modes lead to different oscillations. The search for these oscillations gives an indication of which wave mode, and hence which heating mechanism, may be present in different parts of the chromosphere. The observations used to search for these oscillations are described in the next chapter.

Chapter 3

Instrumentation

The chromosphere has long been studied from ground-based telescopes in optical wavelengths, especially the strong Fraunhofer lines. This has the benefits of being relatively cheap and simple to implement, with *in situ* corrections easy to perform. Advances in both telescope technology and post-processing has also improved the quality of data from ground-based telescopes. However space-based telescopes will always have the advantages of being able to provide long-duration observations, free of any atmospheric distortion, in all wavelengths. The work in this thesis utilises both ground- and space- based observations, with the aim of maximising the respective advantages of each.

3.1 Richard B. Dunn Solar Telescope

3.1.1 General Description

At an altitude of 2804 m, the National Solar Observatory[1] at Sacramento Peak is in a prime location for high-resolution imaging of the Sun. The Dunn Solar Telescope (Figure 3.1) at Sacramento Peak was originally dedicated the Vacuum Tower Telescope in 1969 and rededicated in 1998 after Richard Dunn who was the main driving force behind it. Its basic design consists of a large 41 m tower with a 0.76 m window at the top. Sunlight is reflected by a pair of movable 1.1 m mirrors down a 1.2 m diameter, 100 m long evacuated tube. Light reflects off a concave 1.6 m main mirror at the bottom of the telescope, 57 m below ground, and then back up to the observing room. The two mirrors at the top act as a heliostat, therefore compensating for proper motion. The entire set-up hangs from a low-friction tank that contains about 10 tons of mercury and hence it is easy to rotate the 200 tons of tube and instruments to compensate for apparent image rotation.

[1]The National Solar Observatory is operated by the Association of Universities for Research in Astronomy under a cooperative agreement with the National Science Foundation

Figure 3.1: The Richard B. Dunn solar telescope. The large tower houses the optic benches, and half of the telescope is underground

3.1.2 Optical Lines

The observations were taken on 1998 September 22 as part of an eleven day long joint campaign with *TRACE*. The aim of the campaign was to examine the relationship between quiet-Sun events in the photosphere, chromosphere, and transition region. The set-up for the observing run is displayed in Figure 3.2 and the data is described in Table 3.1. The Universal Birefringent Filter (UBF; Bonnacini *et al.* 1989) was tuned successively through eight wavelengths, with a cycle time of 45 s. At each UBF image

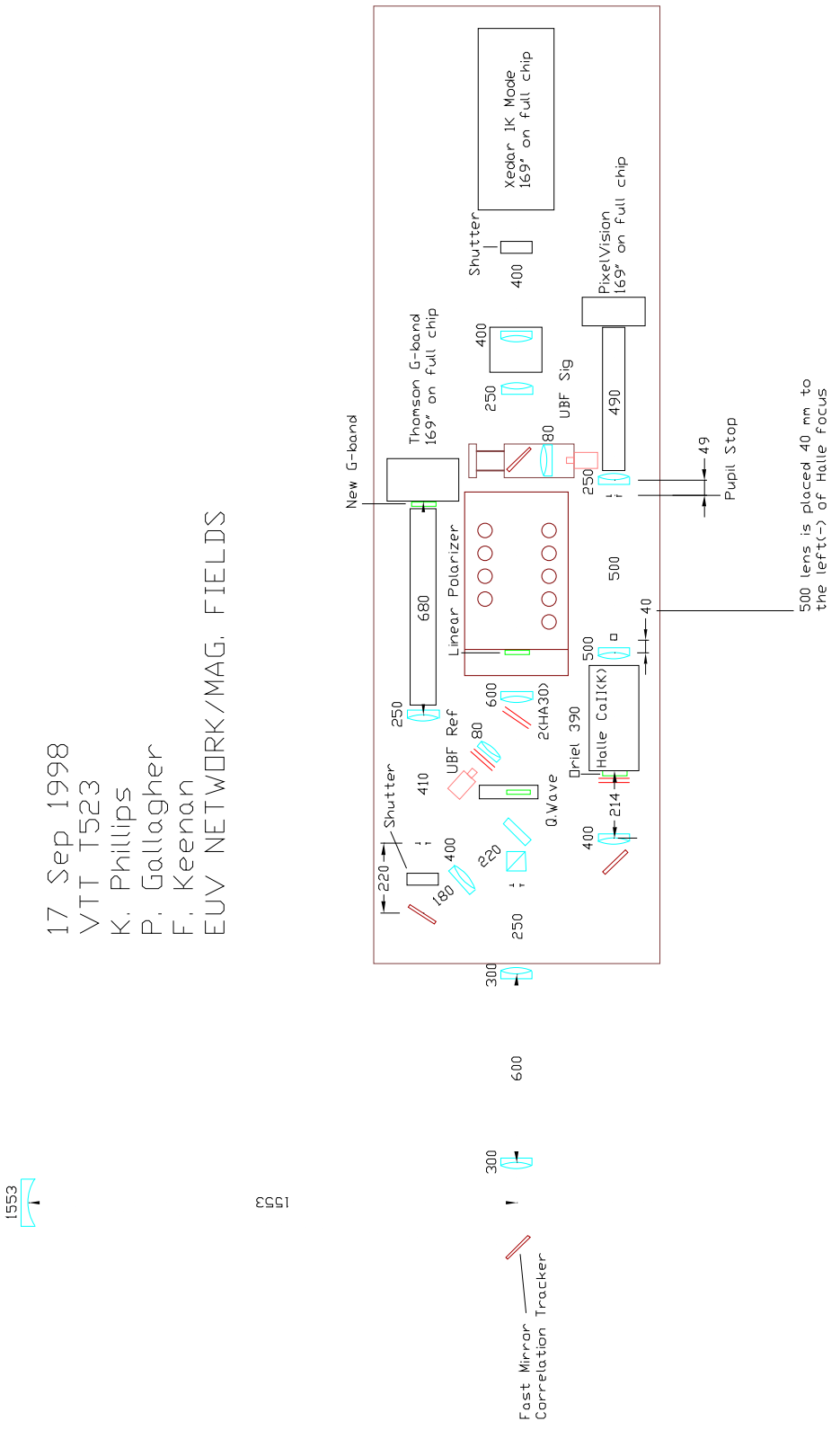

Figure 3.2: *DST* optical bench set-up

Table 3.1: Summary of *DST* data

Line	Wavelength (Å)	Instrument	CCD size
Ca II K_3	3933.7	Halle	512×512
G-band	4305.0	Thompson	1024×1024
Hα	6562.8	UBF	934×968
Hα+0.7Å	6563.5	UBF	934×968
Hα+1.0Å	6563.8	UBF	934×968
Mg I b_2	5172.7	UBF	934×968
Mg I $b_1 - 0.4$ Å	5183.2	UBF	934×968
FeI	6302.5	UBF	934×968
FeI	6032.5	UBF	934×968
continuum	5256.4	UBF	934×968

acquisition step, images through the Halle filter (Ca II K_3) and Thompson filter (G-band) were also acquired onto separate CCDs. Each cycle was saved in FITS format, such that each UBF file contained one image at each wavelength, and each Halle (and Thompson) file contained 8 images. Flatfields were acquired by rapidly slewing the telescope. Darks were acquired by blocking all light to the CCD. Co-alignment of the field-of-view (FOV) with *TRACE* data led to a calculated spatial pixel size of $0.33''$ per pixel for the Ca II K_3 images and $0.18''$ per pixel for the UBF images.

3.1.3 Magnetograms

The Zeeman effect states that the emission from an atom in an external magnetic field will be split into several components. The shift of these components from the normal wavelength of emission is directly proportional to the field strength. Viewed along the magnetic field, these shifted components are left- (L) and right- (R) circularly polarised. Hence, by imaging the L and R circularly polarised components, both the Stokes I (=R+L) and Stokes V =(R-L) signal can be easily calculated for each pixel. The degree of polarisation, P (=V/I), is directly proportional to the magnetic field.

For this dataset, both circularly polarised components of an Fe I line ($\lambda = 6302.5$ Å)

Figure 3.3: *TRACE* spacecraft. The three triangular windows are the EUV filters. The fourth circular window is the UV entrance filter.

were imaged in the UBF cycle. This was achieved by initially passing the light through a $\lambda/4$ plate in order to change the polarisation from circular to linear. Then a linear polariser only accepts light polarised parallel to its optical axis. Reversing the $\lambda/4$ retardation will change the direction of the two polarised components. Unfortunately the time delay (a few secs) between the acquisition of L and R images means that large scale seeing effects dominate the data. These can be reduced by firstly destretching the data, aligning to sub-pixel accuracy, then combining the R and L images, integrating over several of these combinations and applying a spatial smoothing. This meant that it took $\sim$30 minutes of data to create one magnetogram, and hence time series analysis of magnetic field information was not possible. However it was possible to identify photospheric magnetic features with increased intensity in the chromosphere (Chapter 4).

Table 3.2: Summary of *TRACE* filter passbands (Handy *et al.* 1999a)

Central Wavelength (Å)	Emission	Bandwidth (Å)	Temperature $\log_{10}$ (K)
171	Fe IX/X	6.4	5.2–6.3
195	Fe XII/XXIV	6.5	5.7–6.4, 7.0–7.4
284	Fe XV	10.7	6.1–6.6
1216	Lyα	84	4.0–4.5
1550	C IV	30	4.8–5.4
1600	UV cont.	275	3.6–4.0
1700	UV cont.	200	3.6–4.0
5000	White light	broad	3.6–3.8

3.2 Transition Region and Coronal Explorer

3.2.1 Characteristics

The Transition Region and Coronal Explorer (*TRACE*; Handy *et al.* 1999a) is a single-instrument 0.3 m Cassegrain telescope capable of imaging the solar atmosphere in a temperature range of 6×10^3–1×10^6 K at a spatial resolution of $1''$ (pixel size $0.5''$), equivalent to $\sim$ 770 km on the sun, with typical temporal cadence of 20–40 s. It was launched on a Small Explorer spacecraft from a Pegasus XL vehicle on 1998 April 2 into a geo-polar orbit. As such it provides uninterrupted observations for a 9-month period, followed by a 3-month partial eclipse. The *TRACE* orbit passes through the South Atlantic Anomaly (Sherrill 1991) and auroral radiation belts, which limit the duration of continuous observation sequences.

3.2.2 Imaging in the Ultraviolet

The 1024×1024 pixel^2 CCD is sensitive in both the ultraviolet (UV) and extreme ultraviolet (EUV). The telescope is divided into four quadrants, three of which are designed for EUV imaging (Figure 3.3). In this thesis I work on data from the fourth

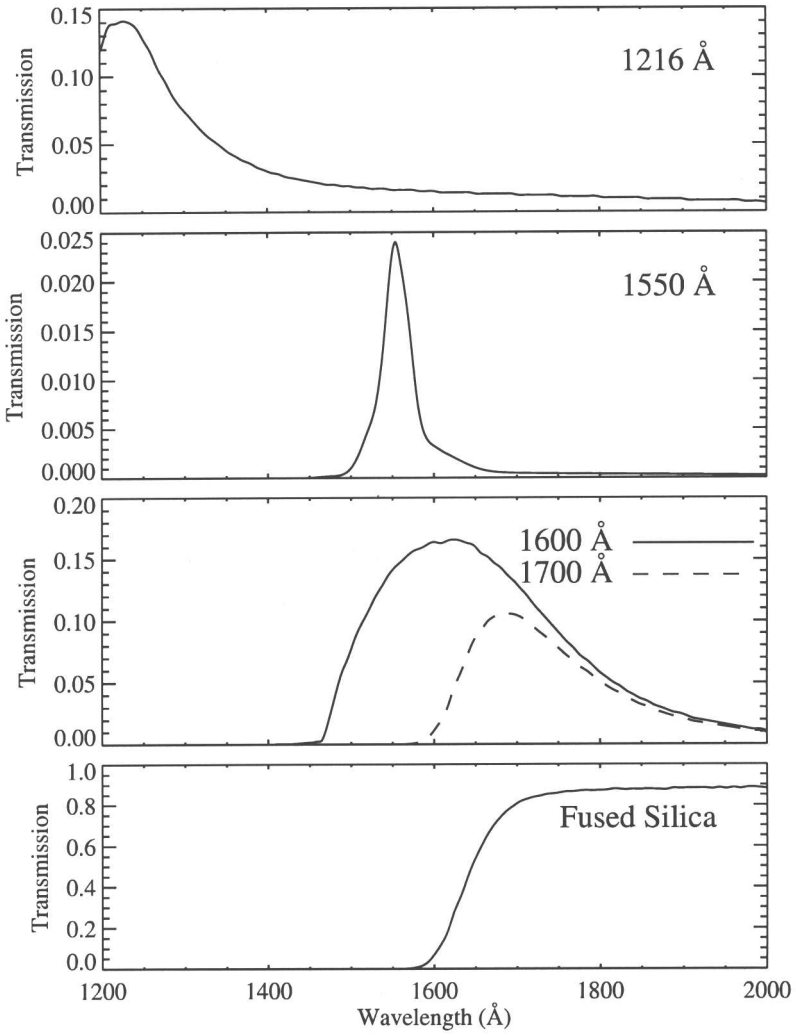

Figure 3.4: The four *TRACE* UV filter passbands are displayed. From top to bottom these are Lyα, C IV, 1600 Å continuum and fused silica. The fused silica and 1600 Å continuum filters are combined to form a further filter passband centred on 1700 Å (Handy *et al.* 1999a)

quadrant, designed to image in UV wavelengths.

The UV filter entrance has a multi-layer dielectric coating on a MgF_2 substrate, which acts to block long-wavelengths ($>$ 2000 Å), whilst optimising transmission at both C IV (1550 Å) and Lyα (1216 Å). Various combinations of filters are used to image a number of wavelengths, namely 1216 Å, 1550 Å, 1600 Å, 1700 Å and white light. Details of the passbands and filters used are provided in Table 3.2 and Figure 3.4. Essentially the C IV, Lyα and UV continuum (centred on 1600 Å) provide three individual passbands. The 1600 Å and fused silica filters are used in tandem to create a

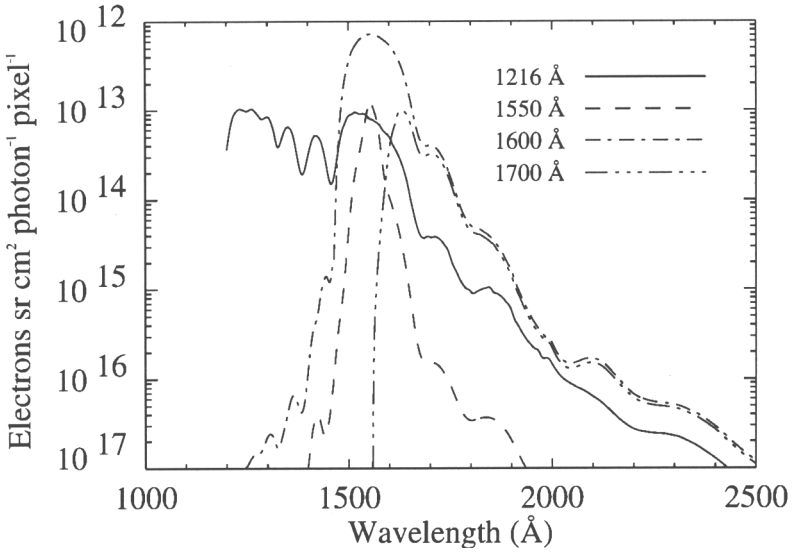

Figure 3.5: Combined response function of *TRACE* UV optics and quantum efficiency of the CCDs. (Handy *et al.* 1999a)

fourth filter, centred on 1700 Å, whilst the fused silica filter also provides white light images. The response function of each passband (including quantum efficiency of the CCDs) are displayed in Figure 3.5. Linear combinations of images in these passbands can then be used to isolate both the C IV and Lyα emission from the continuum (Handy *et al.* 1998, Handy *et al.* 1999b). Depending on the aims of the observing program, images may be taken in all eight passbands, obviously at the expense of a lower cadence for the dataset.

3.2.3 Data Reduction

The extensive *TRACE* branch of the SolarSoftWare (SSW; Freeland & Handy 1998) tree of IDL provides a comprehensive suite of data reduction and analysis tools. Data are provided from several data centres worldwide and commonly downloaded as hour-long multi-fits (.mxf) files. The *structure* format of *TRACE* data is vital as the shear size of these files can be overwhelming. The structure format provides a means of perusing the data without loading the image files, and extracting the relevant data by keyword (e.g., only certain passbands or specific times).

Chapter 4

Oscillations in Ca II *K_3 Observations of the Quiet-Sun Network*

The spatial variation of chromospheric oscillations in network bright points (NBPs) is studied using high-resolution observations in Ca II K_3. Lightcurves, and hence power spectra, are created by isolating distinct regions of the NBP via a simple intensity thresholding technique. Using this technique, it is possible to identify peaks in the power spectra with particular spatial positions within each NBP. In particular, long-period oscillations (4–15 min; 1–4 mHz) were found in the central portions of each NBP, indicating that waves present are certainly not acoustic. These oscillations are possibly due to magneto-acoustic or magneto-gravity wave modes. We also show that spatially averaged or low spatial resolution power spectra can lead to an inability to detect such long-period waves.

4.1 Introduction

The solar network, defined as the boundaries of supergranular flows, contains oscillation with periods longward of the acoustic cut-off and the Brunt-Väisällä cut-off (the low-frequency cut-off for gravity waves). These are not correlated with underlying fluctuations (Lites *et al.* 1993; Cauzzi, Falchi, & Falciani 2000), and their origins have been attributed to magnetic stochastic processes (Kneer & von Uexküll 1985; 1986; von Uexküll *et al.* 1989), or events spatially removed from the network, e.g., granular overshoot. Imaged in the light of Ca II K_3 (3933.7Å), the network is only partially defined, as brightenings at vertices of several supergranules. Due to the coincidence of these network bright points (NBPs) with high magnetic field concentrations, magnetohydrodynamic (MHD) waves (Kalkofen 1997; Hasan & Kalkofen 1999) and magneto-gravity waves (Damé, Gouttebroze, & Malherbe 1984; Deubner & Fleck 1990; Kneer & von Uexküll 1993) seem to be the modes most likely present. The mechanism responsible for heating the network is still the topic of much debate, with a recent publication by Rosenthal *et al.* (2002) beginning to readdress the problem.

The existence of low-frequency (1–4 mHz) oscillations in the solar network of the quiet Sun is well known. Table 4.1 presents a summary of results from published literature (the frequency resolution term in Table 4.1 will be explained in Section 4.2.3). There are several points concerning these results which need to be addressed. Firstly, most studies simply integrate over all network pixels (normally defined as areas which have a higher intensity than some arbitrary value). This means that the lightcurve will be that of the entire network in the FOV, and any small-scale, localised oscillations may be washed out by stronger, global oscillations. There are some exceptions to this: Cauzzi *et al.* (2000) identify eleven separate NBPs, but then average over them; Kariyappa (1994) identifies three individual NBPs; Lites *et al.* (1993) and Curdt & Heinzel (1998) both study only one. Other studies take a different approach, by creating a lightcurve for each and every pixel inside a network 'mask'. However this method is very susceptible to errors due to misalignment and changes in atmospheric seeing, and normally any resulting Fourier power spectra will once again be averaged over the entire network.

Secondly, few results identify specific Fourier peaks, instead preferring to refer to either 'low-frequency power' below a specific value (e.g., Kneer & von Uexküll 1993) or around the 'acoustic band' (e.g., Bocchialini, Vial, & Koutchmy 1994). Of course it must be recognised that this tendency to refer to a frequency band may simply be because of the requirements of the study (e.g., comparing oscillatory power between the network and internetwork). Other studies also prefer to use phase and coherence analysis (e.g., Deubner & Fleck 1990), and do not concentrate on identifying peaks in Fourier power. In cases where specific peaks are identified, their validity may be compromised as they correspond to periods which may be due to insufficiently long observing windows. Through this argument, Kalkofen (1997) discounts all but the 2.7 mHz frequency in Damé *et al.* (1984), and that at 2.5 mHz in Lites *et al.* (1993). A similar argument can be used to discount the 0.6 mHz period discovered by Cauzzi *et al.* (2000). Furthermore, the smoothing window used by Cauzzi *et al.* (2000) directly affects the 1.3 mHz oscillation found by these authors.

Thirdly, the importance of the frequency resolution and other erroneous Fourier effects must be fully recognised. A poor frequency resolution may result in some peaks being omitted (Section 4.2.4). The bottom half of Table 4.1 are results from SUMER (Solar Ultraviolet Measurements of Emitted Radiation, Wilhelm *et al.* 1995) and *TRACE* data. Although the long duration observations, free of atmospheric distortions, makes these data very useful, it should be noted that most results from SUMER studies have been omitted. The reason for this is that in the vast majority of SUMER studies of the quiet Sun, solar rotation is not followed. Hence a new area of the Sun rotates into the SUMER slit every 380 s, introducing a low-frequency cutoff at 2.65 mHz. With only taking specific peaks into account, and addressing the frequency resolution problem, all non-discounted frequencies can be reduced to two broad peaks, one at 2.4 ± 0.3 mHz, and a second at 3.0 ± 0.3 mHz.

In this chapter I use a 'contour & contrast' technique to discover further peaks in NBP power spectra. Furthermore these peaks are identified with particular spatial positions in each NBP. The important improvements over previous work are,

- The careful identification of seven individual NBPs.
- The narrow-band Ca II K_3 filter.
- Long duration observations leading to good frequency resolution.
- Excellent seeing and high spatial resolution.
- Creation and implementation of a new filtering routine.

Table 4.1: Summary of frequencies discovered in network regions in literature. The final column contains details of the full width half maximum (FWHM) of the passband, and whether the oscillations were found in intensity (I) or velocity (V).

Reference	Wavelength	Frequencies (mHz)	Dur. (mins)	Freq. Res. (mHz)	Cadence (secs)	Notes
This study	Ca II K_3	1–4	150	0.11	45	0.3Å FWHM bandpass
Damé *et al.* 1984	Ca II K_3	1.3, 2.0, 2.7, 3.2	52	0.32	10	1.2Å FWHM bandpass
Kneer & von Uexküll 1986	Hα, Hα±0.45Å	<2.4, ∼3.3	54	0.31	20	I only
von Uexküll *et al.* 1989	Hα	2.4, (3.3[a])	64	0.26	30.4	[a] V only
Kneer & von Uexküll 1993	Hα	3.5, <2.4	128	0.13	15	0.25Å FWHM bandpass
	Ca II K	3.2, <2.4	128	0.13	15	0.6Å FWHM bandpass
	Mg I b_2	<2.4	128	0.13	15	0.3Å FWHM bandpass
Deubner & Fleck 1990	Ca II 8498Å& 8542Å	3.3, <2	275	0.06	10	V&I
Kulaczewski 1992	Mg I	3.3–5	80	0.21	15	V&I
	Ca II K_3	<2	80	0.21	15	V&I
	Ca II 8542Å	<3	75	0.22	15	V&I
Lites *et al.* 1993	Ca II H_3	0.9, 1.8, 2.5	62	0.27	5	V only, 1 NBP
Kariyappa 1994	Ca II H_{2V}	2.4	35	0.48	12	I only, 3 NBPs
Bocchialini *et al.* 1994	He I,Ca II K_3	∼3.3	83	0.20	5	V&I, some low freq peaks
Bocchialini & Baudin 1995	He I,Ca II	∼3.3	83	0.20	5	V only, wavelet study
Baudin *et al.* 1996	He I,Si I	∼3.3	83	0.20	5	V only, wavelet study
Cauzzi *et al.* 2000	Hα	0.6, 1.3, 2.2	50	0.33	12	0.25Å FWHM bandpass, 11 NBPs
Curdt & Heinzel 1998	Lyα	2.2–2.4	33	0.50	33.5	SUMER
Krijger *et al.* 2001	1700,1600,1500	3.5	90	0.19	15.0523	*TRACE*, all network
	1700,1600,1500	3.5	228	0.07	21.8625	*TRACE*, all network
Judge *et al.* 2001	JOP 72 data	<5	multiple datasets			*TRACE*, SUMER, MDI
Krijger *et al.* 2003	1216, 1600	< 2, 3–4	48	0.35	40	*TRACE*
	Lyman series (5,9,15)	2–3	48	0.35	29	SUMER
	Ca II K_{2V}	4-5	48	0.35	6	0.6Å FWHM bandpass

4.2 Data Analysis

The dataset used for this study consisted of a 150-minute sequence of $100'' \times 100''$ Ca II K_3 (bandpass FWHM 0.3Å) images centred on quiet Sun (Solar_X = -25″, Solar_Y = -35″) at a 45 s cadence. The sequence was part of the dataset described in Chapter 3 taken at the *DST* (Sacramento Peak / National Solar Observatory), on 1998 September 22 under excellent seeing conditions. Co-alignment of the images with co-spatial and co-temporal *TRACE* data led to a calculated spatial size for the Ca II K_3 images of $0.33''$ per pixel. All images were initially flat fielded and dark-current subtracted. Each image was then aligned to a sub-pixel accuracy to the first image in the series by means of cross-correlation.

4.2.1 Image Segmentation

Seven NBPs were clearly identified (Figure 4.1) which exist throughout the entire dataset and sub-fields of $30'' \times 30''$ centred on each NBP were extracted. This created seven 3-dimensional data cubes (two spatial and one temporal dimension) which were then analysed using custom-written programs in SolarSoftWare IDL (SSWIDL; Freeland & Handy 1998).

For each NBP subset, contours were drawn on each image in the sequence at a chosen intensity threshold value. This contouring ensures that each NBP is followed carefully over time (after Cauzzi *et al.* 2000). It also provides a means of separating the NBP brightenings from the internetwork contribution. Integrating over entire pixel subfields will include signal from both solar (internetwork) and non-solar (sky fluctuations) oscillatory components. Here we add a further improvement to the contour method of Cauzzi *et al.* (2000), that allows us to better isolate each individual NBP. A routine was used to ensure only pixels within a *closed* contour around the NBP were used. This ensures that erroneous pixels – due to sudden fluctuations in the background,

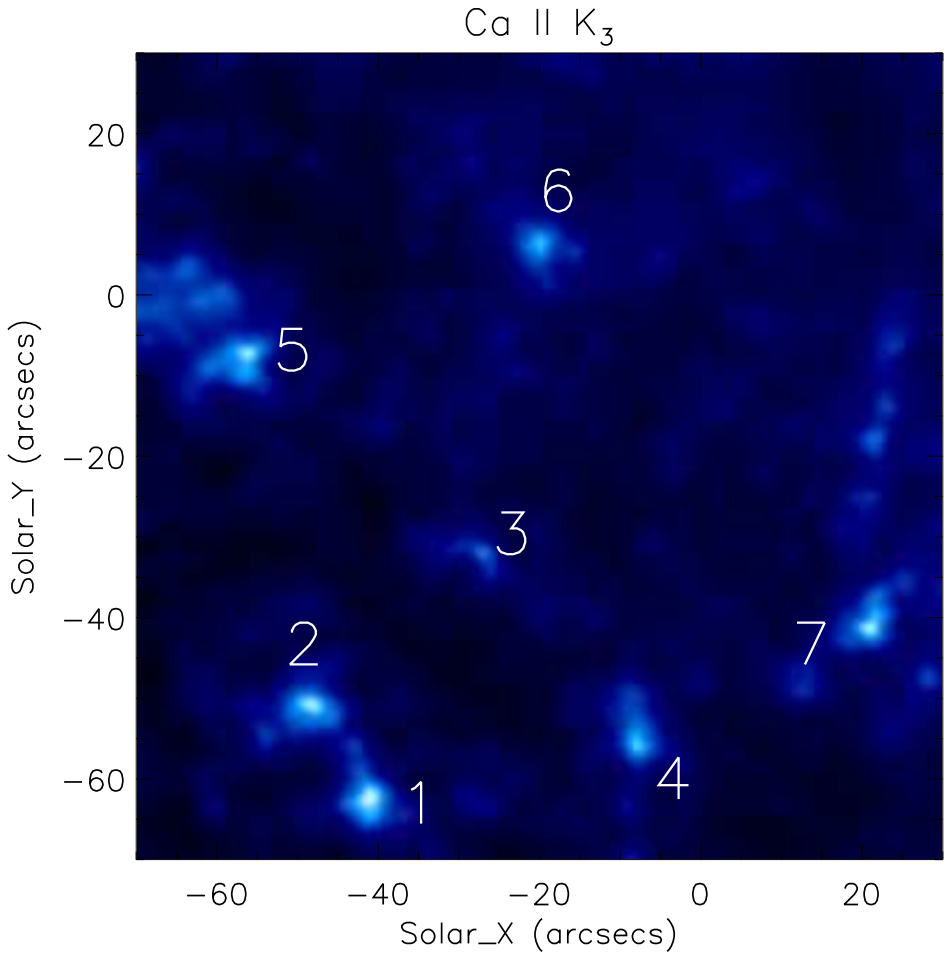

Figure 4.1: Time averaged FOV of the Ca II K_3 dataset. Each NBP which existed throughout the dataset is numbered

supergranular lane flow or other NBPs – are ignored.

4.2.2 Contrast Lightcurves

Lightcurves were created using the following method. For a single image *i*, a histogram of the pixel intensity is constructed, from which I^{bck}, the most common (modal) pixel value of the image, is selected to represent the background. A threshold pixel intensity, I^{thr} is then chosen to contour the NBP. All pixels inside this contour are included in the NBP, and I^{NBP} is calculated as the average intensity value of all these pixels. A further improvement on previous work is achieved by not choosing a constant *absolute*

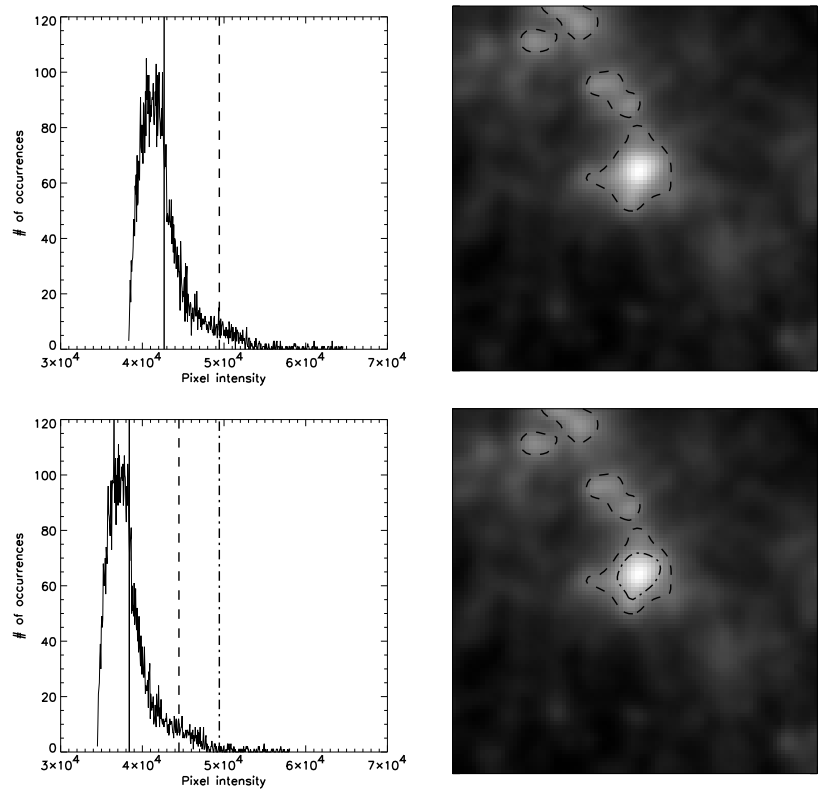

Figure 4.2: Choice of threshold for an NBP. Top row (Image A) - Left plot: Histogram of pixel intensities. The solid line is at the mean, and the dashed line is at 2σ above the mean. Right image: The dashed contour is at the intensity value given by the dashed line of the plot on the left. Bottom row (Image B) - Left plot: Histogram of pixel intensities resulting from the same image as the top row, but with 10% less intensity. The solid line is at the mean, the dashed line is at 2σ above the mean, and the dash-dot line is at the same absolute threshold as the top row. Right image: Both the dashed and dash-dot lines are contoured at the intensities given by the plot on the left. The dash contour on the bottom image contains the same pixels as the contour on top image. The dash-dot contour contains fewer pixels.

threshold for each image in the series. Instead a constant *relative* threshold is chosen throughout, as a number of standard deviations above the mean for the (invariably different) standard deviation and mean of each image. The contrast, C_i, of each image, i, is then defined as,

$$C_i = \frac{I_i^{\mathrm{NBP}} - I_i^{\mathrm{bck}}}{I_i^{\mathrm{NBP}} + I_i^{\mathrm{bck}}} \ . \tag{4.1}$$

This is repeated for every image in the sequence for a given threshold, such that the final lightcurve is then a series of C_i values.

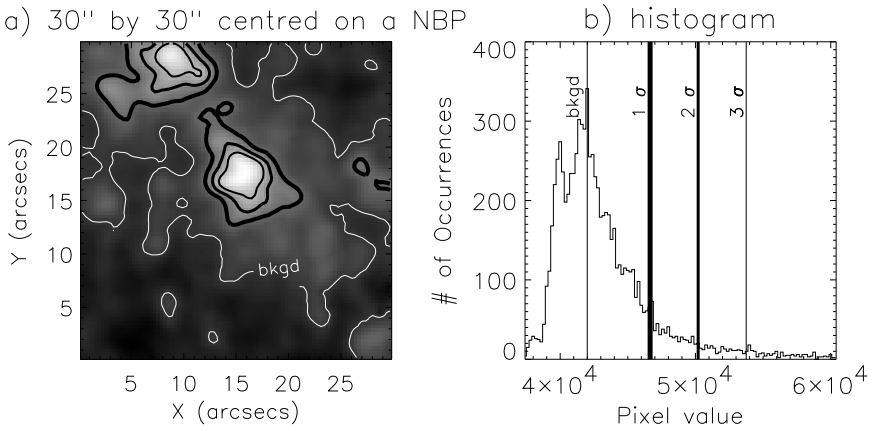

Figure 4.3: Description of thresholding contours on an NBP. (a) Sample NBP. The dark lines show the contour for all pixels in the image which are 1.0σ (thickest line), 2.0σ and 3.0σ (thinnest line) above the mean. Only pixels inside the three centre-most contours are included. The white line contours the background level.(b) Corresponding histogram of the sample image. The background level is the modal value. The three vertical lines refer to the contour levels of (a).

This lightcurve construction removes any long-term trend due to sky fluctuations. For example, assume an NBP exhibits no change in intensity but a thin cloud results in a decreased intensity of 10% between two sequential images, A & B (Figure 4.2). Hence I^{Mod}, the mean ($\bar{I}$), and the standard deviation (σ) will all decrease by 10% in the second image. If the same absolute threshold intensity is used in both images, fewer pixels will be contoured in image B (Figure 4.2 dash-dot line), which will alter I^{NBP} erroneously. However if a constant relative threshold (e.g., 2σ above the mean) is used, the same exact pixels will be contoured in each image (Figure 4.2 dash line). As this results in a decrease of 10% in both I^{Mod} and I^{NBP} the contrast value of each image will be the same.

After the creation of the contrast lightcurve the threshold value was increased and a new lightcurve created. The threshold was chosen to increase from a minimum of 1σ above the mean, in steps of 0.05σ,

$$I^{thr} = \bar{I} + (n\sigma)\ , \tag{4.2}$$

$n \in (1.0, 1.05, 1.10, ...N)$, where N is chosen so that the contour confines at least ten

pixels in all images in the sequence (this normally occurred in only one image per sequence, such that the average number of pixels in an image at maximum threshold was around one hundred). With this method, increasing the threshold corresponds to better isolation of the very centre of the NBP (Figure 4.3a), and provides a means of probing and comparing different parts of the NBP. Essentially this increasing threshold creates a series of nested contours in the NBP.

This 'contour & contrast' method can only be applied to data with a high spatial resolution in two simultaneous spatial dimensions and with good seeing conditions. A low spatial resolution means few pixels will be contoured at high threshold. Spectrometers normally only have one spatial dimension so require an image to be built up by scanning the slit across a region. The final image will therefore contain contributions from different points in time. In 'sit and stare' mode the slit may be too small to contour the NBP correctly, and causes an extra low-frequency cutoff (Section 4.1). Finally, poor seeing will lead to poor image contrast, increasing the difficulty of separating the NBP from the background intensity.

4.2.3 Fourier Analysis

A Fourier analysis was carried on each lightcurve using routines written in SSWIDL. For a continuous signal, $f(t)$, sampled at N discrete values, f_k ($k = 0, 1, 2, ..., N-1$), the discrete Fourier transform (DFT), F_j ($j = N/2, N/2-1, ..., -N/2+1$) is given by,

$$F_j = \sum_{k=0}^{N-1} f_k e^{\frac{-2\pi i jk}{N}} \ . \tag{4.3}$$

Each sample is separated by a time interval, δt, such that the entire signal lasts for time $T = \delta t \times (N-1)$. Each value of F_j corresponds to the Fourier transform at a frequency $\nu_j = j/N\delta t$, hence the maximum detectable frequency, termed the Nyquist frequency

is given by,

$$\nu_{Ny} = \frac{N/2}{N\delta t} = \frac{1}{2\delta t} \ , \tag{4.4}$$

and the frequency resolution, is given by,

$$\delta\nu = \frac{1}{N\delta t} \ . \tag{4.5}$$

A poor frequency resolution will blend peaks in the Fourier spectrum, and the Fourier analysis will be susceptible to the picket fence effect (Section 4.2.4).

Where the DFT will be complex and of the form $a(j)+ib(j)$, the Fourier amplitude, A_j, phase, ϕ_j, and power, P_j, can be determined from,

$$A_j = \sqrt{a^2+b^2} \ , \tag{4.6}$$

$$\phi_j = tan^{-1}\left(\frac{b}{a}\right) \ , \tag{4.7}$$

$$P_j = {A_j}^2 = a^2+b^2. \tag{4.8}$$

A useful check at this stage is to ensure the resulting Power spectrum obeys Parseval's theorem, whereby the total Fourier power should be equal to the variance of the original signal, i.e.,

$$\sum_j P_j = \sigma^2 \ . \tag{4.9}$$

A study of the statistical significance of peaks in the power spectrum can be made by assuming a Gaussian distribution for each point in the signal. Hence each point in the power spectrum will have a χ^2 distribution, with two degrees of freedom (DOF). For a significance level, *sig*, (where $0 < sig < 1$), the corresponding value for the power spectrum, P_{sig}, will be

$$P_{sig} = \frac{\sigma^2\chi^2(1-sig, DOF)}{\frac{N}{2}DOF} \ . \tag{4.10}$$

This equation is used throughout at both the 99% (*sig* = 0.99, χ^2(0.01,2) = 9.21) and 95% (*sig* = 0.95, χ^2(0.05,2) = 5.99) level. Essentially this means that if one hundred

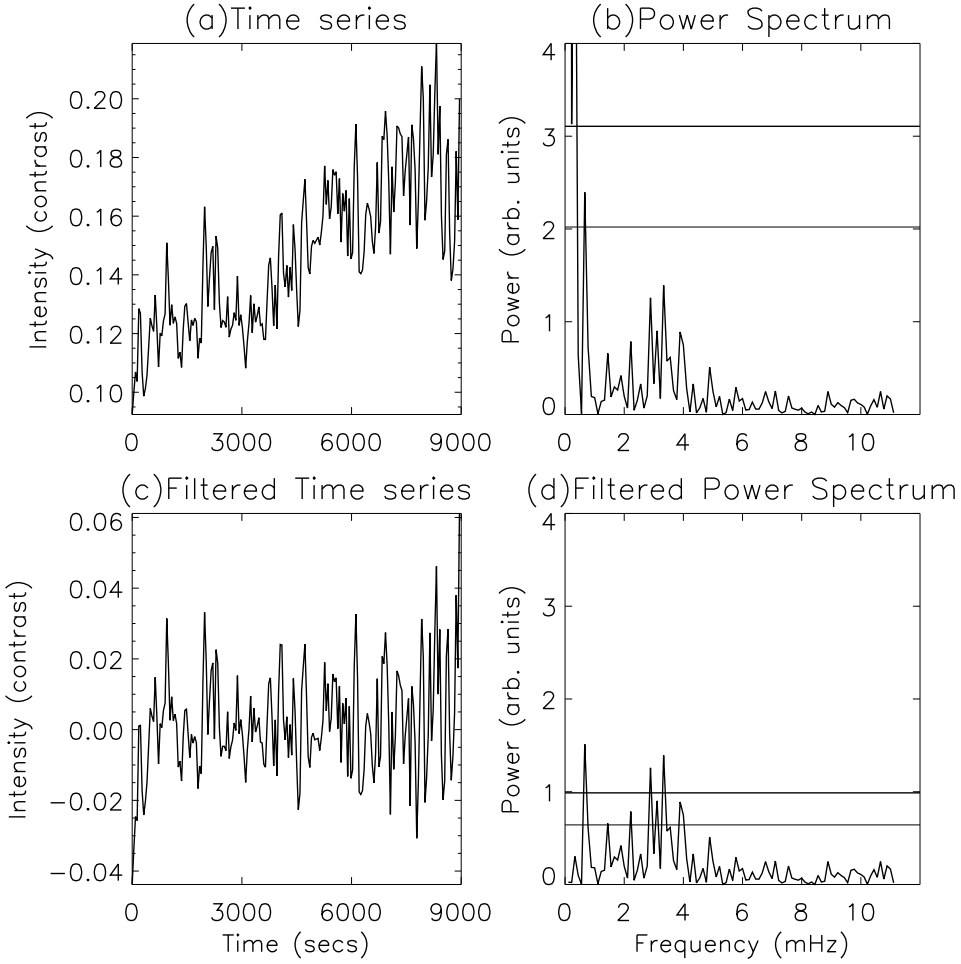

Figure 4.4: The effect of filtering the timeseries and power spectra of the Ca II K_3 lightcurve for NBP2. The top row (panels a and b) gives the raw timeseries and its corresponding power spectrum, while the bottom row (panels c and d) shows the effect of the low-pass filter. (a) and (c) share the same x axis as do (b) and (d). The thick and thin horizontal lines on the power spectra refer to the 99% and 95% significance levels respectively.

Fourier peaks were chosen at random, five would have power above the 95% level, and one would have power above the 99% level.

4.2.4 Filtering

If the original continuous signal contains oscillatory power at frequencies greater than the Nyquist frequency (i.e., signal is under-sampled), aliasing may occur. Aliasing results in power at these higher frequencies showing up as power at low frequencies in the

resulting power spectrum. Hence the first few components of the power spectrum may contain a lot of false power swamping any real peaks in the power spectrum. Figure 4.4 shows the effect of filtering a lightcurve to remove power at low frequencies. The top row contains the original lightcurve and resulting power spectrum. The slowly varying nature of the lightcurve results in the large peaks at < 1 mHz. The bottom row displays the filtered lightcurve and resulting power spectrum. As a result of removing the slowly varying component, the standard deviation of the lightcurve is lower, decreasing the 99% and 95% siginificance levels (Eq. 4.10). Hence the peaks at around 3 mHz become 99% significant.

It is vital to remove these low frequencies without introducing erroneous effects. The most common methods of filtering are applied in the time domain (i.e., simply subtract the trend from the lightcurve, or perform a running average.) However these methods can change the overall shape of the lightcurve. It is statistically preferable to carry out the filtering in the frequency domain by convolving the lightcurve with a suitable Bessel function. The convolution theorem states that the Fourier transform of a convolution is simply given by the product of the individual transforms, i.e., for a convolution, $h(t)$, of two signals, $f(t)$, and $g(t)$, which have Fourier transforms, $H(\nu)$, $F(\nu)$, and $G(\nu)$, respectively,

$$h(t) = f(t) \otimes g(t) \ , \tag{4.11}$$

$$H(\nu) = F(\nu)G(\nu) \ . \tag{4.12}$$

Let the lightcurve be $f(t)$, and the Bessel function be $g(t)$. Their Fourier power spectra, $F(\nu)$, and $G(\nu)$, are displayed in Figure 4.4b, and Figure 4.5, respectively. Note the power spectrum of a Bessel function is simply a high-pass filter with a smooth cutoff. A sharp cutoff would introduce ringing effects into the Fourier analysis. Multiplying the two Fourier spectrum results in a high-pass filtered power spectrum, $H(\nu)$ (Figure 4.4d). An inverse Fourier transform of $H(\nu)$ then reproduces the high-pass filtered lightcurve $h(t)$ (Figure 4.4c).

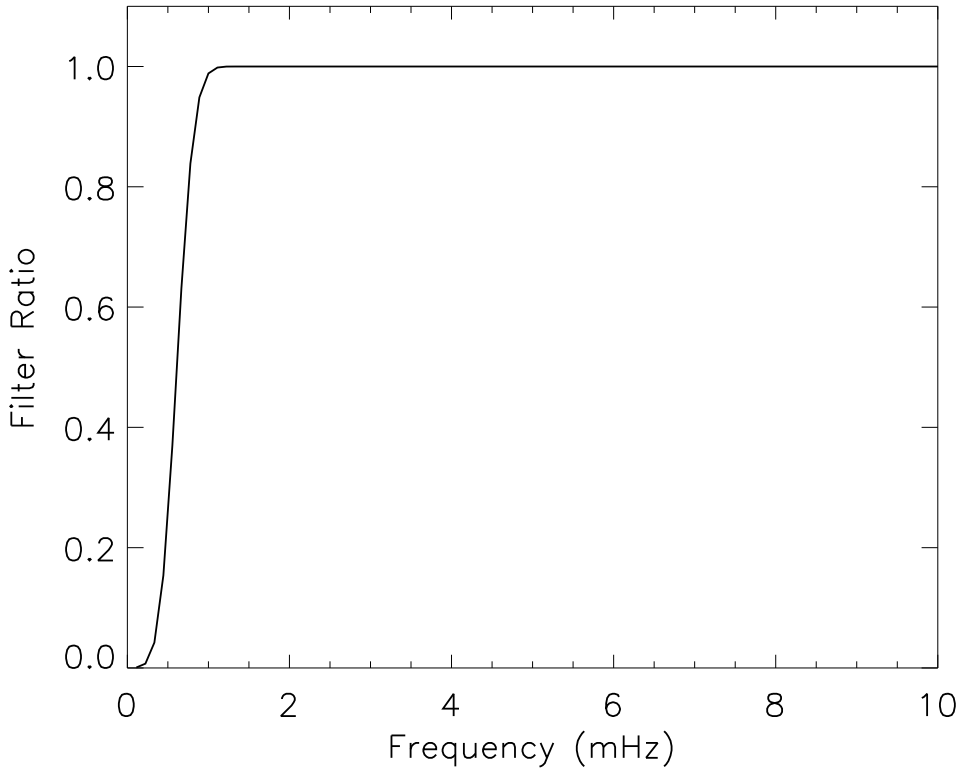

Figure 4.5: The Fourier power spectrum of the chosen Bessel function. This acts as the frequency response curve for the high pass filter and is used to remove low frequency variations. Only power under 1 mHz is attenuated.

For the data presented here, the filter profile (Figure 4.5) was chosen as to have no effect on frequencies above 1.5 mHz, and only reduce the power at 1.0 mHz to 90% of the unfiltered lightcurve. As well as aliasing, other factors of non-solar origin (e.g., atmospheric effects, edge effects) are also strong in this low frequency region.

There are two other important effects which need to be considered when using the DFT, namely *spectral leakage* and the *picket-fence* effect. Spectral leakage is a spreading, or leaking, of spectral components away from the correct frequency. This is a direct result of the finite length of the signal and hence the length is never an exact integral number of any periodicity which may be present. This leads directly into the picket fence effect whereby the actual Fourier peak may lie between two values of ν_j. This effect can be reduced by padding the input signal with zeros, hence increasing the length of the signal and shifting the values of ν_j. This shift may discover spectral components which were initially hidden. In the analysis of this dataset we incorporate

an error value in each peak of $\pm\delta\nu$ (the frequency resolution). Hence a peak at $\nu_j = a$Hz refers to power in the range $(a-\delta\nu)$ – $(a+\delta\nu)$ Hz. This reduces the combined effects of spectral leakage and the picket-fence effect.

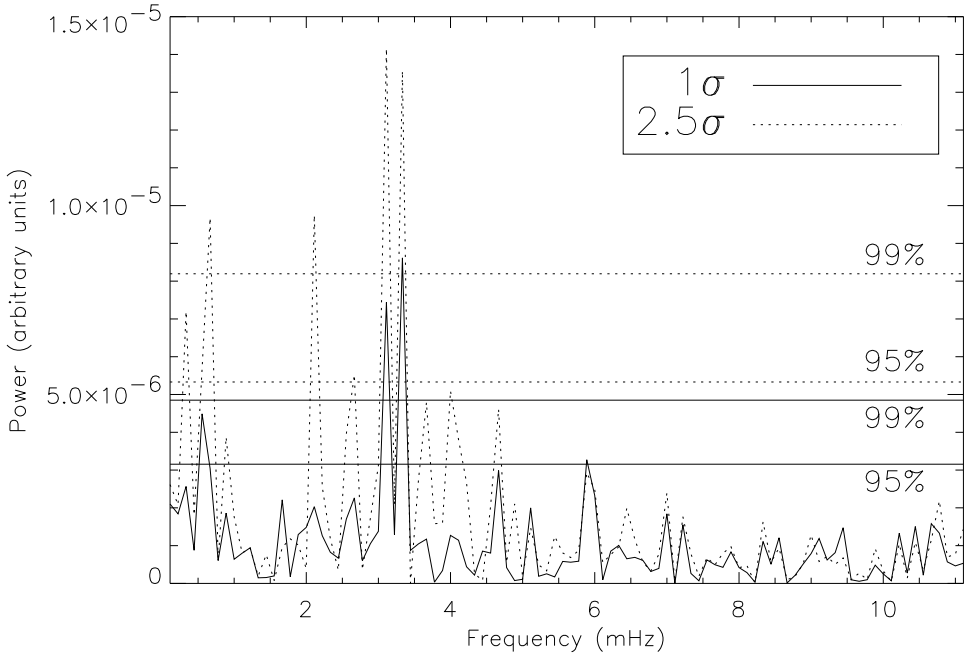

Figure 4.6: Power spectra of a single NBP at different threshold values where the solid and dotted lines refer to a threshold of 1.0 and 2.5 standard deviations above the mean, respectively. The 99% and 95% significance levels are shown, corresponding to the levels at which 1% and 5% of data points, respectively, are expected to be due to random fluctuations.

4.3 Results

All lightcurves at each threshold for all the NBPs were filtered, subjected to a Fourier analysis and the power spectrum inspected for significant peaks. In Figure 4.6 we show an example of how the power spectrum changes with increasing threshold. At high frequencies, the power spectra are very similar for both thresholds, showing no peaks above 5 mHz. At low frequencies the power spectra are markedly different. The power of the two largest peaks, at 3.11 mHz and 3.33 mHz, has increased by a factor of $\sim$2 when the higher threshold is chosen. Furthermore, a peak at 2.67 mHz has increased by a factor of $\sim$2.5 to over 95% significance, and a peak at 2.11 mHz has increased by a factor of $\sim$5, to well above the 99% significance level.

A more detailed graph showing the development of peaks with increasing threshold is given in Figure 4.7. This shows quite clearly the appearance of a 2.11 mHz oscillation at $\sim$1.5σ, peaking in power at $\sim$2.5σ before levelling off around the 99%

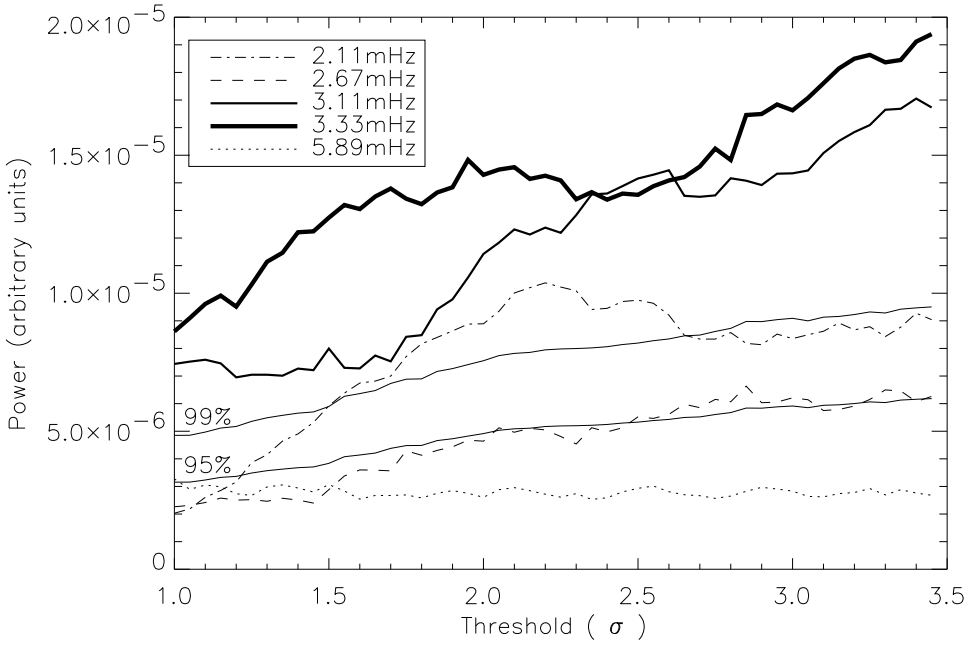

Figure 4.7: Power against threshold for the NBP of Figure 4.3. The *x*-axis gives the threshold in terms of σ above the mean. The 99% and 95% levels are also shown for each threshold

significance level. The 3.33 mHz and 3.11 mHz frequencies more than double in power from minimum to maximum threshold. A 2.67 mHz frequency also appears, but only to the 95% signficance level, whilst the higher value of 5.89 mHz (although staying at a similar power) becomes less statistically significant. Similar behaviour is repeated in all the other NBPs, but for different frequencies in the 1–4 mHz range. The fact that no single specific frequency dominates throughout the network, combined with the lack of this behaviour in internetwork regions, suggests that this is a real effect.

A summary of the frequencies found in each NBP is shown in Table 4.2. In this table the error is taken to be the frequency resolution (i.e., ± 0.11 mHz). There are two distinct types of behaviour described in this table. Some frequencies show a steady increase in power with increasing threshold and, in many cases, are confined to the centre of the NBP. These are denoted '*s*'. Other frequencies showed a steady increase up to a threshold value, after which there is a plateau in power (or slight decrease). These are denoted as '*p*'. The '99' and '95' refer to the fact that the power of the frequency reached higher than the 99% and 95% significance levels, respectively. Frequencies at

Table 4.2: Summary of frequencies found in the seven NBPs, their significance (above **99**% or 95%), and behaviour as a function of thresholding intensity (steady increase –s, plateau –p).

	Frequency (mHz)							
NBP	1.11	1.56	1.89	2.22	2.78	3.11	3.33	3.78
1				**99** *p*	95 *s*	**99** *s*	**99** *s*	
2		95 *p*		95 *s*	**99** *s*	**99** *s*	**99** *s*	**99** *p*
3	95 *s*	**99** *s*			**99** *s*	95 *s*	**99** *s*	
4				95 *s*	95 *s*	95 *p*		**99** *p*
5	**99** *p*			**99** *p*			**99** *p*	95 *p*
6	**99** *p*			95 *p*	**99** *s*		**99** *p*	95 *s*
7	**99** *p*		**99** *p*	**99** *s*				

the 95% significance level which only exist for a small range of threshold values are not included, as they may be random effects, although we note the possibility of frequencies only existing in a very small part of a NBP. It also important to note the long duration of our observations means that even the lowest frequencies are trustworthy

The most striking feature of Table 4.2 is that each NBP exhibits a different oscillatory signal. Some NBPs only show power at the higher (i.e., NBP 1, NBP 4) or lower (i.e., NBP 7) frequencies. Others exhibit strong oscillatory power throughout the entire frequency range (e.g., NBP 5). In terms of frequency occurrence, the 2.22 mHz, 2.78 mHz and 3.33 mHz oscillations are most popular (6 NBPs, with 3.33 mHz always at 99% significance), followed by 1.11 mHz, 3.11 mHz and 3.78 mHz (all in 4 NBPs), 1.56 mHz (2 NBPs) and 1.89 mHz (only 1 NBP). There is no oscillatory power above 4 mHz in any NBP. Concentrating on any one type of behaviour ('*s*' or '*p*'), only the 2.78 mHz oscillation is constant. Power at this frequency always seems to steadily increase with increasing threshold.

4.4 Discussion

It can clearly be seen from Figure 4.8 that particular frequencies may dominate in different areas of a NBP. At maximum threshold, the 3.33 mHz frequency dominates (point

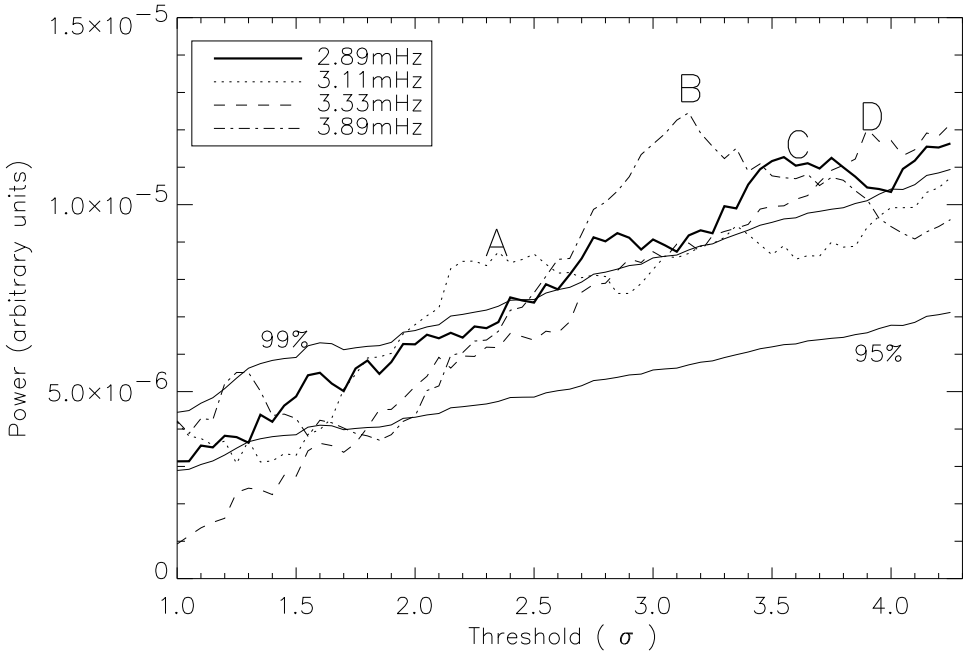

Figure 4.8: Power against threshold for NBP 2 in Table 4.2. Labels A, B, C and D refer to the points in the diagram where different frequencies dominate.

D). With smaller threshold, hence including more of the edge of the NBP, 2.89 mHz (point C), 3.89 mHz (point B) and 3.11 mHz (point A) dominate in turn. As these incremented thresholds refer to a series of nested contours, this highlights how the power spectrum is highly dependent on the chosen threshold value. Hence all frequencies found in the network are spatially localised at both large scale (i.e., the entire network cannot be assumed to have a global mode) and small scale (i.e., even within a NBP different frequencies may dominate in different sections). When the entire $100'' \times 100''$ image is used to create lightcurves using a similar method, (i.e., summing over all NBPs) it is the $\sim$2.22 mHz (steadily increases) and $\sim$1.00 mHz (plateaus) frequencies which dominate. This agrees with the results of Lites *et al.* (1993), who only use one NBP, and Cauzzi *et al.* (2000) who used the average of eleven.

The 3.33 mHz frequency (5-minute) has been previously reported in solar network regions (Kneer & von Uexküll 1993; Al, Bendlin, & Kneer 1998; Bocchialini *et al.* 1994; Baudin *et al.* 1996). However, it does not appear in all the NBPs, and in several cases is not the dominant frequency. Hence it does not appear to be connected to the

well known 5-minute oscillation. Instead the results presented here suggest it localised to specific NBPs.

Despite the seemingly random selection of oscillatory power in Table 4.2, a connection to existing theories can be drawn. In most cases, the onset of low-frequency oscillations coincides with the disappearance of higher frequencies (Figure 4.7), suggesting that gravity or magnetism is the dominant restoring force in the centre of NBPs, at the expense of weaker acoustic waves ($\nu_{ac} \sim 5.55$ mHz). Lou (1995) suggested that diverging magnetic flux tubes in the chromosphere and lower corona forms a magnetic bottle that can trap magneto-gravity modes. This scenario can create long-period oscillations in the range 1200–200 s (0.8–5.0 mHz) in the chromospheric network. All frequencies found here fall within this range,

Kalkofen (1997) shows how fast-mode MHD waves at frequencies greater than $\sim$1.3 mHz can be excited by granular buffeting (Hasan & Kalkofen 1999). These propagate upward and couple with weaker slow-mode MHD waves at a higher frequency of $\sim$3.4 mHz, thereby transferring power to the slow-mode waves. These longitudinal slow-mode waves become shocks, thereby heating the upper chromosphere. Ulmschneider, Zähringer, & Musielak (1991) show that during coupling a fast-mode wave at frequency ν, will transfer most its energy to a slow-mode wave at frequency 2ν, although some energy will be left in waves at the original frequency ν. This agrees with Table 4.2 where the weaker, less common, lower frequencies may be the signature of the fast-mode waves, and the stronger, more frequent, higher frequencies may be the onset of the slow-mode waves

The tendency of NBPs to exhibit stronger oscillatory power in the centre of NBPs has also been pointed out by Judge *et al.* (2001). They use the phrase ‘magnetic shadows’ to describe the decrease in both intensity and oscillatory power in the 3–8 mHz range near but not directly above magnetic elements. This is discussed in terms of upwardly propagating acoustic waves reaching the magnetic canopy and undergoing mode-conversion to MHD waves suggesting ‘magnetic heating occurs only close to the

center of expanding flux tubes, not throughout them'.

In this chapter I have presented a contour & contrast method to identify frequency peaks with particular spatial position inside NBPs. Frequencies detected confirm the $\sim$2.2 mHz and $\sim$3.3 mHz values found previously. New frequencies are also detected at 3.78 mHz, 3.11 mHz, 2.78 mHz and 1.11 mHz in several NBPs, whereas 1.56 mHz only occurs in two NBPs and 1.89 mHz only one. The lack of detection of these frequencies in previous studies may be due to the improved method of isolation of each NBP and a higher frequency resolution. The frequencies found agree with the existence of a magnetic component in the waves, either as magneto-gravity waves or magneto-acoustic waves. In the next chapter I will extend this search from one dimension (i.e., distance from NBP centre, r), into 2 extra dimensions (height in solar atmosphere, z, and localised time domain, t) in order to look for waves propagating throughout the chromosphere.

Chapter 5

Oscillations in Multi-Wavelength Optical Observations of the Quiet-Sun Network

Oscillations in Network Bright Points (NBPs) are studied at a variety of chromospheric heights. In particular, the three-dimensional variation of NBP oscillations is studied using image segmentation and cross-correlation analysis between images taken in the light of Ca II K_3, Hα core, Mg I b_2, and Mg I $b_1 - 0.4$ Å. Wavelet analysis is used to isolate wave-packets in time, and to search for height-dependent time delays which result from upward- or downward- directed travelling waves. In each NBP studied, evidence is found for kink mode waves (1.3 mHz, 1.9 mHz), travelling up through the chromosphere and coupling with sausage mode waves (2.6 mHz, 3.8 mHz). This provides a means for depositing energy in the upper chromosphere. Other upward- and downward- propagating waves in the 1.3–4.6 mHz range are also found. Some oscillations do not correspond to travelling waves and we attribute these to waves generated in neighbouring regions.

5.1 Introduction

This chapter deals with the search for the oscillatory signatures of propagating waves in the chromosphere by extending the work in the previous chapter into two further dimensions (namely height in atmosphere and time). This study uses the fact that both longitudinal and transverse travelling waves are observable as intensity changes in carefully chosen wavelength bandpasses. A propagating longitudinal wave results in a periodic compression and hence heating of the surrounding plasma. This leads to increased radiation, which is then viewable as a periodic intensity change in the filter bandpass. Transverse waves propagating through a plasma result in a Doppler shift of the line profile of the emitted radiation. When the wave is not travelling along the observers line-of-sight ,this results in a periodic change in intensity in the filtergram as the emitted line profile moves in and out of the chosen bandpass. Detailed MHD simulations predict various types of oscillatory signatures for different wave modes at

different heights in the chromosphere. The search for these oscillatory signatures is therefore vital in providing observational evidence for MHD waves.

Simulations of MHD waves are commonly modelled using the thin flux tube approximation, whereby the flux tube radius is much smaller than the characteristic wavelength. This approximation will break down in the mid chromosphere, where the flux tube will expand radially due to decreased density and hence its diameter will exceed the pressure scale height (Spruit 1981a). Further discussion of the validity of the thin flux tube approximation in modelling the network can be found in Hasan *et al.* (2003).

In the thin flux tube approximation a magnetic flux tube in an isothermal atmosphere supports three types of waves (Spruit & Roberts 1983), as discussed in Chapter 2. To summarise, the pure Alfvén torsional wave is non-dispersive and is propagating for any frequency, which negates it as a possible heating mechanism. In a flux tube with a strong magnetic field (as occurs in NBPs), the other types are the transverse, kink-mode wave and the longitudinal, sausage-mode wave. The corresponding tube speeds are given in Kalkofen (1997) in terms of the acoustic speed, c_S (which is around 9 km s^{-1} in the low chromosphere). Both wave modes are dispersive and propagate at frequencies above their respective cut-offs; otherwise they are evanescent. The wave will propagate at the appropriate tube speed, followed by a wake oscillating at the corresponding cut-off frequency. The longitudinal cut-off frequency, ν_l, and the transverse cut-off frequency, ν_k, are defined by Kalkofen (1997) in terms of the acoustic cut-off frequency, ν_{ac} (typically around 5.5 mHz in the chromospheric internetwork K_{2V} bright points, Liu 1974) and given in Chapter 2. For ease of reference they are reproduced as,

$$\nu_l = \nu_{ac}\sqrt{\frac{63+48\beta}{60+50\beta}}\,, \tag{5.1}$$

$$\nu_k = \nu_{ac}\sqrt{\frac{1}{2\gamma(1+2\beta)}}\,. \tag{5.2}$$

With a maximum plasma β value of 0.5 (Kneer, Hasan, & Kalkofen 1996), this gives a minimum ν_k=2.2 mHz and ν_λ=5.7 mHz. However, the local conditions (e.g., density,

magnetic field) in the network can be quite different from the internetwork such that although ν_λ will not vary by more than 2% from ν_{ac} (Kalkofen 1997), ν_k may be much lower than 2.2 mHz. Roberts (1983) also discuss the possibility of non-adibatic conditions in the network, which will drastically alter ν_λ. The exact value of ν_{ac} in the magnetised atmosphere may also differ from the internetwork.

Transverse waves may be generated at the photosphere by granular buffeting of network flux tubes at a frequency above the transverse cut-off. Muller & Roudier (1992) and Muller *et al.* (1994) have discovered that NBPs do possess a rapid, intermittent motion which Choudhuri, Auffret, & Priest (1993) and Choudhuri, Dikpati, & Banerjee (1993) modelled as the creation of transverse mode waves at the photospheric level. These waves can then propagate up along the field lines in a NBP at the corresponding tube speed. Their speed amplitude will increase due to density stratification, so that when it becomes comparable to the tube speed, they enter the non-linear range. At this point mode-transformation can occur (Ulmscheider *et al.* 1991), and the waves can couple (and hence transfer power) to longitudinal waves. This mode-coupling occurs preferentially for transverse waves at a frequency, ν, which can transfer most of their power to longitudinal waves at a frequency 2ν, with a remnant of power at the original frequency. The interaction is greatest when the two tube speeds are equal (i.e., $c_K = c_\lambda$). From Eqn. 2.58 and Eqn. 2.56 it turns out this corresponds to $\beta = 0.2$, which gives a speed of maximum interaction of around 0.93 c_S. The longitudinal waves can then shock and heat the surrounding plasma (Zhugzhda, Bromm, & Ulmscheider 1995).

In order to identify such a mechanism in the chromosphere, a number of tests can be carried out.

•*Test 1*: Power at a frequency ν in the lower chromosphere should also be identifiable at much reduced power in the upper chromosphere.

•*Test 2*: Power at frequency 2ν should appear in the upper chromosphere.

•*Test 3*: Waves at frequencies above the transverse cut-off should propagate at a speed close to c_S.

Table 5.1: Details of *DST* dataset, including an estimation of the height of formation of each bandpass

Line	Wavelength (Å)	FWHM (Å)	Instrument	Image Scale ($''$ per pixel)	Formation Height (km)
Ca II K_3	3933.7	0.30	Halle	0.33	1800-2000[1]
Hα	6562.8	0.21[a]	UBF[b]	0.18	1200-1700[1]
Mg I b_2	5172.7	0.13[a]	UBF[b]	0.18	700-750[2]
Mg I $b_1-0.4$ Å	5183.2	0.13[a]	UBF[b]	0.18	200[3]

REFERENCES:
(a) Beckers, Dickson, & Joyce (1975)
(b) Universal Birefringent Filter, Bonaccini *et al.* (1989)
(1) Vernazza *et al.* (1981)
(2) Schmieder (1979)
(3) Keller & Koutchmy (1991)

•*Test 4*: In the upper chromosphere there may be evidence for waves above the longitudinal cut-off frequency although to a lesser extent as they should shock in this region.
•*Test 5*: Oscillations should be quasi-periodic, resulting from the nature of the granular buffeting.

In this chapter I search for observational evidence of MHD waves by studying intensity changes in NBPs at several wavelengths, corresponding to a range of heights from the photosphere to the upper chromosphere. Section 5.2 provides a summary of the observations and data analysis. Both Fast Fourier Transforms (FFTs) and wavelet transforms are used to study NBP oscillations in space and time. The wavelet transforms are also cross-correlated at all frequencies to check for the signature of possible travelling waves. In Section 5.3 I present and discuss the results from each NBP individually and collectively. These results are then further discussed in Section 5.4 in relation to the observational tests mentioned above.

5.2 Data Analysis

The observational set-up at the *DST* has been described in detail in Chapter 3. For this study, time series analysis of the Ca II K_3, Hα core, Mg I b_2, and Mg I $b_1-0.4$ Å data

were used to provide information as a function of height throughout the chromosphere (Table 5.1).

A 150-minute sequence of $100'' \times 100''$ images were obtained in all wavelengths, centred on a quiet Sun field (Solar_X = -25″, Solar_Y = -35″) with a 45 s cadence. This provided seven NBPs (Figure 5.1), four of which (NBPs 1, 2, 5 & 7) were distinguishable throughout the entire series in all wavelengths, and hence are used here. As discussed in Chapter 3 the UBF cycle (Table 5.1) also included two Fe I (6302.5 Å) images, linearly polarised at 90° to each other. These images were destretched, integrated and combined to create the magnetogram at the bottom of Figure 5.1. Coalignment of the ground based images with the *TRACE* data led to a calculated spatial size of 0.33″ per pixel in the Ca II K_3 data and 0.18″ per pixel for the other wavelengths (Table 5.1). Figure 5.1 shows that the chromospheric NBPs have a one-to-one spatial correlation with the photospheric magnetic field and exist throughout the transition region, and even into the corona.

Analysis of the *DST* observations was carried out using standard routines within SSW. The data were corrected for CCD readout bias and flat-fielded. Each image was aligned to the first image of the series by means of cross-correlation. *TRACE* images were reduced using the standard calibration and despiking routines provided. Light curves in each wavelength were then created using the contour and contrast method, high-pass filtered and subjected to a Fourier analysis as described in Chapter 4.

5.2.1 Heights of Formation

An estimation of the height of formation of each bandpass is provided in Table 5.1. It is important to note both the difficulty of estimating these, and their physical meaning. Essentially the temperature and density of the plasma where the optical depth of light emitted in each bandpass is unity ($\tau = 1$, photons escape from the solar atmosphere without any further absorption) is estimated. These parameters are then compared to

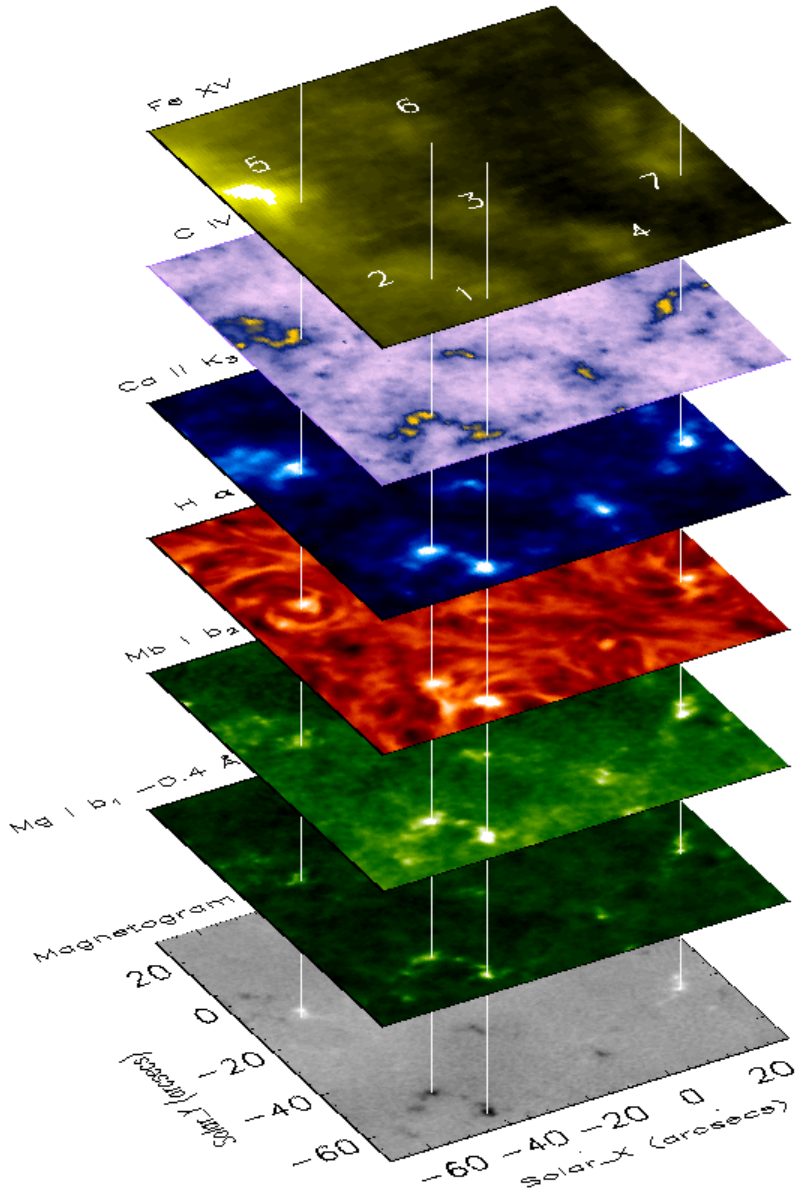

Figure 5.1: Example time-averaged data of the $100'' \times 100''$ FOV in the corona (Fe XV 284 Å), transition region (C IV 1550 Å) and chromosphere (*DST* wavelengths). The bottom plot is the corresponding magnetogram. The vertical lines show the four stable NBPs analysed in this paper.

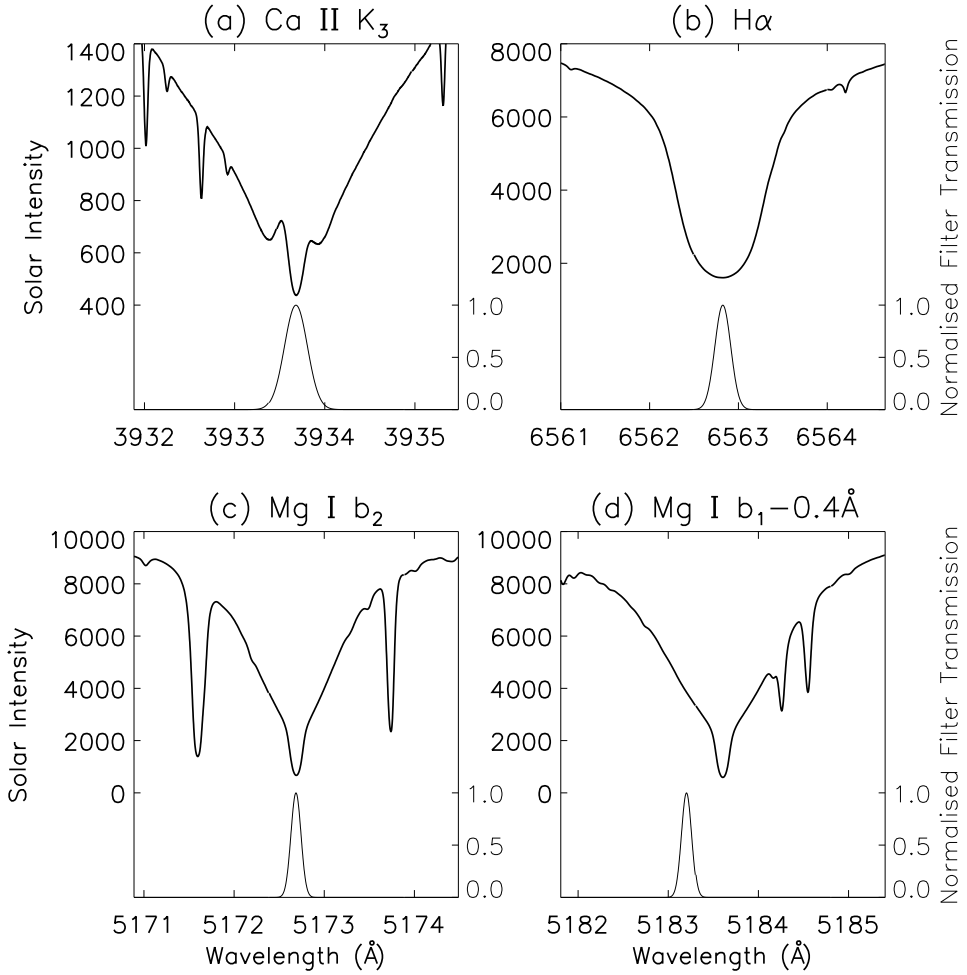

Figure 5.2: Filter profile plotted with line profile for (a) Ca II K_3, (b) Hα, (c) Mg I b_2 and (d) Mg I $b_1 - 0.4$ Å. In each case the leftmost y axis is solar intensity, the rightmost y axis is normalised filter transmission and the x axis is wavelength.

models of the chromosphere in order to assign a height of formation. However this $\tau = 1$ surface will vary dramatically according to the local plasma parameters. This, combined with the fact that most models are of a magnetic-field free plasma, means that care must be taken not to apply too much physical meaning to any height of formation estimation.

Figure 5.2 shows the profile of each filter overplotted on the line profile of the respective wavelength. As the Ca II K_3 profile is narrowband, most of the emission is assumed to be from the K_3 core. However there will be some contribution from the self-reversed K_2 peaks. The VAL model is used here to estimate a height of 1800–2000 km. The height of formation of the Hα core is also estimated from the VAL model. It is well

known that Hα contains a double-peaked response function, so a much larger range of heights is assumed (1200–1700 km). The Mg I b_2 core is discussed in Kneer & von Uexküll (1993) who, with a bandpass of 0.6 Å, place it at ∼350 km. However, the data presented in this paper have a much smaller bandpass, and as such include less of the wings, so are placed at 700–750 km (Schmieder 1979). Keller & Koutchmy (1991) use data 0.4 Å into the red wing of the Mg I b_1 line, and adopt 200 km as the height of formation. Although our data are 0.4 Å in the blue wing, we also adopt this height of formation.

Compared to the relatively clean images of Ca II K_3, Mg I b_2 and Mg I $b_1-0.4$ Å, the Hα images are notoriously difficult to study due to the presence of extra structure (Chapter 1 of this thesis; Zirin 1966). Hence extra care was taken to correctly identify each NBP. The contour method was particularly useful for these data as it ensured non-NBP brightenings were not included.

5.2.2 Wavelet Analysis

Like many time series in solar physics (and astronomy in general), light curves from NBPs are known to exhibit non-stationarity. This means that while the light curve may contain periodic signals, these may vary in both frequency and amplitude with time. As such, a simple Fourier analysis may not detect the time- and frequency–localised oscillations. There are several solutions to this problem. One such solution is to use a *windowed FFT*, whereby a portion of the light curve is selected, and this window is slid along the light curve, calculating the FFT at each step. However this approach means the shape of the curve is dependent on the window size. As is shown in Figure 5.3b, at low frequencies so few oscillations will occur inside the window that frequency–localisation will be lost. At high frequencies there will be so many oscillations inside the window that the time–localisation will be lost. The use of a box-car shape window will also lead to ringing effects.

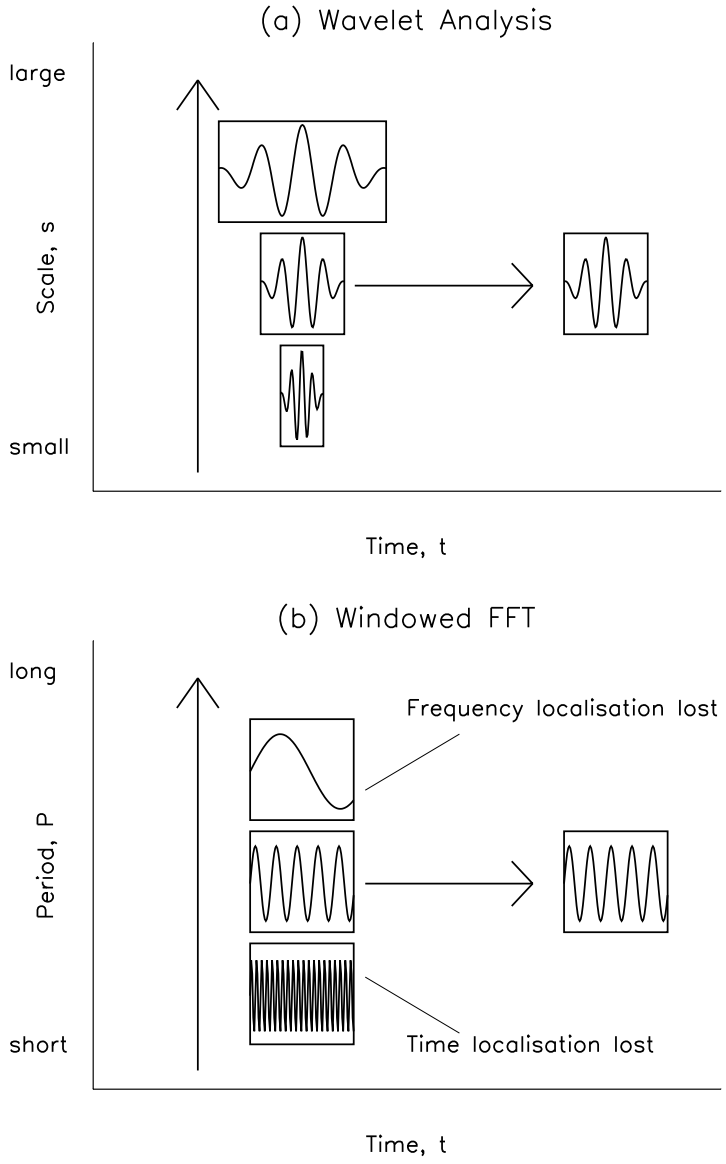

Figure 5.3: A pictorial description of how varying the scale ensure both time - and frequency- localisation are retained in (a) wavelet analysis but lost in (b) a windowed-FFT

Wavelet analysis circumvents these difficulties by using a base wave-packet of finite duration, d, and specific frequency, ν. A convolution of this wave-packet with a section of light curve will give an indication of the oscillatory power (at frequency ν) in that section (of duration d) of the light curve. Sliding this wave-packet along the light curve provides time–localisation. Changing the width of the wave-packet (known as the scale) provides frequency–localisation. The major improvements of wavelet analysis over a windowed FFT are,

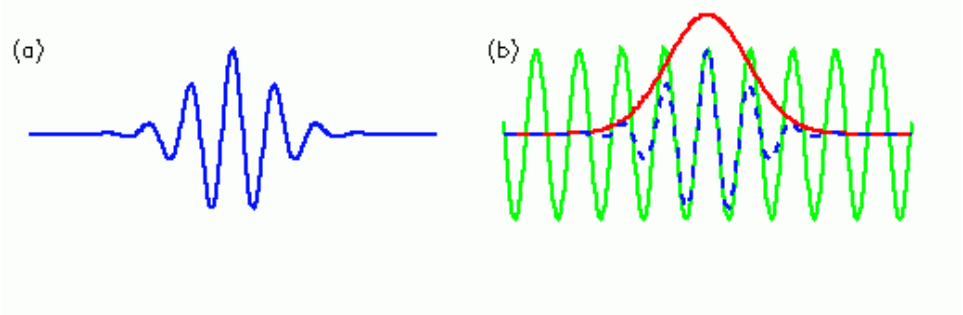

Figure 5.4: The real part (blue) of the Morlet wavelet is simply a sine curve (green), with a Gaussian envelope (red)

(i) wavelet analysis will fit the same number of oscillations for each frequency whereas the windowed FFT does not (Figure 5.3).

(ii) a suitable choice of base-wavelet avoids edge effects.

In this work a wavelet analysis (Torrence & Compo 1998) was carried out on all the maximum threshold light curves using a Morlet wavelet of the form

$$\psi(\eta) = \pi^{-1/4} \exp(i\omega_0\eta) \exp\left(\frac{-\eta^2}{2}\right) , \tag{5.3}$$

where $\eta = t/s$ is the dimensionless time parameter, t is the time, s the scale of the wavelet (i.e., its duration), $\omega_0 = s\omega$ is the dimensionless frequency parameter (i.e., the number of oscillations within the wavelet; ω_0=6 to satisfy the admissibility condition, Farge 1992), and $\pi^{-1/4}$ is a normalization term. The real part of this wavelet is basically a sine curve, with a Gaussian envelope (Figure 5.4). This continuous (and hence nonorthogonal), complex function is ideal for capturing smooth, continuous oscillatory behaviour, but is known to be redundant at large scales (and hence low frequencies) where the wavelet spectrum will be highly correlated (another reason for filtering off low frequencies). The wavelet transform, W_n, at scale, s, of a discrete sequence, x_n ($n = 0, 1, 2, \ldots . N-1$), is a convolution of x_n with a translated $\psi(\eta)$,

$$W_n(s) = \sum_{n'=0}^{N-1} x_{n'} \psi^* \left[\frac{(n'-n)\delta t}{s}\right] . \tag{5.4}$$

The smallest scale, s_0 is normally chosen as 2δt (i.e., inverse of the Nyquist frequency) with the larger scales then 2^n multiples of s_0,

$$S_j = s_0 \times 2^{j\delta j} \ , \tag{5.5}$$

where δj is the spacing between scales and $j = 0, 1, 2...J-1$. Hence the scales values increase logarithmically from s_0 to $s_0 \times 2^{J\delta j}$ and J is calculated by rearranging Equation 5.5,

$$J = \frac{1}{\delta j} log_2 \left(\frac{N\delta t}{s_0} \right) \ . \tag{5.6}$$

The wavelet transform will have a real and imaginary part, from which the amplitude, power, and phase can be determined as for the FFT. These will all be 2-dimensional maps, plotted against both time and scale (here scale, period, and frequency can be interchanged). Significance levels can also be calculated using a method similar to that for the FFT (e.g., for *sig* = 0.95, χ^2(0.05,2) = 5.99, which is then multiplied by the mean power spectrum to give a power value for the 95% level).

Bocchialini & Baudin (1995) note that although wavelet analysis can be used to obtain phase information, this is very sensitive to frequency. They preferred to determine lags from correlations between their signals, and it is an extension of their method which is used here. Essentially, from the 2D wavelet power density maps, 'power curves' at each frequency were created by taking slices of the wavelet power transform. These were then cross correlated across pairs of wavelengths to search for timelags (it should also be noted here that the chosen width of the frequency band should be small enough to negate errors arising from the different weighting of each scale, Torrence & Compo 1998).

5.2.3 *Search for Travelling Waves*

For a pair of wavelengths, λ_1 and λ_2, at a frequency ν, the power curves, $P_{\lambda_1}(\nu)$ and $P_{\lambda_2}(\nu)$ were created. The cross correlation coefficient, $C(\Delta t, \nu)$, of these power curves as a function of timeshift, Δt, is given by

$$C(\Delta t,\nu) = \frac{\sum \left(P_{\lambda_1}(\nu,t) - \overline{P_{\lambda_1}(\nu,t)} \right) . \left(P_{\lambda_2}(\nu,t+\Delta t) - \overline{P_{\lambda_2}(\nu,t+\Delta t)} \right)}{\sqrt{\sum \left(P_{\lambda_1}(\nu,t) - \overline{P_{\lambda_1}(\nu,t)} \right)^2 . \sum \left(P_{\lambda_2}(\nu,t) - \overline{P_{\lambda_2}(\nu,t)} \right)^2}} . \qquad (5.7)$$

This is used to evaluate the shift in $P_{\lambda_2}(\nu)$ which results in maximum correlation with $P_{\lambda_1}(\nu)$. This shift, Δt_{max_corr}, then corresponds to the timelag of $P_{\lambda_2}(\nu)$ onto $P_{\lambda_1}(\nu)$ at frequency ν, and $C(\Delta t_{max\_corr}, \nu)$ is an indication of how good the correlation is. This procedure was then repeated for all frequencies, and between all pairs of wavelengths. From this timelag information, and from a knowledge of the approximate heights of formation (Table 5.1), the speed of possible travelling waves at specific frequencies were calculated (Bocchialini & Baudin 1995; Baudin, Bocchialini, & Koutchmy 1996).

5.3 Results

Example wavelet power transforms for NBP2 are shown in Figures 5.5 and 5.6, where the wavelet diagrams are divided into three boxes. The top panel (a) shows the filtered light curve, while the main panel (b) shows the wavelet power transform, with frequency as the vertical axis and time along the horizontal axis. This time axis is the same as in panel (a), so that direct comparisons between the occurrence of oscillatory power and the parent time series can be made. The lighter an area, the stronger the oscillatory power. The contours refer to the χ^2-derived 95% confidence level, while the cross-hatched area is known as the Cone-Of-Influence (COI; Torrence & Compo 1998). Inside this hatched area, edge effects can be significant, so that any power appearing inside the hatched area has to be treated with caution. The right-hand panel (c)

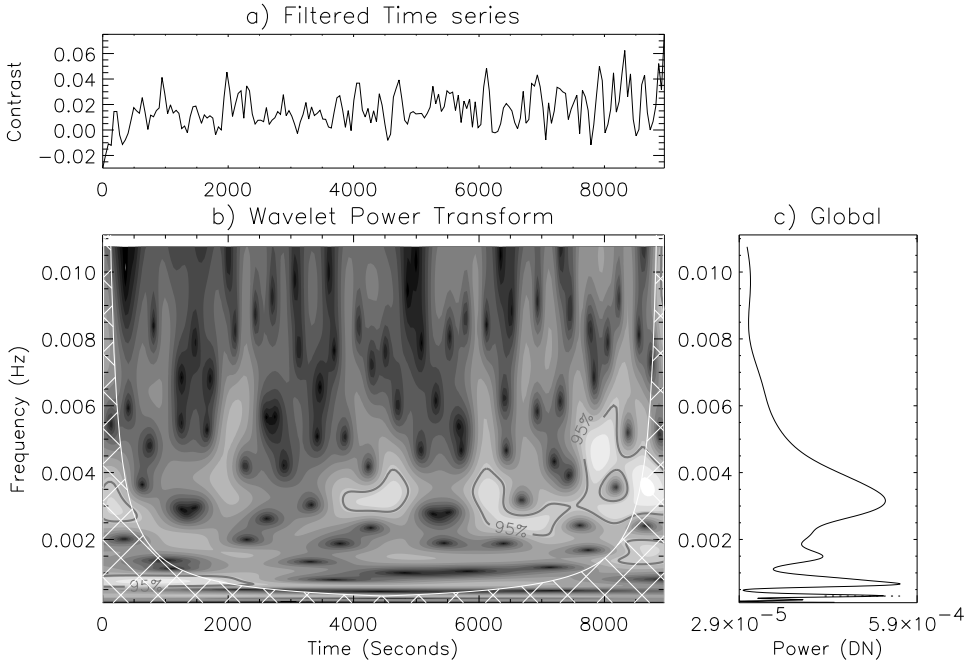

Figure 5.5: Example wavelet power transform for Ca II K_3 data. (a) Filtered light curve from the Ca II K_3 data for NBP2. (b) Wavelet power transform. The lighter an area, the stronger the oscillatory power. (c) The global wavelet spectrum.

shows the global wavelet spectrum. This is the sum of power over all time as a function of frequency, analogous to the FFT. However it should be noted that at large wavelet scales (low frequency), peaks will be sharper and hence have a larger amplitude. So it is best to think of the global significance level as a good, but biased, estimate of the true Fourier power. The wavelet transforms clearly show the quasi-periodic nature of the oscillations in all wavelengths (agreeing with *Test 5*) where power at any frequency occurs in the form of wave-packets lasting for a few oscillations before disappearing. Its also clear that Ca II K_3 exhibits power around 3–4 mHz, whereas Mg I b_2 contains more power at lower frequencies (1.5–2 mHz)

Tables 5.2 – 5.5 contain a summary of the behaviour of each NBP. The top part of each table refers to peaks in the FFT power spectrum (and is hereafter referred to as an *FFT table*). It contains a summary of the behaviour of the NBP in each wavelength as a function of thresholding intensity (as in Chapter 4). The ‘99’ and ‘95’ refer to the fact that the power at this frequency reached at least the 99% and 95% confidence levels, respectively. Wavelet diagrams were then used to look at the duration of wave-packets

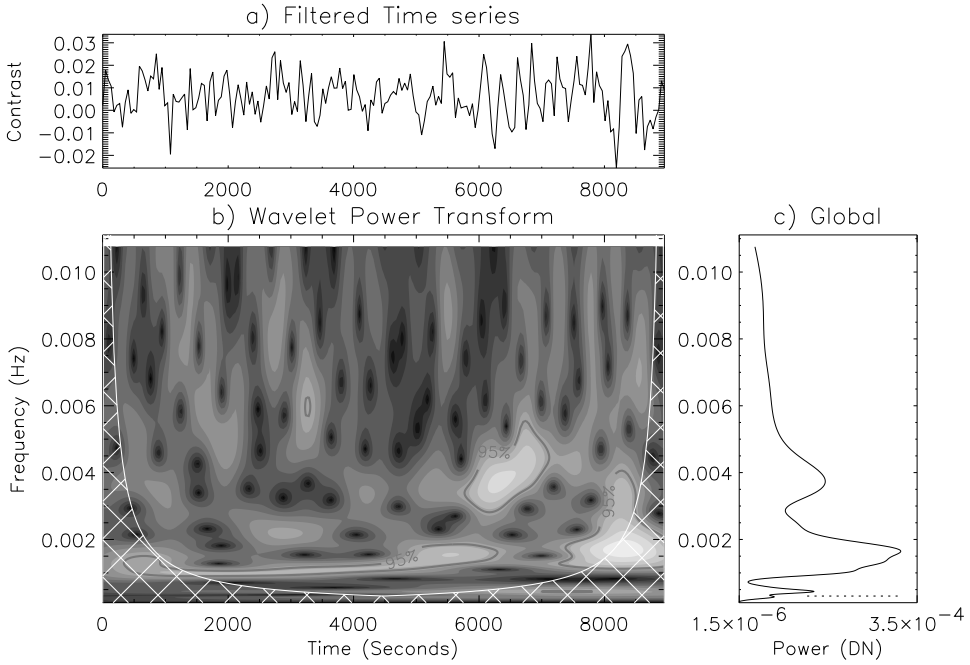

Figure 5.6: Example wavelet power transform for Mg I b_2 data. (a) Filtered light curve from the Mg I b_2 data for NBP2. (b) Wavelet power transform. The lighter an area, the stronger the oscillatory power. (c) The global wavelet spectrum.

at each peak in the FFT. For a frequency to be considered, it must last for at least one full oscillation outside the COI at greater than 95% confidence. Any frequencies which showed more than two complete oscillation periods are presented in bold type. Together with the FFT confidence level, this gives an indication of the strength and significance of any oscillations. As in Chapter 4 the frequency resolution of 0.11 mHz is used as the error in the FFT values, and hence all values are grouped in $\pm$ 0.11 mHz blocks, with the first row in the table corresponding to the lower limit, and second row to the upper limit (e.g. the first data column contains any peaks at 1.00, 1.11, and 1.22 mHz)

The bottom part of each table contains a summary of the possible travelling waves for each wavelength pair. Across every pair of wavelengths and for each frequency, the maximum correlation coefficient and corresponding timelag were recorded. Figure 5.7 shows the result of this procedure, and is now used to explain further steps. In Figure 5.7(a) there are two peaks above 1 mHz in the frequency-correlation curve: 1.3 mHz (correlation = 0.78) and 1.9 mHz (correlation = 0.68). By drawing horizontal lines from these peaks across into (b), the timelag-correlation curve, the corresponding timelags

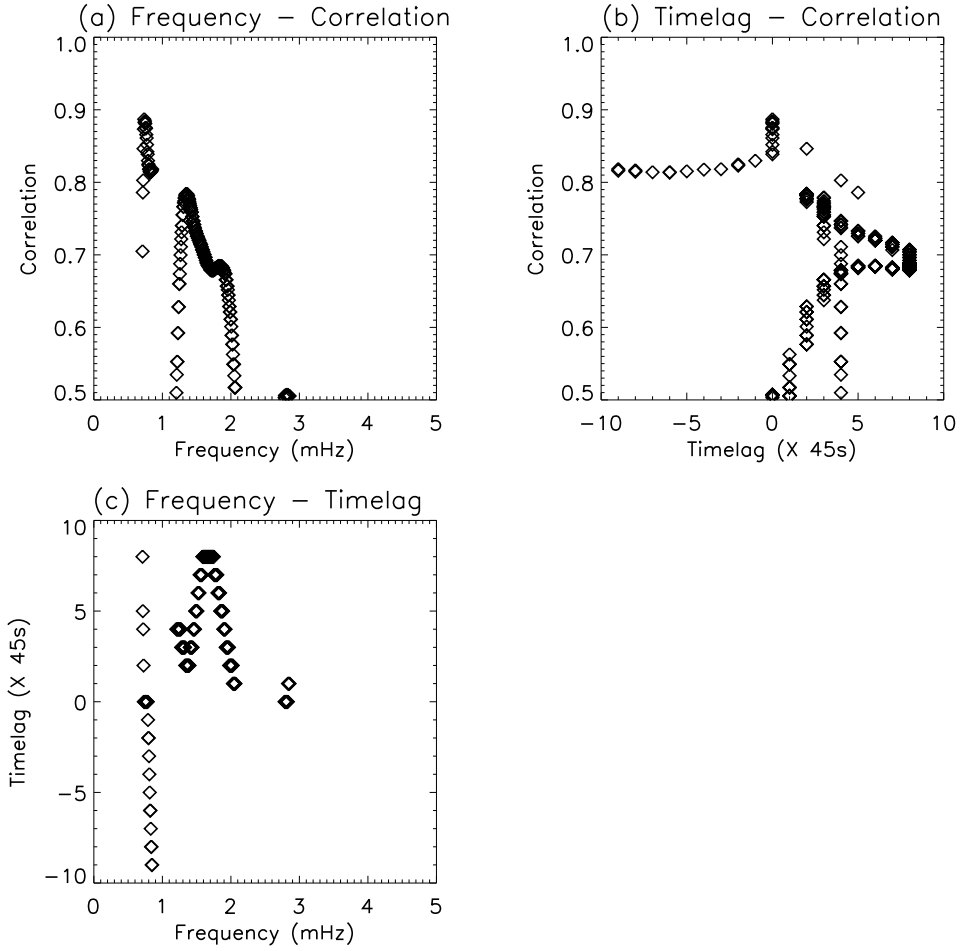

Figure 5.7: The three curves resulting from the correlation of the light curves of NBP2 in Ca II K_3 and Mg I b_2. (a) Peak correlation against frequency. (b) Peak correlation against timelag. (c) Timelag against frequency. The x-axis of (a) and (c) are the same. The y-axis of (a) and (b) are the same. Hence the timelag corresponding to the peaks in (a) can be determined by drawing horizontal and vertical lines across to (b) and down to (c) respectively.

can be obtained. This can also be achieved by drawing vertical lines from these peaks, down into (c), the frequency-timelag curve. Maxima in the frequency-correlation curve were retained only if the correlation was above 0.6, and the corresponding timelag was less than 450 s (10×45 s cadence). By individual inspection of the power curves, it is clear that correlations of greater than 10 time units could not be attributed to individual wave packets. Any correlations below 1 mHz were also disregarded, as the high-pass filter (Figure 4.5) used dictates that there will be no wave-packets remaining below this frequency. Wavelet analysis and Fourier transforms were both featureless above 5 mHz, so this is taken as the upper limit to search for correlations. The range of val-

ues given in correlation and timelag in Tables 5.2 – 5.5 is determined by the maximum and minimum correlation and timelag in the frequency range of the chosen frequency $\pm$ 0.1 mHz. The final column denotes the speed of the wave. It is noted that a data cadence of 45 s, combined with the spread in height estimates (Table 5.1) leads to a large range of speed estimates. A '$<$' symbol signifies a maximum speed, whereas a '+' symbol signifies the speed may be faster than the quoted value. It should also be noted here that a negative timelag refers to a downward speed, whereas a zero timelag could suggest either evanescent waves or upward- or downward- propagating waves, within the available time resolution.

Some general comments can be made, before concentrating on each NBP individually. In the lower atmosphere (e.g., Mg I $b_1 - 0.4$ Å), the oscillations are concentrated in the bright central portion of each NBP. However, in the upper chromospheric (e.g., Ca II K_3), there is a greater tendency for some oscillatory power to exist in the outer regions (i.e., further from the centre of the NBP). This is best demonstrated by the moving threshold FFTs (Chapter 4, Figure 4.7), where the sudden appearance of power at a particular threshold indicates that it is confined in the central portion only. It can be explained in terms of the magnetic canopy effect, whereby the magnetic field lines diverge in the upper chromosphere. The FFT tables also show a tendency for higher frequency power ($\sim$3 mHz) to exist in the upper chromosphere, with lower frequencies ($\sim$2 mHz) more powerful in the lower chromosphere. This is in general agreement with *Test 2*. The following four subsections contain a qualitative description of the wave behaviour found in each NBP, especially pertaining to the the five tests stated in Section 5.1

Table 5.2: Summary of frequencies (mHz) and correlations for NBP7. See Section 5.3.1 for details.

	From:	1.00	1.33	1.67	2.00	2.33	2.67	3.00	3.33	3.67	4.00	4.33
λ	To:	1.22	1.56	1.89	2.22	2.56	2.89	3.22	3.56	3.89	4.22	4.55
Ca II K_3		**99**	**95**	**99**	**99**							95,95
Hα		**99,99**	**99,95**		95,95				**99**			
Mg I b_2		**99**	**99,95**	**99,**95			95		**95**	**95**		**99**
Mg I $b_1-0.4$ Å		95,99	95,95,95	99		95		99				

λ_1	λ_2	Correlation Coefficient	Frequency (mHz)	Timelag (Units of 45 s)	Speed (km s^{-1})
Ca II K_3	Mg I b_2	0.66 – 0.72	1.5 –1.7	8–11	2–4
Ca II K_3	Mg I $b_1-0.4$ Å	0.81 – 0.91	1.3 – 1.5	0 – 3	12–40+
Hα	Mg I b_2	0.69 – 0.81	1.8 – 2.0	0 – -3	3–22+
		0.75 – 0.79	2.8 – 3.0	-1 – -3	3–22
		0.83 – 0.84	3.55 – 3.75	4 – 5	2–6
Hα	Mg I $b_1-0.4$ Å	0.72 – 0.81	1.8 – 2.0	1 – 2	11–33
Mg I b_2	Mg I $b_1-0.4$ Å	0.96 – 0.98	1.8 – 2.0	1 – 5	2–12
		0.69 – 0.70	3.3 – 3.5	2	5–6

Table 5.3: Summary of frequencies (mHz) and correlations for NBP2. See Section 5.3.2 for details.

	From:	1.00	1.33	1.67	2.00	2.33	2.67	3.00	3.33	3.67	4.00	4.33
λ	To:	1.22	1.56	1.89	2.22	2.56	2.89	3.22	3.56	3.89	4.22	4.55
Ca II K_3							**99,95**	99,95	99,95	**99**	**95**	**95**
Hα		**99**	**99**		**99**					**95**		**95**
Mg I b_2			**99,99**	**99,95**					**99,99**			**95**
Mg I $b_1-0.4$ Å		95,99	95,95	95,95	95							

λ_1	λ_2	Correlation Coefficient	Frequency (mHz)	Timelag (Units of 45 s)	Speed (km s^{-1})
Ca II K_3	Hα	0.72 – 0.76	2.4 – 2.6	0 – 4	0–17+
Ca II K_3	Mg I b_2	0.66 – 0.78	1.25 – 1.45	2 – 4	6–14
		0.68 – 0.68	1.75 – 1.95	3 – 8	3–10
Ca II K_3	Mg I $b_1-0.4$ Å	0.67 – 0.78	1.2 – 1.4	1 – 3	12–40
		0.70 – 0.73	1.7 – 1.9	7 – 11	3–6
Hα	Mg I b_2	0.65 – 0.67	2.97 – 3.17	1 – 2	5–22
		0.63 – 0.65	3.85 – 4.05	3	3–7
Hα	Mg I $b_1-0.4$ Å	0.61 – 0.62	3.2 – 3.4	5	4–7
		0.62 – 0.63	4.7 – 4.9	-2	11–16
Mg I b_2	Mg I $b_1-0.4$ Å	0.83 – 0.93	1.3 – 1.5	0 – 1	11+
		0.95 – 0.97	1.6 – 1.8	4 – 6	2–3
		0.94 – 0.94	4.2 – 4.4	-2	5–6

Table 5.4: Summary of frequencies (mHz) and correlations for NBP5. See Section 5.3.3 for details.

	From:	1.00	1.33	1.67	2.00	2.33	2.67	3.00	3.33	3.67	4.00	4.33
λ	To:	1.22	1.56	1.89	2.22	2.56	2.89	3.22	3.56	3.89	4.22	4.55
Ca II K_3		99,99,95			**99**		95		**99**	**95**		**95,95**
Hα		**99,95**	**99,**95		**99**		99			**95,95**	**95,99**	
Mg I b_2		**99,99**					**99**	**95**	**99**			**99**
Mg I $b_1-0.4$ Å		**99**	99,95		**99**		**95**	**99**	**95**			

λ_1	λ_2	Correlation Coefficient	Frequency (mHz)	Timelag (Units of 45 s)	Speed (km s^{-1})
Ca II K_3	Hα	0.82 – 0.84	3.65 – 3.85	-8 – -9	<2
		0.6 – 0.76	3.3 – 3.5	0 – 1	2+
Ca II K_3	Mg I b_2	0.64 – 0.76	0.9 – 1.1	-1 – -8	3–29
		0.56 – 0.77	1.05 – 1.25	0 – -1	23+
Ca II K_3	Mg I $b_1-0.4$ Å	0.58 – 0.60	4.55 – 4.75	-6 – -7	5–7
Hα	Mg I b_2	0.55 – 0.67	1.2 – 1.4	0 – -5	2-22+
Hα	Mg I $b_1-0.4$ Å	0.67 – 0.68	4.15 – 4.35	2	11-17
Mg I b_2	Mg I $b_1-0.4$ Å	0.80 – 0.86	1.48 – 1.68	0 – 2	6–12+
		0.62 – 0.63	4.0 – 4.2	-3	4

Table 5.5: Summary of frequencies (mHz) and correlations for NBP1. See Section 5.3.4 for details.

	From:	1.00	1.33	1.67	2.00	2.33	2.67	3.00	3.33	3.67	4.00
λ	To:	1.22	1.56	1.89	2.22	2.56	2.89	3.22	3.56	3.89	4.22
Ca II K_3							95	**99**	**99**		**95**
Hα		**99,95**	**99**		95		99			**99**	**99,95**
Mg I b_2		99,99					99	95	95		
Mg I $b_1-0.4$ Å		99	**99,95**		99		95	99	95		

λ_1	λ_2	Correlation Coefficient	Frequency (mHz)	Timelag (Units of 45 s)	Speed (km s^{-1})
Ca II K_3	Hα	0.66 – 0.79	1.2 – 1.4	-3 – -12	<6
		0.61 – 0.72	2.3 – 2.5	4 – 6	<4
Ca II K_3	Mg I b_2	0.68 – 0.75	1.9 – 2.1	0	
Ca II K_3	Mg I $b_1-0.4$ Å	0.57 – 0.62	1.73 – 1.93	3 – 7	5–13
Hα	Mg I b_2	0.77 – 0.84	1.2 – 1.4	-3 – -7	1–7
Hα	Mg I $b_1-0.4$ Å	0.69	4.1 – 4.3	3	7–11
Mg I b_2	Mg I $b_1-0.4$ Å	0.69 – 0.79	1.5 – 1.7	0 – 3	4–12+

5.3.1 NBP7 –Table 5.2

Correlations across Hα, Mg I b_2 and Mg I $b_1-0.4$ Å show a possible travelling wave at ∼1.9 mHz at a speed around c_S. The FFTs also reveal a strong peak around this frequency in the lower chromospheric lines, with a weaker peak in Hα, and the latter also show the appearance of a strong peak around 3.6 mHz. There is also a correlation around 3.6 mHz (Hα to Mg I b_2) and at 3.4 mHz (Mg I b_2 to Mg I $b_1-0.4$ Å). This is consistent with *Tests 1–4*, where a transverse wave at 1.9 mHz travels up through the atmosphere and couples to a longitudinal wave at around twice the original frequency when it reaches the height of Hα (core) formation temperature. This longitudinal wave then continues to travel upward and eventually shocks, explaining the lack of power at ∼3.5 mHz in Ca II K_3. The strong peaks at ∼2.0 mHz in Ca II K_3 are unexpected, but do not appear to be correlated with oscillations at the same frequency in the lower chromosphere.

In the 1.33–1.56 mHz range the oscillations are initially weak but increase in power in Mg I b_2 and Hα, before decreasing again in Ca II K_3. However, there is no power at twice this frequency in Ca II K_3, and the only correlation is between Ca II K_3 and Mg I $b_1-0.4$ Å. There is a downward- moving wave between Hα and Mg I b_2 (2.9 mHz) and a slow upward- moving wave between Ca II K_3 and Mg I b_2 (1.6 mHz). Below 1.3 mHz there is significant power in all wavelengths, but no indication of any correlation. Several frequencies seem to be localised in height, specifically the peaks around 2.5 mHz in the two lower lines, and the peaks at 4.4 mHz in Mg I b_2 and Ca II K_3. These may be driven by events spatially removed from the NBP at each height, e.g. granular overshoot (Lites *et al.* 1993).

5.3.2 NBP2 –Table 5.3

Correlations of Ca II K_3 to Mg I b_2 and Mg I $b_1-0.4$ Å, and Mg I b_2 to Mg I $b_1-0.4$ Å, reveal a possible travelling wave at $\sim$1.3 mHz. The FFTs also show power at this frequency, up to the Hα level. There is some power at the Ca II K_3 level, but it appears inside the COI and hence is not included here. However, Ca II K_3 does contain power around 2.8 mHz, and there is some correlation around 2.6 mHz between Ca II K_3 and Hα. This is all consistent with *Tests 1 to 4*, excepting the fact that there is no correlation from Hα to Mg I b_2. However, this lack of correlation shows the benefit of multi-wavelength analysis. Although the Hα to Mg I b_2 correlation is missing, we can safely rely on correlations across the other wavelengths. It is worth noting that a transverse frequency of 1.4 mHz, and longitudinal frequency of 2.8 mHz, are low compared to the suggestions of Kalkofen (1997).

The Ca II K_3 to Mg I b_2 and Mg I $b_1-0.4$ Å correlations, along with that of Mg I b_2 to Mg I $b_1-0.4$ Å, also show a possible $\sim$1.8 mHz wave. There is some power at this frequency in the lower lines and a weak peak in Hα at $\sim$3.8 mHz, with a possible travelling wave at $\sim$3.9mHz (Hα to Mg I b_2). However, there is no peak in the higher lying lines at the original frequency. Again, there is some power below 1.3 mHz, with no apparent correlation, and several frequencies seem to be localised in height (e.g., $\sim$3.4 mHz in Mg I b_2).

There are several other correlations evident between the lower lines. However in many cases, when the frequencies of these correlation peaks are compared to the FFT tables, there is no associated power in the FFT, or wave-packets in the wavelet power transforms. This demonstrates the advantage of using wavelet analysis to obtain temporal information and allows us to dismiss the 3.07 mHz (Hα to Mg I b_2), 3.3 mHz and 4.8 mHz (Hα to Mg I $b_1-0.4$ Å) correlations. The 4.3 mHz correlation (Mg I b_2 to Mg I $b_1-0.4$ Å) does correspond to a possible downward- moving wave-packet. Waves at around this frequency have been noted before (Bocchialini & Baudin 1995).

5.3.3 NBP5 –Table 5.4

In the 1.2–1.6 mHz range, there appear to be two different correlation patterns. A $\sim$1.3 mHz correlation (Ca II K_3 and Hα to Mg I b_2)corresponds to a decrease in power (and hence significance) of this frequency in the upper lines. There is also an appearance of signal at $\sim$2.7 mHz in Hα and Ca II K_3. Although this $\sim$2.7 mHz frequency also occurs in the lower lines, it seems to be uncorrelated to the upper lines. However there is a lack of correlation between Hα and Ca II K_3 at $\sim$2.7 mHz (*Test 4*) (although this could be due to the longitudinal wave shocking) and the waves may be downward-moving. Also, similar to NBP2, it is of a very low frequency compared to Kalkofen (1997). A $\sim$1.6 mHz correlation between Mg I b_2 and Mg I $b_1-0.4$ Å corresponds to a disappearance of power at this frequency from Mg I $b_1-0.4$ Å to Mg I b_2, as well as the existence of a $\sim$3.1 mHz oscillation in Mg I b_2. However, the lack of a remnant peak (*Test 1*) in the upper line makes this a less likely candidate for mode coupling. It would also have coupled too low in the atmosphere to be a viable candidate for chromospheric heating.

The correlation at 4.25 mHz (Hα to Mg I $b_1-0.4$ Å) corresponds to an appearance at this frequency in Hα, and could be the indication of a longitudinal wave appearing at this height. There is also power at 2.1 mHz in the lower lines. However, as there in no correlation at 2.1 mHz, and the power at this frequency does not decrease with height, this is not a good candidate for mode-coupling. There is a further upward- moving wave at 3.4 mHz (Ca II K_3 to Hα).

There appear to be three downward- moving waves at 1.0 mHz (Ca II K_3 to Mg I b_2), 3.75 mHz (Ca II K_3 to Hα) and 4.65 mHz (Ca II K_3 to Mg I $b_1-0.4$ Å), corresponding to wave-packets in each wavelength. Bocchialini & Baudin (1995) also found a downward- moving wave at 3.5 mHz using a similar method and invoked the magneto-gravity waves suggested by Deubner & Fleck (1990). The 4.1 mHz correlation (Mg I b_2 to Mg I $b_1-0.4$ Å) does not correspond to any wave-packets, and is thus dismissed as

not being real. Again, there seem to be a few oscillations which are localised in height, mainly in the range 2.67–3.56 mHz in Mg I b_2 and Mg I $b_1-0.4$ Å. For the frequencies around 3.33 mHz this could be due to some photospheric leakage. However, as this does not occur in all NBPs, it seems unlikely to be the case.

5.3.4 NBP1 –Table 5.5

The correlations between Ca II K_3 and both Mg I b_2 and Mg I $b_1-0.4$ Å show a possible travelling wave at $\sim$1.9 mHz (Mg I b_2 to Mg I $b_1-0.4$ Å also shows a correlation at a slightly lower frequency). This corresponds with an oscillatory signal at $\sim$1.9 mHz in Mg I $b_1-0.4$ Å and reduced power in Hα. There is also a peak at $\sim$4.0 mHz in Hα, which is reduced on reaching the Ca II K_3 level. Hα to Mg I $b_1-0.4$ Å shows a travelling wave at $\sim$4.1 mHz (*Test 4*). This all indicates a transverse wave of $\sim$1.9 mHz coupling to a longitudinal wave at $\sim$4.1 mHz, leaving behind a small remnant at the original frequency. This longitudinal wave then shocks, thereby explaining the lack of power in lines produced higher up in the chromosphere.

Again, there is also some weak evidence for downward- moving waves. A $\sim$1.3 mHz correlation is found (Ca II K_3 to Hα and Hα to Mg I b_2), although among these three wavelengths an oscillatory signal at this frequency is found in Hα only. Hence the correlation is not necessarily between wave packets. Similarly the $\sim$2.4 mHz correlation (Ca II K_3 to Hα) does not correspond to any wave-packet in either wavelength, and hence is dismissed. As in the other cases, a few frequencies exist which do not correspond to any waves. Below 1.3 mHz there is power up to the Hα level. As in NBP5 there are a lot of oscillatory power in the 2.67–3.56 mHz range which does not correspond to any travelling waves.

Table 5.6: Summary of propagating waves in all four NBPs. In each case the two wavelengths, wave frequency, and note as to possible mode-coupling transverse (MCT), mode-coupling longitudinal (MCL), upward (U), or downward (D) wave is given.

λ_1	λ_2	Frequency (mHz)	Notes
NBP7			
Hα	Mg I b_2	1.8 – 2.0	MCT
Hα	Mg I $b_1-0.4$ Å	1.8 – 2.0	MCT
Mg I b_2	Mg I $b_1-0.4$ Å	1.8 – 2.0	MCT
Mg I b_2	Mg I $b_1-0.4$ Å	3.3 – 3.5	MCL
Hα	Mg I b_2	3.55 – 3.75	MCL
Ca II K_3	Mg I $b_1-0.4$ Å	1.3 – 1.5	U
Ca II K_3	Mg I b_2	1.5 –1.7	U
Hα	Mg I b_2	2.8 – 3.0	D
NBP2			
Ca II K_3	Mg I b_2	1.25 – 1.45	MCT
Ca II K_3	Mg I $b_1-0.4$ Å	1.2 – 1.4	MCT
Mg I b_2	Mg I $b_1-0.4$ Å	1.3 – 1.5	MCT
Ca II K_3	Hα	2.4 – 2.6	MCL
Ca II K_3	Mg I b_2	1.75 – 1.95	U
Ca II K_3	Mg I $b_1-0.4$ Å	1.7 – 1.9	U
Mg I b_2	Mg I $b_1-0.4$ Å	1.6 – 1.8	U
Hα	Mg I b_2	3.85 – 4.05	U
Mg I b_2	Mg I $b_1-0.4$ Å	4.2 – 4.4	D
NBP5			
Ca II K_3	Mg I b_2	1.05 – 1.25	MCT
Hα	Mg I b_2	1.2 – 1.4	MCT
Mg I b_2	Mg I $b_1-0.4$ Å	1.5 – 1.7	MCT
Hα	Mg I $b_1-0.4$ Å	4.15 – 4.35	U
Ca II K_3	Hα	3.3 – 3.5	U
Ca II K_3	Mg I b_2	0.9 – 1.1	D
Ca II K_3	Hα	3.65 – 3.85	D
Ca II K_3	Mg I $b_1-0.4$ Å	4.55 – 4.75	D
NBP1			
Ca II K_3	Mg I b_2	1.9 – 2.1	MCT
Ca II K_3	Mg I $b_1-0.4$ Å	1.7 – 1.9	MCT
Mg I b_2	Mg I $b_1-0.4$ Å	1.5 – 1.7	MCT
Hα	Mg I $b_1-0.4$ Å	4.1 – 4.3	MCL
Ca II K_3	Hα	1.2 – 1.4	D
Hα	Mg I b_2	1.2 – 1.4	D

5.4 Discussion

A summary of all the propagating waves in each NBP is provided in Table 5.6. The ordering of the waves in this table, and notes as to whether each wave may be a possible mode-coupling candidate, or simply an upward- or downward- moving wave reflects the discussion in Sections 5.3.1 to 5.3.4. Correlations which do not correspond to wave packets are omitted.

In each NBP, there is at least one frequency which satisfies the five tests described in Section 5.1. However, a few points must be addressed concerning this. Firstly, Kalkofen (1997) suggests that transverse waves should not normally be viewable at disk centre. If they are viewable it will be due to a flux tube which, being slightly slanted, will make a small angle with the line-of-sight. In this case the resulting light curve will have two maxima for each complete oscillation of the wave and hence the frequency detected will be twice that of the wave. However, this will only be true for completely symmetrical profiles. If the line profile is asymmetric, or if the filter is in the wing of the line, the Doppler shift from the transverse wave will result in a light curve which will still contain a signal at the original transverse wave frequency.

Secondly, the main area of disagreement with theory is in the values of the cut-off frequencies determined from Kalkofen (1997). As stated in Section 5.1 it should be noted that the cut-offs calculated have not been derived specifically for the network. In the network several parameters may vary, due to the highly magnetised structure and local depression, or non-adiabatic effects, which may alter ν_k. A complete understanding of the structure within the network is necessary, which may introduce other factors into the equations given by Kalkofen (1997) for the cut-off frequencies. It is also apparent that the thin flux tube approximation will not be appropriate in the high chromosphere. Further modelling using thick flux tubes will be necessary. The results here suggest transverse cut-offs of $\sim$1.3 mHz, and $\sim$1.9 mHz, with longitudinal cut-offs at around twice these frequencies. Hasan & Kalkofen (1999) suggest cut-off periods of 534 s

and 227 s for the transverse and longitudinal mode respectively, which agree with the higher frequency (1.9 mHz) cut-off suggested here.

Thirdly, results such as those presented here have never before been so clearly demonstrated. There are several reasons for this. It is important to note that our method uses 2-dimensional images, making it easier to spatially isolate the NBP throughout the entire time series (as first pointed out by Cauzzi *et al.* 2000). The contour method also ensures only pixels inside the NBP are included, ignoring any other bright pixels in the FOV. In addition, some oscillatory components can be missed if each NBP is not followed completely from the outer reaches to the bright centre. In Chapter 4 I demonstrated how spatially averaging over many NBPs can lead to overlooking power at several frequencies. The contrast light curve and digital high-pass filtering techniques used here also remove all very low frequency power which can dominate the power spectrum (Figures 4.5 and 4.4). It is of course important to remove this low-frequency component without unduly affecting the higher frequencies. It is also of note that the time series used here (150 minutes) is longer than most previous studies. Most importantly, the use of wavelet analysis to create the power curves gives temporal information associated with any wave-packets. A Fourier phase analysis, which will average over time, may result in any correlation across wave-packets being 'washed out' by the longer non-periodic component. This may explain the lack of correlation found in previous work (e.g., Lites *et al.* 1993). It is also important to note the multi-wavelength nature of the data used in this study. Although a few papers have previously performed correlations across wavelet power diagrams (Bocchialini & Baudin 1995; Baudin, Bocchialini, & Koutchmy 1996), they have used only two wavelengths in a limited frequency range. Using four wavelengths across all observable frequencies gives a much higher chance of detecting correlated oscillations, and makes the findings more significant.

Finally, the results reported here suggest longitudinal waves shock in the mid- to high- chromosphere, hence heating the surrounding plasma, and the oscillations subsequently disappear. However simulations by Carlsson & Stein (1992) of K_{2V} grains

suggest that these shocks may be coherent which will lead to further oscillations at 5.5 mHz. This lack of agreement suggests that either the magnetic network differs from the internetwork bright points, or the coherence area must be well less than the areas integrated over in this paper.

In this chapter I have used a novel combination of wavelet analysis and cross-correlation to study propagating waves in the chromosphere. For each NBP studied I have found the possibility of transverse wave propagation in the lower chromosphere. There is also evidence of these transverse waves coupling to longitudinal waves in the upper chromosphere, which can then shock. Thus mode-coupling provides a means of energy transport to heat the upper chromosphere. In the next chapter I will present another novel wavelet analysis technique to study oscillatory signals in *TRACE* ultra-violet datasets.

Chapter 6

Oscillations in TRACE Observations of the Quiet-Sun Chromosphere

Quiet-Sun oscillations in the four *TRACE* ultraviolet passbands centred on 1700 Å, 1600 Å, 1216 Å and 1550 Å are studied using a wavelet-based technique. Both network and internetwork regions show oscillations with a variety of periods and lifetimes in all passbands. The most frequent network oscillation has a period of 283 s with a lifetime of 2–3 cycles in all passbands. These oscillations are discussed in terms of upwardly-propagating magnetohydrodynamic wave models. The most frequent internetwork oscillation has a period of 252 s, again with a lifetime of 2–3 cycles, in all passbands. The tendency for these oscillations to recur in the same position is discussed in terms of 'persistent flashers'. The network contains greater oscillatory power than the internetwork at periods longer than 300 s in the low chromosphere. This value is shown to decrease to 250 s in the high chromosphere. The internetwork also displays a larger number of short-lifetime, long-period oscillations than the network, especially in the low chromosphere. Both network and internetwork regions contain a small number of non-recurring long-lifetime oscillations.

6.1 Introduction

This chapter presents an automated wavelet analysis approach to *TRACE* quiet-Sun UV intensity oscillations for both the network and internetwork. This idea was originally applied to Coronal Diagnostic Spectrometer (CDS, Harrison *et al.* 1995) data by Ireland *et al.* 1999. The oscillations in each region are discussed in relation to chromospheric heating via waves discussed in Chapter 2. When studying quiet-Sun data, wavelet analysis has two specific benefits over the Fourier transform. Firstly, the intermittency of the oscillations present (Banerjee *et al.* 2001; Hansteen, Betta, & Carlsson 2000) means that their Fourier power may be swamped by the much longer non-periodic component, whereas wavelet analysis provides localised temporal information. Secondly, quiet-Sun

datasets are difficult to align compared to active region datasets due to a relative lack of features. Again the time-localised nature of wavelet analysis is better suited than Fourier analysis in dealing with frames which may not be perfectly aligned (Ireland *et al.* 1999). In order to reduce alignment problems, *TRACE* was used to provide long duration observations of the Sun, free of atmospheric distortions. The large FOV of *TRACE* makes it very useful for quiet-Sun studies, where it provides a larger spatial sample than slit-based spectrometers (e.g., SUMER, CDS). The large passbands of *TRACE* also mean that any oscillations present are free from Doppler-shift effects due to plasma motions. Oscillations must therefore be due to changes in temperature and/or density. However, it is noted that the wide passbands make it difficult to estimate their height of formation (HOF), as each passband contains significant contributions from continuum in addition to line emission. The wide passbands may also lead to phase averaging.

As discussed in Chapter 1, the quiet Sun displays a distinct network appearance identical to the supergranular cell structure in Dopplergrams (Leighton, Noyes, & Simon 1962). The nature of supergranular flow results in magnetic flux coalescing at cell vertices, with replenishment of flux occurring on the scale of a few days to a week (Schrijver *et al.* 1998). This creates a dense collection of flux tubes (Berger *et al.* 1998; Lites, Rutten, & Berger 1999) at these vertices and is observable as kilogauss fields in magnetograms. In time-integrated UV images of the chromosphere, the network is only partially defined as patches of increased intensity (NBPs), which display a one-to-one spatial correlation with this underlying photospheric magnetic field (similar to optical wavelengths; Figure 5.1). On the other hand, the internetwork is mainly field-free, and appears dark on time-integrated images of the chromosphere.

This spatial dichotomy between the network and internetwork is also apparent in the Fourier spectrum of light curves from these two regions, leading to the suggestion that different heating mechanisms may dominate in each region (Gallagher *et al.* 1999). The internetwork contains oscillations with periodicities around 180 s (a broad 3–8 mHz

peak in the Fourier spectrum: the acoustic band), intermittently present in small grains, and with a good correlation between the photosphere and the chromosphere (Lites *et al.* 1993). Some work shows the existence of nodal planes and hence standing waves (e.g., Kneer & von Uexküll 1993; Deubner, Waldschik, & Steffens 1996). Other studies show a directly proportional increase of phase lag with frequency between lines formed at different heights in the atmosphere (e.g., Judge *et al.* 2001; Wikstøl *et al.* 2000). This suggests the presence of upwardly-propagating acoustic waves, which have been successfully modelled by Carlsson & Stein (1992; 1995; 1997). Brandt *et al.* (1992) suggest a scenario whereby there are two types of grains: one with a long term memory, termed 'persistent flashers', with a magnetic dependence; and a second, 5–10 times more common, with no spatial memory or magnetic dependence. This may explain the difference between the conclusions reached by Worden, Harvey, & Shine (1999) and Lites *et al.* (1999), who suggest no correlation between the small internetwork magnetic fields and the chromospheric grains, and those of Sivaraman *et al.* (2000) who found a strong correlation between the internetwork grains and magnetic fields.

Longer-period network oscillations (5–20 mins) have not benefited from such similarly detailed simulations, mainly due to the difficulty of modelling the chromospheric plasma in the presence of the kilogauss magnetic fields (Bogdan *et al.* 2003). Current theories of network heating suggest that the magnetic field is critical and these fall into three main categories:

(i) *in situ* resistive dissipation from the stochastic rearrangement of magnetic field lines (Kneer & von Uexküll 1985; 1986);

(ii) upwardly-propagating transverse magnetohydrodynamic (MHD) waves coupling, and hence transferring power, to longitudinal waves, which can then form shocks (Kalkofen 1997; Hasan & Kalkofen 1999; Hasan *et al.* 2003);

(iii) resistive dissipation of Pedersen currents, driven by longitudinal MHD waves (Goodman 2000).

Observations show a poor temporal correlation between chromospheric network oscillations and those in the underlying photosphere (Lites *et al.* 1993). However in Chap-

Table 6.1: Details of the *TRACE* dataset used in this chapter (Krijger *et al.* 2003)

Date	1999 May 04
Image Size (px)	256×640
Image Size ($''$)	128×320
Time (UT)	08:08 – 11:52
1700Å exposure (s)	2.0479
1600Å exposure (s)	1.0239
1216Å exposure (s)	2.1538
1550Å exposure (s)	5.7919
Effective cadence (s)	40.05

ter 5 I have shown how wavelet-based studies (also Bocchialini & Baudin 1995; Baudin, Bocchialini, & Koutchmy 1996) show the existence of mainly upwardly-propagating (but also some downwardly-propagating) waves in the chromosphere at speeds close to the sound speed. Furthermore, the tendency of oscillations to occur in the very centre of network elements (as shown in Chapter 4), combined with a lack of both intensity and oscillatory power near, but not directly above, photospheric network elements (termed 'magnetic shadows'), suggests the existence of mode-conversion of acoustic waves as they interact with the magnetic canopy (Judge *et al.* 2001; McIntosh & Judge 2001; McIntosh, Fleck, & Judge 2003).

The outline of this chapter is as follows. An overview of the dataset, including a discussion of the HOF of each passband, is presented in Section 6.2. The alignment procedure, creation of the network/internetwork subsets and high-pass filtering are discussed in Section 6.3. This is followed by a detailed description of the wavelet analysis routine designed to search for both periodicity and lifetime of any oscillations in all the pixels in each subset. Section 6.4 compares the differing results from the network and internetwork, while conclusions are given in Section 6.5.

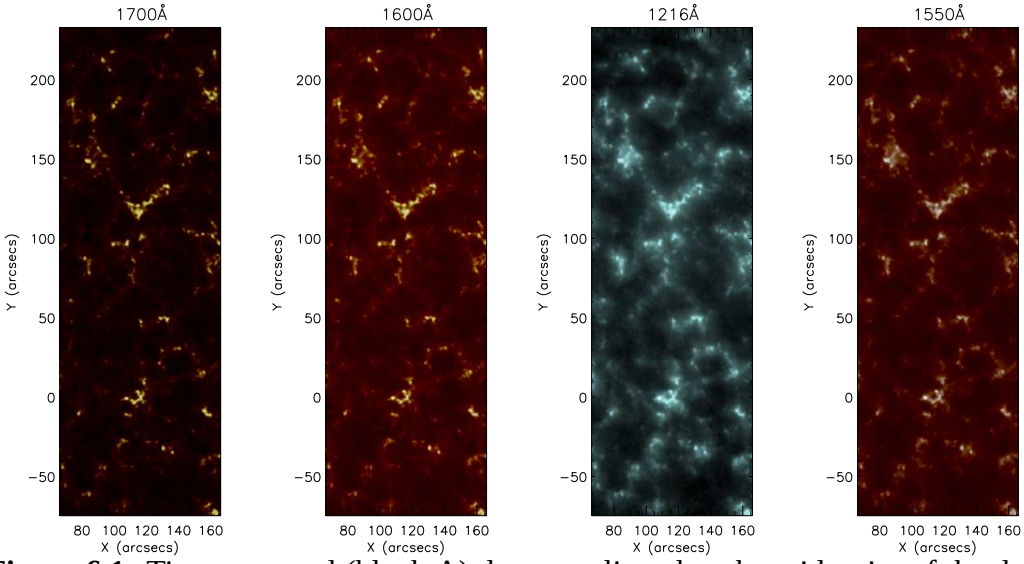

Figure 6.1: Time averaged (block A) data, co-aligned to the mid-point of the dataset. From left to right in order of increasing HOF: 1700Å, 1600Å, 1216Å, 1550Å.

6.2 Observations

A dataset from 1999 May 4 containing quiet-Sun images in the four UV passbands (1700 Å, 1600 Å, 1216 Å, 1550 Å) with a FOV of $128'' \times 320''$ was selected for this study. Further details of the dataset can be found in Table 6.1, and example time-average images are displayed in Figure 6.1. A simple investigation into the frame rate stability in each passband resulted in a constant cadence of 40.05 s being assumed for the purpose of both Fourier and wavelet analyses. After image 168 there was a 50 s delay, corresponding to a small change in the FOV as *TRACE* compensated for solar rotation. For this reason the data were divided into two equal timeblocks; block A containing images 1–168 and block B containing images 169–336. This creation of two data blocks was also vital for data analysis (Sections 6.3.1 and 6.3.2) and to the search for oscillation recurrence (Section 6.4.3). In some cases there were 80 s time gaps between images. It was assumed this was due to a missing image. These missing images were replaced by an average of the (aligned) preceding and following images. Any images severely contaminated by cosmic rays were cleaned using programs available in the *TRACE* branch of SSW.

6.2.1 Heights of Formation

There are well-known difficulties associated with attributing specific HOFs to emission from broadband filters. Due to the complexity of line emission and continuum, any HOF will vary in both time (e.g., during a flare) and space (e.g., plage/network – internetwork). Whilst realising the limitations of any assigned HOF we suggest the following. Previous work with *TRACE* UV data (Judge *et al.* 2001; Krijger *et al.* 2001; Handy *et al.* 1999a) place the 1700 Å band lowest in the atmosphere (UV continuum at $\sim$4–10$\times10^3$K, below temperature minimum), followed by the 1600 Å passband (UV continuum at $\sim$4-10$\times10^3$K plus Fe II at $\sim$1.3$\times10^4$K, temperature minimum). Up to 50% of the signal in the 1216 Å passband is also believed to be UV continuum (Worden *et al.* 1999) suggesting a HOF around the mid chromosphere (50% Lyα at $\sim$1-3$\times10^4$K, plus 50% UV continuum). The 1550 Å passband has the highest HOF, at $\sim1\times10^5$K, but with sigificant contributions from other lines (e.g., Si II at $\sim1\times10^4$K) and continuum. These temperatures are approximate and there is expected to be a degree of overlapping emission between passbands. However in order to carry out a qualitative discussion of our results, we assume a sequence of increasing HOF of 1700 Å, 1600 Å, 1216 Å, 1550 Å.

Techniques have been developed to separate both the Lyα (Handy *et al.* 1999b) and C IV (Handy *et al.* 1998) emission from the continuum. However in both cases it has been shown that these techniques are only reliable for more intense solar features (e.g., Figure 6 of Handy *et al.* 1998). The bright network will be at the lower limit of this intensity, and the techniques are certainly not applicable to the internetwork without long exposure times. As we wish to compare network and internetwork oscillations we decided not to apply any continuum removal to the data.

6.3 Data Analysis

6.3.1 Alignment

The division of the data into two blocks was vital to compensate for solar differential rotation in the dataset (estimated as $1''$ over each 167 image block). Initially all wavelengths were aligned by calculating the offsets of the middle image of each block to the corresponding 1600 Å image, and shifting all images in each wavelength correspondingly. At each wavelength, all images were then aligned to the middle image of the timeseries using cross-correlation programs available in SSW. Any large offsets were replaced by the average of the preceding and following offsets, and the cross-correlation repeated until all offsets were less than 0.2 pixels (i.e., $0.1''$). This procedure was carried out for each block separately. Finally, the offset of the middle image of block A to block B was found using the same cross-correlation procedure and all block B data were shifted by this offset. This resulted in the entire timeseries, in all four UV wavelengths, being aligned to within $0.1''$. Due to solar rotation, several pixel rows and columns were not always present in the data, so that the aligned data FOV was reduced from 256×640 pixels^2 to 215×600 pixels^2.

6.3.2 Creation of Network and Internetwork Subsets

The nature of the network to appear bright in time-averaged images is used to define a network/internetwork mask in a method similar to Krijger *et al.* (2001). For the aligned 1600 Å data, a time-averaged image was created for each block. For each time-averaged image, a histogram of pixel values was created. Pixels with an intensity below the modal intensity value were defined as internetwork, while those with an intensity value greater than one standard deviation above the mean intensity value were defined as network (Chapter 4 this thesis; Worden *et al.* 1999). The subsequent network pixel arrays for block A and block B were compared, and only pixels defined as network in

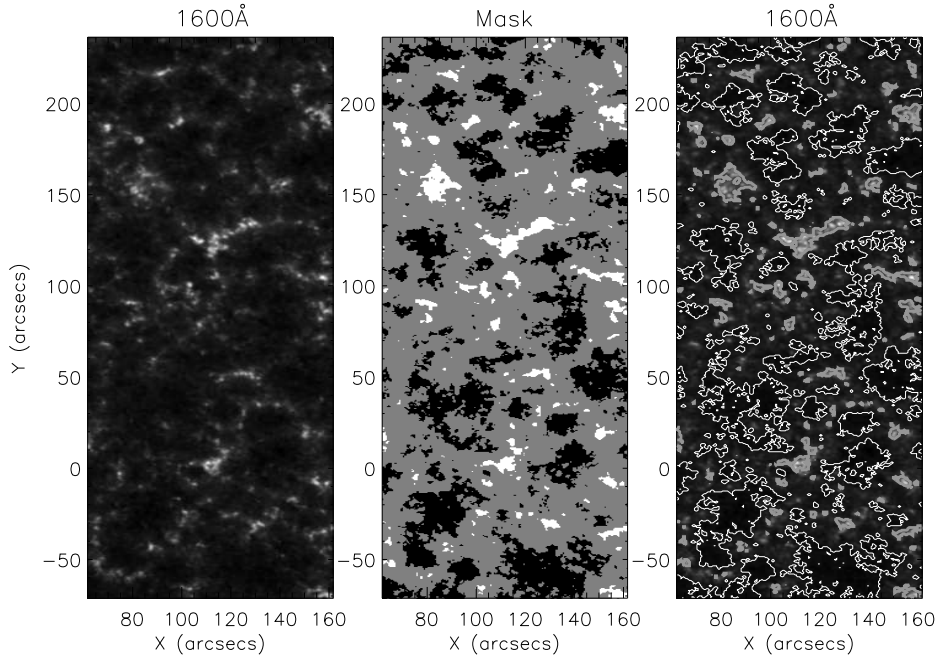

Figure 6.2: Network and internetwork masks. Left: Time averaged (data block A) 1600 Å image. Middle: The network (white) and internetwork (black) masks. Right: Network (bright) and internetwork (dark) pixels are contoured.

both datablocks were retained. A similar process was carried out for the internetwork. The resulting network and internetwork pixels are displayed in Figure 6.2. The leftmost image is the time-averaged 1600 Å block A, where the network appears as bright clusters at supergranular cell vertices. The network and internetwork pixels are contoured in the rightmost image, according to the masks in the middle image (where white is the network mask and black is internetwork mask). These masks were then applied to all the data, resulting in 28717 internetwork light curves, and 5999 network light curves in each of the four UV passbands.

6.3.3 Filtering

With 167 images at 40.05 s cadence, the Nyquist frequency is 11.1 mHz and the frequency resolution is 0.13 mHz. After subtracting the mean this provides a range of detectable periodicity of 90–7692 s. A high-pass filter was employed such that all

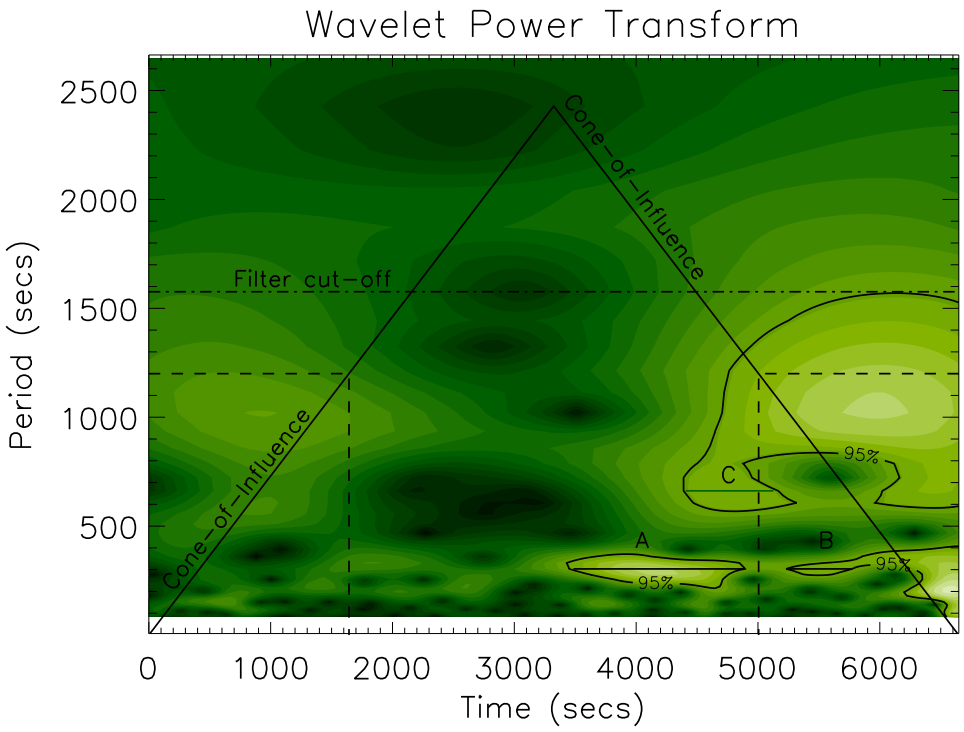

Figure 6.3: Wavelet power transform of a typical network light curve.

Fourier power below ∼0.6 mHz (above ∼1642 s in period space, corresponding to the maximum possible detectable period, see Section 6.3.4, Eqn. 6.3 and Figure 6.3) was removed. The importance of filtering is to increase the significance of the expected peak around 3–5 min by reducing aliasing effects. Filtering was carried out on each light curve by convolution with a suitable Bessel function so as to provide a smooth edge to the filter profile, and hence reduce ringing effects.

6.3.4 Wavelet Analysis

Similar to Chapter 5 a wavelet analysis was carried out on each light curve using a Morlet wavelet of the form,

$$\psi(\eta) = \pi^{-1/4} \exp(i\omega_0\eta) \exp\left(\frac{-\eta^2}{2}\right) . \tag{6.1}$$

For the Morlet wavelet, the Fourier period is ∼1.03 times the wavelet scale (Torrence & Compo 1998). A typical wavelet power transform (square of the absolute value of

the wavelet transform) for a network light curve is shown in Figure 6.3. In Chapter 5 the wavelet power transform is plotted as frequency against time (see Figures 5.5 and 5.6). However for the work in this present chapter it more apt to plot period against time. Hence in Figure 6.3 the abscissa is time, t, and the ordinate is period, P. This is displayed on a linear intensity scale, such that brighter areas correspond to greater oscillatory power. The contours are at the 95% significance level and the two slanted lines define the cone-of-influence (COI). Edge effects are significant above these two lines. The extent of the COI, from the beginning and the end of the time series, at each period P, is defined in Torrence & Compo (1998) for the Morlet wavelet, as the decorrelation time for a spike in the time series, $t_d = \sqrt{2}P/1.03$ s . For example, for the dashed lines on Figure 6.3 at P = 1200 s, the COI extends from t = 0–1647 s, and from t = 5001–6648 s. After creating the wavelet power transform, an automated routine calculated the lifetime and periodicity of any oscillations following the procedure first described in Ireland *et al.* (1999). First, all power below the 95% significance level or above the COI lines was removed. The routine then searches for any remaining power maxima. The lifetime of the oscillation at the period of each power maximum is defined as the interval of time from when the power reaches above 95% significance to when it dips below 95% significance again. The lifetime was then divided by the period to give a lifetime in terms of complete cycles. For example, for the oscillatory power in contour A in Figure 6.3, the lifetime is given by (4900-3500)/300 = 4.67 cycles. Any oscillations lasting for less than t_d (e.g., for the maxima in contour C in Figure 6.3, lifetime = (5100-4400)/650 = 1.08 cycles) were discarded as possibly being due to a spike in the time series. From the criterion of a lifetime of at least $\sqrt{2}P/1.03$ outside the COI (of size $2\sqrt{2}P/1.03$), the maximum possible detectable period, P_{max}, can be obtained from,

$$\frac{3\sqrt{2}\,\mathrm{P}_{max}}{1.03} = \delta\mathrm{t} \times (\mathrm{N}-1)\ , \tag{6.2}$$

where δt is the cadence, and N is the number of data points in the light curve (hence $\delta\mathrm{t} \times (\mathrm{N}-1)$ is the total duration of the light curve). Rearranging for the dataset used

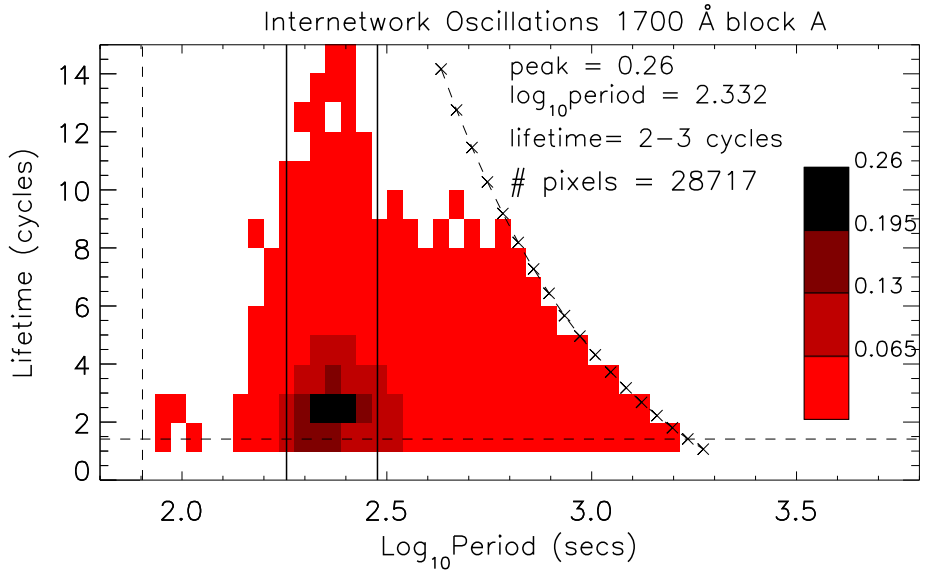

Figure 6.4: Summary of all internetwork oscillations for the 1700 Å block A dataset. The frequency of occurrence of any oscillation at each period and lifetime is plotted according to the intensity scale on the right.

here,

$$\mathrm{P}_{max} = \frac{1.03 \times 40.05 \times 167}{3\sqrt{2}} = 1642 \text{ s} . \tag{6.3}$$

In Figure 6.3 P_{max} is shown as the dash–dot line, and is the value used as the cut-off for the high pass filter (Section 6.3.3). The final output from the routine is a list of lifetimes and periodicities for all oscillations in each input light curve.

6.4 Results

6.4.1 Internetwork Oscillations

A summary of all internetwork oscillations for the first half (block A) of the 1700 Å data is shown in Figure 6.4. Here the ordinate is the period, P, as determined from the wavelet analysis. The nature of wavelet analysis means that the values of period increase logarithmically. The abscissa, l, is the oscillation lifetime binned to integer values. For example, the lifetime of 4.67 cycles discussed above is placed in the 4–5

bin. The horizontal dashed line is at $\sqrt{2}/1.03$ cycles (minimum lifetime), the vertical dashed line is at the Nyquist frequency, while the two solid vertical lines are at 3 and 5 min. The curved dashed line refers to the maximum number of complete cycles which can be observed at each period (due to the finite length of the time series). Figure 6.4 is plotted on a inverted linear intensity scale, such that darker areas correspond to a larger number of pixels with oscillations at period P, for lifetime l. The four colour bands refer to the upper quartile (black; $>$ 75% of peak value), mid-upper quartile (dark red; 50–75% of peak value), mid-lower quartile (brighter red; 25–50% of peak value) and lower quartile (bright red; $<$ 25% of peak value). The data have been divided by the number of pixels (hence number of light curves), to make all results from the network and internetwork directly comparable. It should be noted that oscillations in the bright red areas *are not* less significant than those in the black areas – the rules regarding significance are the same for all oscillations. Instead, oscillations in the bright red areas are less common than those in the black areas. This is an important distinction between the wavelet studies and the results from Fourier analysis.

Figure 6.4 displays several interesting features. The most common oscillation is a well defined peak with a period of $\log_{10}(P)$ = 2.33 ($P \sim$ 210 s), lasting for 2–3 cycles, with an occurrence rate of 0.26 (i.e., 1 in 4 pixels contain an oscillation at this period for this lifetime). There are few oscillations below $\log_{10}(P)$ = 2.2 ($P \sim$ 160 s), and all the long-lifetime oscillations (LLOs; defined as $>$8 cycles) occur near the acoustic band (i.e., $\log_{10}(P) \sim$ 2.2–2.5). The internetwork results from the other UV passbands display a similar behaviour.

By summing Figure 6.4 over the lifetime axis we can create occurrence rate curves which are directly comparable to the average Fourier power curves (Figure 6.5). These occurrence rate curves have also been divided by a probability correction curve, to account for the fact that short-period oscillations are more likely to be observed (less time to undergo $\sqrt{2}/1.03$ cycles, and more light curve outside the COI). In Figure 6.5 the ordinate is the occurrence per pixel (i.e., average number of cycles) for the top

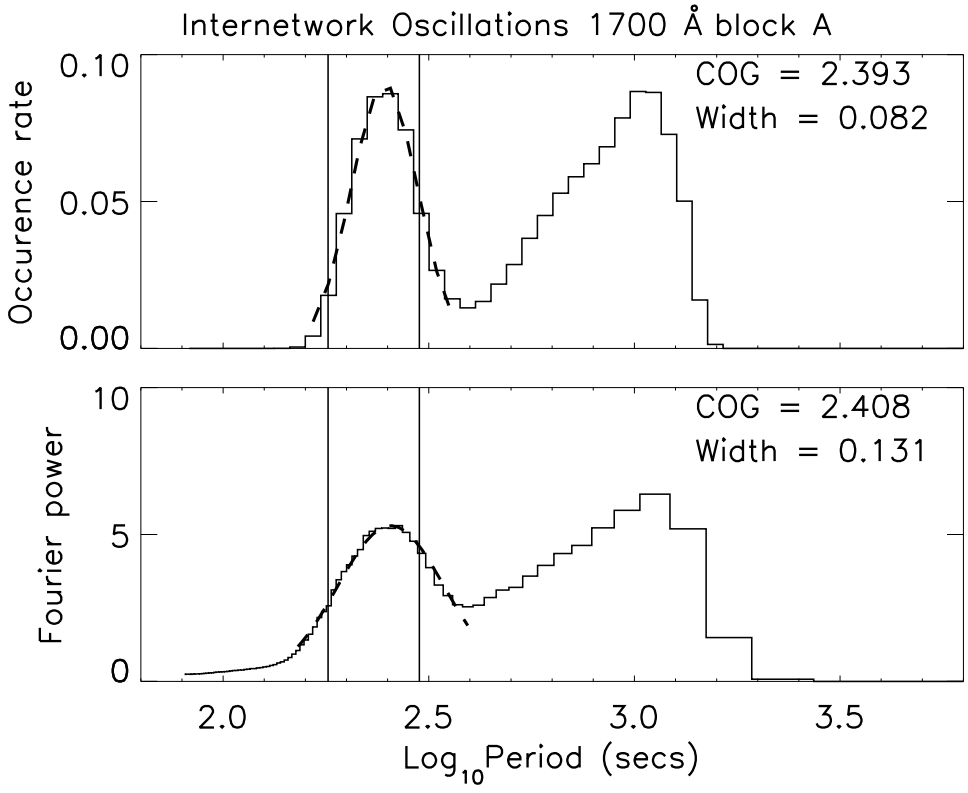

Figure 6.5: Internetwork occurrence rate and Fourier power in the 1700 Å block A dataset. Top: occurrence rate per pixel at each period. Bottom: Average Fourier power per pixel at each period. In both diagrams, a Gaussian fit is applied to the feature around $\log_{10}(P) = 2.4$, and the centre of this Gaussian fit is displayed at the top right.

panel, and average Fourier power per pixel for the bottom panel. Both panels share the same abscissa as Figure 6.4, namely period on a log scale. Again the two vertical lines are at 3 and 5 min.

Although the curves in Figure 6.4 are comparable, the distinct Fourier – wavelet difference still exists. In the top part of Figure 6.4 all the oscillations are equally significant – all oscillations have a >95% significance for at least $t = t_d$. However in the bottom part, the Fourier power defines the significance. As these are normalised Fourier power spectra, the 95% significance level is at 5.99 (see Chapter 4). Hence although the oscillations with $\log_{10}(P) = 2.6$ are all above 95% significance in the wavelet study, their average Fourier power is well below 95%.

A simple Gaussian fit (i.e., with no continuum) has been applied to the feature around the acoustic band and overplotted in each case. The Gaussian fit was applied

to the region of the curve from where it rises above zero, to the minimum around $\log_{10}(P)$ = 2.6. The value of the centre of the Gaussian fit (COG), and one sigma width are displayed in the top right corner of each plot. It should be noted that this width is an indication of the spread of frequencies around the peak. The estimated error in the determination of the position of the centre of the Gaussian is typically around 0.005 in $\log_{10}(P)$ (i.e., $\delta P \sim$ 4 s), and hence much smaller than the one sigma width.

Figure 6.5 shows the good agreement between the wavelet analysis and classical Fourier approach. It displays a rise of power (Fourier) and occurrence rate (wavelet) with increasing period, reaching a maximum around $\log_{10}(P)$ = 2.4 ($P \sim$ 250 s). This value differs from the peak in Figure 6.4 because of the probability correction curve applied to the data. Both curves reach a minimum around $\log_{10}(P)$ = 2.6 ($P \sim$ 400 s), followed by a gradual increase at higher periods. Using phase analysis techniques, Krijger *et al.* (2001) attribute this high period power primarily to internal gravity waves, with some contribution from granular overshoot and the low-frequency tail of acoustic interference. The fall-off at $\log_{10}(P) > 3.0$ is due to the high-pass filter applied to the light curves.

6.4.2 Network Oscillations

A summary of all network pixel oscillations from the first half of the 1700 Å data is displayed in Figure 6.6. In contrast to the results from the internetwork pixels, the most common network oscillation is a well defined peak with a longer period of $\log_{10}(P)$ = 2.41 ($P \sim$ 260 s), lasting for 2–3 cycles, with a lower occurrence rate of 0.19 (i.e., 1 in 5 pixels contain an oscillation at this period for this lifetime; the distribution of the occurrence rate is broader in the network). As in the internetwork, there are few oscillations below $\log_{10}(P)$ = 2.2 ($P \sim$ 160 s), and all the LLOs occur near the acoustic band. However, the network contains an extended tail at the 25–50% level up to periods of $\log_{10}(P)$ = 2.9 ($P \sim$ 800 s). Hasan & Kalkofen (1999) suggest a sce-

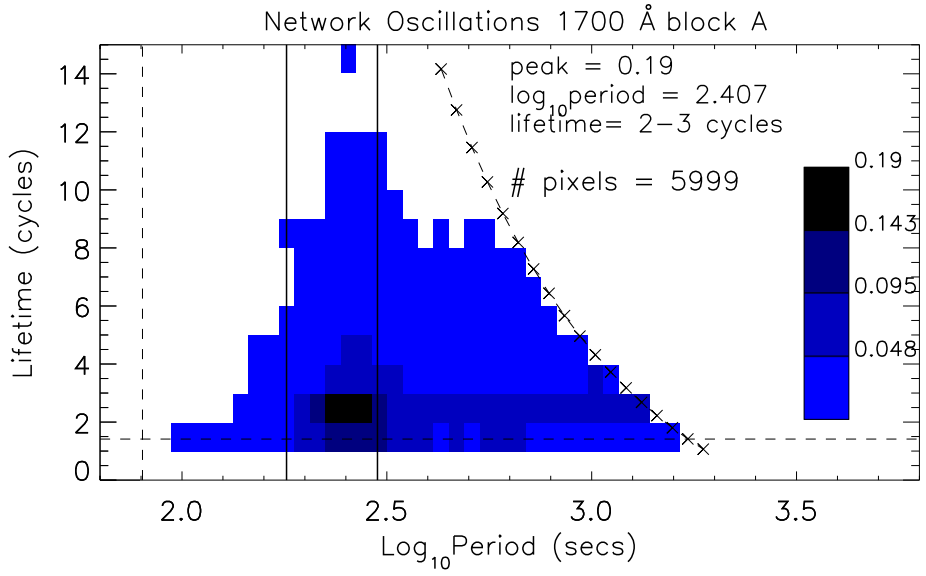

Figure 6.6: Summary of all network oscillations for the 1700 Å block A dataset. The frequency of occurrence of any oscillation at each period and lifetime is plotted according to the intensity scale on the right.

nario whereby kink-mode waves generated in the photospheric network may travel up through the chromosphere, before coupling with saugage-mode waves. The extended tail of the network oscillations in Figure 6.6 may be the oscillatory signature of the kink-mode wave at P = 534 s ($\log_{10}(P)$ = 2.73). In the 1216 Å and 1550 Å passbands this tail is less evident, hence these waves may have coupled in the high chromosphere.

Figure 6.7 repeats the comparison of the wavelet analysis and classical Fourier approaches of Figure 6.5, but applied to the network data. Figure 6.7 displays a rise of power (Fourier) and occurrence rate (wavelet) with increasing period, reaching a maximum around $\log_{10}(P)$ = 2.45 ($P \sim$ 280 s). The two curves reach a minimum around $\log_{10}(P)$ = 2.6 ($P \sim$ 400 s), followed by a gradual increase. Again the fall-off at $\log_{10}(P) > 3.0$ is due to the high-pass filter performed on the light curves.

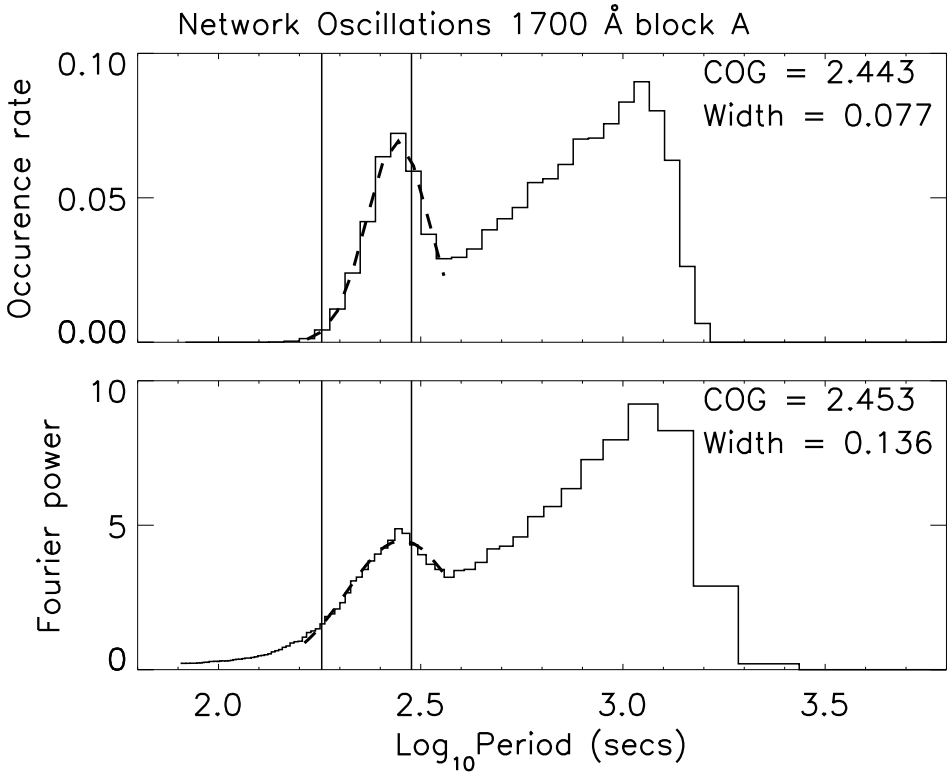

Figure 6.7: Network occurrence rate and Fourier power in the 1700 Å block A dataset. Top: occurrence rate per pixel at each period. Bottom: Average Fourier power per pixel at each period. In both diagrams, a Gaussian fit is applied to the feature around $\log_{10}(P) = 2.4$, and the centre of this Gaussian fit is displayed at the top right.

6.4.3 Oscillation Recurrence

By comparing how many pixels in block A of each wavelength display a similar behaviour in block B, it is possible to study whether oscillations of specific period and lifetime occur repeatedly (Table 6.2). At each wavelength all network pixels displaying periodicity between 230–280 s in block A were selected and compared to network pixels containing periodicity in the same range in block B. This showed a recurrence rate of ∼65–75% in all four UV passbands. This was also carried out for all network pixels displaying oscillations lasting 2–3 cycles at all periods (where the corresponding value was ∼75–85%). A study of all network pixels lasting 2–3 cycles *and* in the range 230–280 s (i.e., at the peak value in the lifetime-period plots), showed ∼40% common pixels. As these oscillations are the most frequent, a 40% chance of a recurrence at the same position represents a good candidate for repeated heating of the surrounding

plasma.

In the internetwork, the fraction of pixels showing oscillations recurring in the same location was generally 5–10% higher than in the network (Table 6.3). The internetwork oscillations lasting 2–3 cycles *and* in the range 230–280 s (with a $\sim$50% recurrence rate) may be the persistent flashers first identified by Brandt *et al.* (1992). However their studies suggest grains which are persistent flashers should be 5-10 times less likely to occur than normal K_{2V} grains, which in turn suggests a recurrence rate of $\sim$10–17%. The higher value of 50% obtained in these data could be due to the internetwork mask preferentially containing persistent flashers rather than normal internetwork grains.

6.4.4 Long Lifetime Oscillations

During each cycle, a wave may transfer a portion of its energy to the surroundings. Hence, any long-lifetime oscillations, which undergo several complete cycles, are good candidates for chromospheric heating. In all the UV passbands, in both the network and internetwork, all the LLOs occur near the acoustic band. At longer periods, oscillations tend to last for fewer cycles, and are even more transient at shorter periods. These LLOs never recur in the same place in both blocks of the data (Tables 6.2 & 6.3). This suggests that the source, in driving the LLO, no longer has sufficient energy to create further oscillations (or if it does create further oscillations, they will be too weak or have short lifetimes, hence will not be detected). Of course it may be that LLOs do recur, but more than 111 minutes (167×40.05 s) apart. It is also noted that the lower HOF passbands (1700 Å,1600 Å) contain more LLOs than the upper passbands, and whereas 1.5–2.0% of network pixels contains LLOs, only 0.05% of internetwork pixels display LLOs. Further studies of more LLOs are necessary to confirm these effects.

Table 6.2: Recurrence rates for network pixels (total 5999)

Selection	Block A		Block B		Both Blocks		
Criteria	**No. pixels**	% of total	**No. pixels**	% of total	**No. pixels**	% of A	% of B
1700Å							
LLO	**64**	1	**103**	2	**0**	-	-
2–3 cycles	**4857**	81	**4611**	77	**3754**	77	81
230-280 s & 2–3 cycles	**2090**	35	**2215**	37	**818**	39	37
230-280 s	**3868**	64	**4138**	69	**2709**	65	70
1600Å							
LLO	**142**	2	**93**	2	**2**	1	2
2–3 cycles	**4637**	77	**4913**	82	**3812**	82	78
230–280 s& 2–3 cycles	**2430**	41	**2337**	39	**961**	40	41
230-280 s	**4587**	76	**4465**	74	**3429**	75	77
1216Å							
LLO	**134**	2	**123**	2	**4**	3	3
2–3 cycles	**5173**	86	**5126**	85	**4370**	85	84
230–280 s& 2–3 cycles	**2537**	42	**2440**	41	**1024**	40	41
230-280 s	**4727**	79	**4515**	75	**3584**	76	79
1550Å							
LLO	**131**	2	**50**	1	**0**	-	-
2–3 cycles	**4704**	78	**3516**	59	**2085**	44	59
230–280 s& 2–3 cycles	**2470**	41	**1591**	27	**679**	27	43
230-280 s	**4560**	76	**3051**	51	**2324**	51	76

Table 6.3: Recurrence rates for internetwork pixels (total 28717)

Selection	Block A		Block B		Both Blocks		
Criteria	No. pixels	% of total	No. pixels	% of total	No. pixels	% of A	% of B
1700Å							
LLO	**642**	2	**613**	2	**15**	1	1
2–3 cycles	**24370**	85	**26427**	92	**22420**	85	92
230–280 s & 2–3 cycles	**13709**	48	**14518**	51	**6990**	51	48
230-280 s	**23871**	83	**25084**	87	**20866**	87	83
1600Å							
LLO	**618**	2	**716**	2	**18**	1	1
2–3 cycles	**24078**	83	**26220**	91	**21994**	91	84
230–280 s & 2–3 cycles	**13240**	46	**13826**	48	**6337**	48	46
230-280 s	**23380**	81	**24640**	86	**20059**	86	81
1216Å							
LLO	**777**	3	**836**	3	**19**	1	1
2–3 cycles	**26421**	92	**26334**	92	**24248**	92	92
230–280 s & 2–3 cycles	**14499**	50	**14594**	51	**7418**	51	51
230-280 s	**25355**	88	**25318**	88	**22364**	88	88
1550Å							
LLO	**462**	2	**161**	1	**2**	1	1
2–3 cycles	**23675**	82	**15763**	55	**12985**	55	82
230–280 s & 2–3 cycles	**12592**	44	**8128**	28	**3564**	28	44
230-280 s	**22245**	77	**14764**	51	**11457**	52	78

Table 6.4: Centres and one sigma widths (both in $\log_{10}$ seconds) of the Gaussian fits to the occurrence rate and Fourier power curves for the first half (block A) and second half (block B) in each bandpass.

Wavelength	Network				Internetwork			
Dataset	Wavelet		Fourier		Wavelet		Fourier	
	Centre	Width	Centre	Width	Centre	Width	Centre	Width
1550 A	2.441	0.080	2.460	0.141	2.391	0.089	2.408	0.143
1216 A	2.457	0.084	2.462	0.127	2.413	0.093	2.421	0.136
1600 A	2.440	0.081	2.452	0.135	2.391	0.084	2.407	0.136
1700 A	2.443	0.077	2.453	0.136	2.393	0.082	2.408	0.131
1550 B	2.455	0.089	2.479	0.166	2.401	0.088	2.435	0.166
1216 B	2.464	0.090	2.473	0.136	2.414	0.092	2.421	0.137
1600 B	2.453	0.098	2.470	0.140	2.406	0.096	2.422	0.143
1700 B	2.457	0.100	2.563	0.141	2.409	0.093	2.419	0.137
Average	2.451±0.087		2.464±0.140		2.402±0.090		2.418±0.141	

6.4.5 Network - Internetwork Comparison

From a comparison of the network and internetwork results in all passbands, a few common themes are apparent. As often confirmed before, the network tends to oscillate with a period close to 5 min. The internetwork, whilst exhibiting many more oscillations around 3 min, contains a peak close to 4 min. Table 6.4 contains a list of the centre of the Gaussian fits and one sigma widths for the Fourier and wavelet approaches. The calculated averages of the COGs for the Fourier and wavelet approaches agree within the one sigma widths and both regions contain a wide range of periodicities. The widths are typically larger in the Fourier than the wavelet approach, but in both cases a range of $\sim \log_{10}(P)$ = 2.1–2.6 is fitted (2.5–7.9 mHz; other work (e.g., Lites *et al.* 1999; McIntosh *et al.* 2003) sums over 3–8 mHz). This periodicity range is important to remember when using the 3- and 5- min oscillations in modelling.

The power of the dominant oscillations in each region was studied using several different methods. Table 6.5 contains a summary of the occurrence rate of the peak periodicity in both the lifetime-period diagrams (e.g., Figures 6.4 and 6.6) and the centre of the Gaussian fits to the average occurrence rate and Fourier power diagrams (e.g., Figures 6.5 and 6.7) in all passbands. It is immediately apparent that the results from

Table 6.5: Frequency of occurrence of the most common oscillation (lifetime-period plots), and peak of the Gaussian fit for occurrence rate and Fourier Power of oscillations in the network (NWK) and the internetwork (INWK) for the first half (block A) and second half (block B) in each bandpass. Columns are numbered (2–7) for ease of reference to the text in Section 6.4.5

	Most Common Osc.		Peak of Gaussian Fit			
Wavelength	Occurrence Rate		Occurrence Rate		Fourier Power	
Dataset	NWK(2)	INWK(3)	NWK(4)	INWK(5)	NWK(6)	INWK(7)
1550 A	0.212	0.229	0.081	0.073	4.80	4.89
1216 A	0.217	0.257	0.086	0.098	4.61	5.12
1600 A	0.206	0.246	0.079	0.085	4.82	5.15
1700 A	0.188	0.260	0.070	0.090	4.47	5.30
1550 B	0.120	0.138	0.043	0.041	4.33	4.24
1216 B	0.197	0.254	0.079	0.099	4.55	5.13
1600 B	0.179	0.241	0.071	0.088	4.48	4.86
1700 B	0.161	0.259	0.058	0.092	3.96	5.02

the second half of the 1550 Å dataset (1550 B) display very low values in both the network and internetwork. These low values may be due to the larger number of saturated pixels, dropped data and streaks in this part of the dataset. Hence for the following interpretation, the 1550 B dataset is ignored.

For the network, the lifetime-period approach (column 2) shows an increasing occurrence rate with increasing HOF from 1700 Å through 1600 Å to 1216 Å. It then decreases in 1550 Å. This trend is also prevalent in the values of the peak of the COG fit for the occurrence rate (column 4) and the peak of the COG fit for the Fourier power of data block B (bottom of column 6). This suggests oscillations occurring more frequently, leading to an increase in oscillatory power, as waves move up through the atmosphere to the HOF of the 1216 Å passband. As the number, as well as the total oscillatory power, increases, this suggests that waves are exciting oscillations in neighbouring regions as they propagate through the atmosphere. Before the waves reach the 1550 Å passband HOF several of these oscillations are no longer observed. There are a number of possible explanations for this decrease in both occurrence and power of oscillations:

(i) waves may either shock or damp between the HOF of 1216 Å and 1550 Å;

(ii) at the height where the canopy closes over completely, the magnetic field lines may be almost horizontal, and hence may channel oscillations away from areas defined as network;

(iii) upwardly-propagating acoustic waves near network areas may undergo mode-conversion when interacting with the closing magnetic canopy in the upper chromosphere (Judge *et al.* 2001), hence oscillations will change in frequency.
It is difficult to determine which one, or combination of two or more, of these explanations is correct.

From a comparison of the Fourier and wavelet approaches in Table 6.5 it is clear that the internetwork normally has a higher value of oscillatory power (Fourier) and occurrence rate (wavelet) than the network. For the lifetime-period approach (column 3), the occurrence rate decreases from the 1700 Å HOF to the 1600 Å HOF, then increases at the 1216 Å HOF, and decreases again at the 1550 Å HOF. This trend is repeated in the COG fitting approach (column 5, column 7 bottom). Therefore some waves at the 1700 Å HOF must disappear before the 1600 Å HOF. This agrees with the low-lying shocks in internetwork grain simulations of Carlsson & Stein (1992; 1995; 1997). Above the 1600 Å HOF both long- and short-period waves will produce shocks separated by the acoustic cut-off period (Carlsson & Stein 1992), which may explain the increase at 1216 Å. The subsequent decrease at the 1550 Å HOF may then be due to a decreased number of these oscillations propagating to this height.

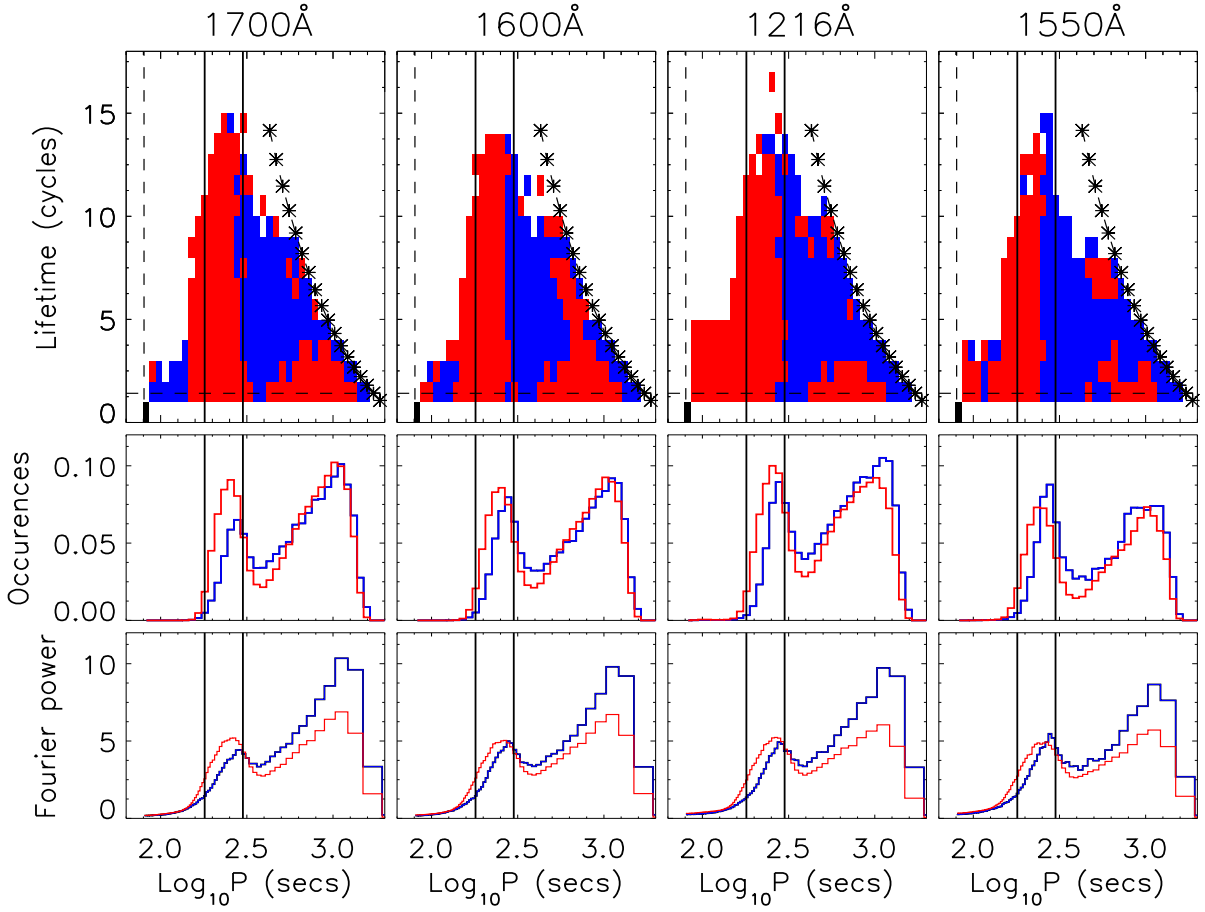

Figure 6.8: Comparison of network (blue) and internetwork (red) oscillations. Rows: Top - Same axis and lines as Figures 6.4 and 6.6. Middle - Average occurrence rate per pixel at each period. Bottom - Average Fourier power per pixel at each period. Columns: Increasing height of formation from left to right; 1700 Å, 1600 Å, 1216 Å, 1550 Å

6.4.6 Network - Internetwork Dominance

Krijger *et al.* (2001) show that the network oscillatory power exceeds that in the internetwork for all frequencies below ∼5 mHz (their Figure 12). The time-localised nature of wavelet analysis can be used to extend this type of study into the temporal domain. In each bandpass, an average network and internetwork lifetime-period diagram was created (i.e., an average of block A and block B, except in 1550 Å where only block A data was used - Section 6.4.5). A comparison diagram was then created by comparing the network occurrence rates to the internetwork occurrence rates at each period and lifetime. Figure 6.8 shows the resulting network / internetwork comparison for all datasets. In each column, the top part has the same axes and lines as Figure 6.4 (also Figure 6.6). Blue parts of the top row of Figure 6.8 refer to where the network has a greater occurrence rate, whereas red parts refer to where the internetwork dominates. The middle and bottom row of Figure 6.8 are directly comparable to Figures 6.5 and 6.7. In these plots, the blue lines refers to network data, and the red lines to internetwork. It is clear from the middle and bottom rows that the network has greater oscillatory power at all periods longer than $\log_{10}(P)$ = 2.45 ($P \sim$ 280 s; 3.6 mHz). There is also a tendency for this cross-over period to decrease with increasing HOF (from ∼300 s in 1700 Å to ∼250 s in 1550 Å). However the top row in Figure 6.8 displays a further feature. If the network dominates for all lifetimes at periods above $\log_{10}(P)$ = 2.45, then the resulting plots in the top row should be entirely blue to the right of this cross-over, and entirely red to the left of this cross-over. Instead there are regions of internetwork domination above $\log_{10}(P)$ = 2.45 for a small number of cycles. This mixing is more prevalent in the 1700 Å and 1600 Å data than for the 1216 Å and 1550 Å, suggesting these short-lifetime, long-period internetwork oscillations are most likely a low-chromosphere phenomenon. There is also some mixing at short periods, which may be examined further by using a higher-cadence dataset.

6.5 Conclusions

A new automated wavelet analysis approach (based on an original idea in Ireland *et al.* 1999) to *TRACE* quiet-Sun UV data is presented. This permits the extension of previous Fourier analysis into the time-localised domain. The resulting occurrence rate at specific periods and lifetimes is directly comparable to the results of the classical Fourier approach. The important results are,

• The network is found to have a peak occurrence rate periodicity of $\log_{10}(P)$ = 2.451 $\pm$ 0.087 (P = 231–346 s) for a lifetime of 2–3 cycles, with a significant tail of higher-period oscillations, while the internetwork is found to have a well-defined peak occurrence rate periodicity of $\log_{10}(P)$ = 2.402 $\pm$ 0.090 (P = 205–309 s) for a lifetime of 2–3 cycles.

• Both the network and internetwork show a number of long-lifetime oscillations, however these do not seem to recur in the same location. Consequently the driver may have exhausted its energy in generating the LLO.

• On the other hand, oscillations at 230–280 s, and/or 2–3 cycles, show a tendency to recur at the same spatial position. These are considered good candidates for chromospheric heating.

• Network oscillations show an increase in occurrence rate and oscillatory power with increasing HOF from 1700 Å to 1216 Å, possibly as a result of the opening up of the canopy at higher altitudes. In the 1550 Å passband there is a marked decrease in both occurrence rate and oscillatory power, suggesting that any possible waves may have either dissipated, shocked, moved away from the network or changed in frequency. The network also contains more oscillations around 534 s in the lower HOF than upper HOF passbands, which agrees with the MHD model of Hasan & Kalkofen (1999).

• In the internetwork there is a decrease in occurrence rate from 1700 Å to 1600 Å. Hence, some oscillations seem unable to propagate past the low chromosphere. However, the increase at 1216 Å and subsequent decrease at 1550 Å suggests that some waves which do propagate through the low-chromosphere may once again excite further oscillations, before disappearing higher in the atmosphere.

• A comparison of the occurrence rate of oscillations in the network and internetwork shows that although the network generally dominates at periods greater than 300 s, for a small number of cycles and long periods the internetwork may dominate. Similarly, regions of network dominance may be found at very short periods (and low lifetimes) where Fourier analysis shows internetwork oscillations to dominate.

Chapter 7

Concluding Remarks and Future Work

This thesis has concentrated on the detections of low-frequency (1–8 mHz) oscillations in the chromosphere, and the possible role of these oscillations in solving the chromospheric heating problem. This chapter will summarise the main results of the work carried out for this thesis and suggest possible extensions of each study.

7.1 Optical Datasets

Chapters 4 & 5 discussed the detection and evolution of oscillations in NBPs in three dimensions - two spatial and one temporal. The importance of separating the NBP contribution from that of the internetwork and other non-solar sources is addressed using a contour and contrast method. The *contour* ensures only NBP pixels are studied, whereas the *contrast* ensures that only intensity oscillations above that of the background are included. A study of oscillatory power against radial distance showed that oscillations in the 1–4 mHz range are much stronger in the centre of NBPs.

The need for high-cadence, two-dimensional images for this type of study shows the importance of using narrow-band optical filters on ground-based telescopes. Space-based telescopes suffer from the fact that high-cadence imaging will be necessarily combined with short duration sequences and a problem of telemetry rate in transferring the data. Ground-based are also cheaper to run, and easier to upgrade. Recent post-acquisition software also makes it possible to remove a lot of seeing effects from the data.

7.1.1 Mode-Coupling in the Network

Chapter 5 extended the radial study of intensity oscillations in NBPs into the time-domain via wavelet analysis, and throughout the atmosphere using multi-wavelength imaging. A cross-correlation study of *oscillatory power curves* between light curves in four wavelengths showed the existence of many upward- and downward- propagating

waves throughout the chromosphere. In particular, each NBP displayed propagating waves which satisfied observational tests predicted by theory. In each case a low-frequency wave (1.3 mHz, 1.9 mHz) travelled from the low- to mid- chromosphere. This is taken to be the signature of a kink-mode wave created by granular buffeting of magnetic flux tubes in the photosphere. In the higher chromosphere, higher frequency travelling waves are detected, and the low- frequency oscillations decrease in power. This agrees with the theoretical studies of Kalkofen (1997) and Hasan & Kalkofen (1999), whereby the low-frequency kink mode waves transfer their power to longitudinal mode waves at twice the original frequency of the kink-mode waves. These longitudinal waves can then shock, hence heating the surrounding plasma.

There are two main extensions to this work. Firstly co-temporal and co-spatial magnetic field information needs to be combined with a larger spatial sample of NBPs. It is believed that both the speed of the wave and frequency of oscillation will be directly influenced by the magnetic field strength. Indeed a subtle change in magnetic field may coincide with the initiation of a wave in a flux tube. Secondly the errors in the estimated velocities of these waves can be greatly reduced by observational and theoretical studies. Observationally, higher-cadence imaging provides better temporal constraints, and improved narrowband imaging provides a better estimate to the height of formation of the data. Theoretically a better understanding of the emission of the strong Fraunhofer lines in the presence of kilogauss magnetic field will also reduce the error in the estimated height of formation. A larger spatial sample of NBPs will also provide further evidence as to the global significance of these oscillations.

7.1.2 Spectroscopy

Spectroscopy of quiet-Sun regions may be one solution to the problems mentioned above. Although spectroscopy requires a scan across an area to make an image, this can be neglected by using a sit and stare study, and provides information at a range of

heights throughout the chromosphere. There is also the possibility of confirming the presence of waves via the Doppler shift of the line profile. It is also well known that many oscillations are stronger in a study of the Doppler shift, rather than the intensity of the line. Ideally a combined spectroscopic and imaging campaign, with high resolution magnetograms, and involving support from CDS and *TRACE* would provide a definitive dataset. With the onset of solar minimum over the next few years it will be easier to select in advance a quiet target region, far from active regions.

7.2 Automated Wavelet Analysis

Chapter 6 presents an automated wavelet analysis approach to searching for oscillations in intensity in a large number of light curves from both the network and internetwork. This permits a comparison study, in terms of both periodicity and lifetime, of oscillations present in these two regions of the quiet Sun. The network displays a higher peak periodicity ($\sim$280 s) than the internetwork ($\sim$250 s). In the lower chromosphere the network also displays a large number of oscillations at higher periods, which may be the signature of kink-mode waves. In both regions, oscillations around these peak values (and with a lifetime of 2–3 cycles) show a tendency to recur in the same spatial position, suggesting a good degree of spatial memory. On the other hand, oscillations with a long lifetime ($>$8 cycles) do not recur, suggesting the driving source may be expending all its energy in the creation of the initial oscillation.

A study of oscillations in each UV passband shows upwardly-propagating waves in both the network and internetwork. The sudden decrease in oscillation strength (and number) in the 1550 Å band is attributed to waves dissipating, shocking or moving away in the high chromosphere. The cross-over period (i.e., the minimum period at which the network exhibits more oscillatory power than the internetwork) is shown to increase from $\sim$250 s in the low chromosphere to $\sim$300 s in the high chromosphere. The time-localised nature of wavelet analysis is used to show that even in these high-

period regimes the internetwork can still exhibit more oscillatory power, but only for oscillations with short lifetimes.

A study into the spatial position of pixels displaying different periodicities and lifetimes may answer some of the questions posed in this chapter. It may be useful to apply this method to higher cadence *TRACE* quiet-Sun datasets and other instruments. It can also be extended into a third spatial region between the network and internetwork (classified as 'intermediate' in Krijger *et al.* 2001). In a wider context, this technique can be used in other areas of solar physics (e.g., active regions) or astronomy in general where a search for transient, spatially-localised, oscillatory power is required (e.g., multi-target wide-field imaging).

The automated aspect of the wavelet analysis in Chapter 6 is worth discussing. With the large datasets expected from future space missions (e.g., Solar Dynamics Observatory may produce up to 1 terabyte per day), it will impossible to manually inspect every light curve for periodicity. Automated routines must be created to filter through datasets and detect interesting features. In this respect an automated search for both periodicity and possible propagating waves is essential. A search for horizontal flows can also be carried out by detecting the starting time of any oscillations. This may make near real-time detections of solar phenomena a possibility.

References

Al, N., Bendlin, C., & Kneer, F. 1998, *A&A*, **336**, 743

Alfvén, H. 1943, *Ark. F. Mat. Ast. Fys.*, **29A**, 1

Ayres, T. R. 1981, *ApJ*, **244**, 1064

Banerjee, D., O'Shea, E., Doyle, J. G., & Goossens, M. 2001, *A&A*, **371**, 1137

Baudin, F., Bocchialini, K., & Koutchmy, S. 1996, *A&A*, **314**, L9

Beck, R. J., Duvall Jn. T. L., & Scherrer P. H. 1998, *Nature*, **394**, 653

Beckers, J. M., Dickson, L., & Joyce, R. S. 1975, Instrumentation Papers No. 227, Air Force Cambridge Research Laboratories, Massachusetts

Berger, T. E., Löfdahl, M. G., Shine, R. S., & Title, A. M. 1998, *ApJ*, **495**, 973

Bird, G. A. 1964, *ApJ*, **140**, 288

Bocchialini, K., & Baudin, F. 1995, *A&A*, **299**, 893

Bocchialini, K., Vial, J.-C., & Koutchmy, S. 1994, *ApJ*, **423**, L67

Bogdan, T. J., Carlsson, M., Hansteen, V., McNurry, A., Rosenthal, C. S., Johnson, M., Petty-Powell, S., Zita, E. J., Stein, R. F., McIntosh, S. W., & Nordlund, A. 2003, *ApJ*, in press

Bonaccini, D., Righini, A., Cavalline, F., & Ceppatelli, G. 1989, *A&A*, **217**, 368

Bohr, N. 1913 *I. Phil. Mag.*, **26**, 1

Brandt, P. N., Rutten, R. J., Shine, R. A., & Trujillo Bueno, T. 1992, in ASP Conf. Ser. **26**, *7th Cambridge Workshop on Cool Stars, Stellar Systems, and the Sun*, eds M. S. Gaimpapa & J. A. Bookbinder (San Francisco: ASP) 161

Brueckner, G. E., Howard, R. A., Koomen, M. J., Korendyke, C. M., Michels, D. J., Moses, J. D., Socker, D. G., Dere, K. P., Lamy, P. L., Llebaria, A., Bout, M. V., Schwenn, R., Simnett, G. M., Bedford, D. K., & Eyles, C. J. 1995, *Sol. Phys.*, **162**, 357

Carlsson, M., & Stein, R. F. 1992, *ApJ*, **397**, L59

Carlsson, M., & Stein, R. F. 1995, *ApJ*, **440**, L29

Carlsson, M., & Stein, R. F. 1997, *ApJ*, **481**, 500

Cauzzi, G., Falchi, A., & Falciani, R. 2000, *A&A*, **357**, 1090

Choudhuri, A. R. 1998, *The Physics of Fluids and Plasmas*, (Cambridge: Cambridge University Press)

Choudhuri, A. R., Auffret, H., & Priest E. R. 1993, *Sol. Phys.*, **143**, 49

Choudhuri, A. R., Dikpati, M., & Banerjee, D. 1993, *ApJ*, **413**, 811

Curdt, W., & Heinzel, P. 1998, *ApJ*, **503**, L95

Damé L., Gouttebroze, P., & Malherbe, J.-M. 1984, *A&A*, **130**, 331

Deubner, F.-L., & Fleck, B. 1990, *A&A*, **228**, 506

Deubner, F.-L., Waldschik, Th., & Steffens, S. 1996, *A&A*, **307**, 936

Einstein, A. 1905, *Annalen der Physik.*, **17**, 132

Edlén, B. 1942, *Zeitschr. f. Astrophys.*, **22**, 30

Erdélyi, A. 1954, *Table of Integral Transforms* Vol. 1, (New York: McGraw-Hill)

Farge, M. 1992, *Annu. Rev. Fluid Mechanics*, **24**, 395

Fleck, B., Domingo, V., & Poland, A. I. 1995, *The SoHO Mission*, (Dordrecht: Kluwer)

Fontenla, J. M., Avrett, E. H., & Loeser, R. 1993, *ApJ*, **406**, 319

Fraunhoffer, J. 1817, *Denkschriften der Müch. Akademie der Wissenchaften*, **5**, 193

Freeland, S. L., & Handy, B. N. 1998, *Sol. Phys.*, **182**, 497

Gallagher, P. T., Phillips, K. J. H., Harra-Murnion, L. K., Baudin, F., & Keenan, F. P. 1999, *A&A*, **348**, 257

Goodman, L. M. 2000, *ApJ*, **533**, 501

Grotian, W. 1939, *Naturwiss.*, **27**, 214

Gustafsson, B., & Jorgensen, U. G. 1994, *A&AR*, **6**, 19

Hagenaar, H. J., Schrijver, C. J., & Title, A. M. 1997, *ApJ*, **481**, 988

Hagenaar, H. J., Schrijver, C. J., Title, A. M., & Shine, R. A. 1999, *ApJ*, **511**, 932

Handy, B. N., Acton, L. W., Kankelborg, C. C., Wolfson, C. J., Akin, D. J., Bruner, M. E., Caravalho, R., Catura, R. C., Chevalier, R., Duncan, D. W., Edwards, C. G., Feinstein, C. N., Freeland, S. L., Friedlaender, F. M., Hoffmann, C. H., Hurlburt, N. E., Jurcevich, B. K., Katz, N. L., Kelly, G. A., Lemen, J. R., Levay, M., Lindgren, R. W., Mathur, D. P., Meyer, S. B., Morrison, S. J., Morrison, M. D., Nightingale, R. W., Pope, T. P., Rehse, R. A., Schrijver, C. J., Shine, R. A., Shing, L., Strong, K. T., Tarbell, T. D., Title, A. M., Torgerson, D. D., Golub, L., Bookbinder, J. A., Caldwell, D., Cheimets, P. N., Davis, W. N., Deluca, E. E., McMullen, R. A., Warren, H. P., Amato, D., Fisher, R., Maldonado, H., & Parkinson, C. 1999a, *Sol. Phys.*, **187**, 229

Handy, B. N., Bruner, M. E., Tarbell, T. D., Title, A. M., Wolfson, C. J., Laforge, M. J., & Oliver, J. J. 1998, *Sol. Phys.*, **183**, 29

Handy, B. N., Tarbell, T. D., Wolfson, C. J., Korendyke, C. M., & Vourlidas, A. 1999b, *Sol. Phys.*, **190**, 351

Hansteen, V. H., Betta, R., & Carlsson, M. 2000, *A&A*, **360**, 742

Hart A. B. 1954, *MNRAS*, **114**, 17

Harrison, R. A., Sawyer, E. C., Carter, M. K., Cruise, A. M., Cutler, R. M., Fludra, A., Hayes, R. W., Kent, B. J., Lang, J., Parker, D. J., Payne, J., Pike, C. D., Peskett, S. C., Richards, A. G., Culhane, J. L., Norman, K., Breeveld, A. A., Breeveld, E. R., Janabi, K. F. Al, McCalden, A. J., Parkinson, J. H., Self, D. G., Thomas, P. D., Poland, A. I., Thomas, R. J., Thompson, W. T., Kjeldseth-Moe, O., Brekke, P., Karud, J., Maltby, P., Aschenbach, B., Brauninger, H., Kuhne, M., Hollandt, J., Siegmund, O. H. W., Huber, M. C. E., Gabriel, A. H., Mason, H. E., & Bromage, B. J. I. 1995, *Sol. Phys.*, **162**, 233

Hasan, S. S., & Kalkofen, W. 1999, *ApJ*, **512**, 899

Hasan, S. S., Kalkofen, W., van Ballegooijen, A. A., & Ulmschneider, P. 2003, *ApJ*, **585**, 1138

Hathaway D. H., Beck J. G., Bogart R. S., Bachmann K. T., Khatri G., Petitto J. M., Han S., & Raymond J. 2000, *Sol . Phys.*, **193**, 299

Holweger, H., & Müller, E. A. 1974, *Sol. Phys.*, **39**, 19

Ireland, J., Walsh, R. W., Harrison, R. A., & Priest, E. R. 1999, *A&A*, **347**, 355

Judge, P. G., Tarbell, T. D., & Wilhelm, K. 2001, *ApJ*, **554**, 424

Kalkofen, W. 1997, *ApJ*, **486**, L145

Kalkofen, W., Ulmschneider, P., & Avrett, E. H. 1999, *ApJ*, **521**, L141

Kariyappa, R. 1994, *Sol. Phys.*, **154**, 19

Keller, C. U., & Koutchmy, S. 1991, *ApJ*, **379**, 751

Kneer, F., Hasan, S. S., & Kalkofen, W. 1996, *A&A*, **305**, 660

Kneer F., & von Uexküll, M. 1985, *A&A*, **144**, 443

Kneer F., & von Uexküll, M. 1986, *A&A*, **155**, 178

Kneer F., & von Uexküll, M. 1993, *A&A*, **274**, 584

Kopp, R. A., & Kuperus, M. 1968, *Sol. Phys.*, **4**, 412

Krijger, J. M., Rutten, R. J., Lites, B. W., Straus, Th., Shine, R. A., & Tarbell, T. D. 2001, *A&A*, **379**, 1052

Krijger, J. M., Heinzel, P., Curdt, W., & Schmidt, W. 2003, *A&A*, in press

Kulaczewski, J. 1992, *A&A*, **261**, 602

Lamb, H. 1909, *Proc. London Math. Soc.*, **7**, 122

Lamb, H. 1932, *Hydrodynamics*, (Cambridge: Cambridge University Press)

Leighton, R. B., Noyes, R. W., & Simon, G .W. 1962, *ApJ*, **135**, 474

Lites, B. W., Rutten, R. J., & Berger, T. E. 1999, *ApJ*, **517**, 1013

Lites, B. W., Rutten, R. J. & Kalkofen, W. 1993, *ApJ*, **414**, 345

Liu, S.-Y. 1974, *ApJ*, **189**, 359

Lou, Y. Q. 1995, *MNRAS*, **274**, L1

Maxwell, J. C. 1873, *A Treatise on Electricity and Magnetism*, (Oxford: Clarendon Press)

McIntosh, S. W., & Judge, P. G. 2001, *ApJ*, **561**, 420

McIntosh, S. W., Fleck, B., & Judge, P. G. 2003, *A&A*, **405**, 769

Muller, R., & Roudier, Th. 1992, *Sol. Phys.*, **141**, 27

Muller, R., & Roudier, Th., Vigneau, J., & Auffret, H. 1994, *A&A*, **283**, 232

Narain, U., & Agarwal, P. 1994, *Bull. Astr. Soc. India*, **22**, 111

Newton, I. 1672, *Phil. Trans. R. Soc.*, **80**, 3075

Newton, I. 1687, *Philosophiae Naturalis Principia Mathematica*

November, L. J., Toomre, J., Gebbie, K.B., & Simon, G.W. 1981, *ApJ*, **245**, L123

Osterbrock, D. E. 1961, *ApJ*, **134**, 347

Parker E. N. 1988, *ApJ*, **330**, 474

Planck, M. V. 1900, *Dtsch. phys. Ges.*, **2**, 202

Phillips K. J. H. 1992, *Guide to the Sun*, (Cambridge: Cambridge University Press)

Priest, E. R. 1982, *Solar Magnetohydrodynamics*, (Dordrecht: D. Reidel)

Priest, E. R., & Forbes, T. G. 2002, *A&AR*, **10**, 313

Roberts, B. 1983, *Sol. Phys.*, **87**, 77

Roberts, B. 2000, *Sol. Phys.*, **193**, 139R

Roberts, B. 2003, in ESA-SP **547**, *Proc. 'SoHO 13: Waves, oscillations and small scale transient events in the solar atmosphere. A joint view of SoHO and TRACE'*, in press

Rosenthal, C. S., Bogdan, T. J., Carlsson, M., Dorch, S. B. F., Hansteen, V., McIntosh, S. W., McMurry, A., Nordlund, Å., Stein, R. F. 2002, *ApJ*, **564**, 508

Roudier, Th., Espagnet, O., Muller, R., & Vigneau, J. 1994, *A&A*, **287**, 982

Roudier, Th., Rieutord, M., Malherbe, J. M., & Vigneau, J. 1999, *A&A*, **349**, 301

Rutten, R. J., & Uitenbroek, H. 1991, *Sol. Phys.*, **134**, 15

Rutten, R. J. 1998, in *Proc. ISSI Workshop 'Solar Composition and its Evolution - from Core to Corona'*, eds. Cl. Fröhlich, M. C. E. Huber, S. Solanki, R. von Steiger, (Dordrecht/Boston/London: Kluwer Academic Publishers), Space Science Rev. **85**, 269

Rutten, R. J. 1999, in ASP Conf. Ser. **184**, *Proc. 3rd Adv. Solar Physics Euroconference*, eds. B. Schmieder, A. Hoffman, & J. Staude (San Francisco: ASP), 181

Scherrer, P. H., Bogart, R. S., Bush, R. I., Hoeksema, J. T., Kosovichev, A. G., Schou, J., Rosenberg, W., Springer, L., Tarbell, T. D., Title, A., Wolfson, C. J., Zayer, I., & MDI Engineering Team 1995, *Sol. Phys.*, **162**, 129

Schmieder, B. 1979, *A&A*, **74**, 273

Schmieder, B. 2001 in *Encyclopedia of Astronomy and Astrophysics*, (Bristol & Hampshire: Nature Publishing Group & Institute of Physics Publishing)

Schrijver, C. J., Hagenaar, H. J., & Title, A. M. 1997, *ApJ*, **475**, 328

Schrijver, C. J., Title, A. M., Harvey, K. L., Sheeley Jn, N. R., Wang, Y.-M., van den Oord, G. H. J., Shine, R. A., Tarbell, T. D., Hurlburt, N. E. 1998, *Nature*, **394**, 152

Schrijver, C. J., & Title, A. M. 2003, *ApJ*, **597**, L165

Sherrill, T. J. 1991, *S&T*, **81**, 134

Simon, G. 2001 in *Encyclopedia of Astronomy and Astrophysics*, (Bristol & Hampshire: Nature Publishing Group & Institute of Physics Publishing)

Sivaraman, K. R., Gupta, S. S., Livingston, W. C., Damé L., Kalkofen, W., Keller, C. U., Smartt, R., & Hasan, S. S. 2000, *A&A*, **363**, 279

Simon G. W. & Weiss N. O. 1968, *Zeit. Astrophys.*, **69**, 435

Skartlien R., Stein R. F. & Nordlund Å. 2000, *ApJ*, **541**, 468

Spruit, H. C. 1981a, *A&A*, **98**, 155

Spruit, H. C. 1981b, *A&A*, **102**, 129

Spruit, H. C., Nordlund, Å, & Title, A. M. 1990, *ARA&A*, **28**, 263

Spruit, H. C., & Roberts, B. 1983, Nature, 304, 401

Spicer, D. S. 1991, in *Mechanisms of Chromospheric and Coronal Heating*, eds. P. Ulmschneider, E. R. Priest, R. Rosner, (Heidelberg: Springer-Verlag), 547

Stein, R. F., & Leibacher, J. 1974, *ARA&A*, **12**, 407

Torrence, C., & Compo, G. P. 1998, *Bull. Amer. Meteor. Soc.*,**79**, 61

Ulmschneider, P. 1970, *A&A*, **4**, 144

Ulmschneider, P., Zähringer, K., & Musielak, Z. E. 1991, *A&A*, **241**, 625

Vernazza, J. E., Avrett, E. H., & Loeser, R. 1981, *ApJ*, **45**, 635

von Uexküll, M., Kneer F., Malherbe, J. M., & Mein, P. 1989, *A&A*, **208**, 290

Wollaston, W. H. 1802, *Phil. Trans. R. Soc.*, **92**, 365.

Wilhelm, K., Curdt, W., Marsch, E., Schühe, U., Lemaire, P., Gabriel, W., Vial, J.-C., Grewing, M., Huber, M. C. E., Jordan, S. D., Poland, A. I., Thomas, R. J., Kúhne, M., Timothy, J. G., Hassler, D. M., & Siegmund, O. H. W. 1995, *Sol. Phys.*, **162**, 189

Wikstøl, O., Hansteen, V. H., Carlsson, M., & Judge, P. G. 2000, *ApJ*, **531**, 1150

Worden, J., Harvey, J., & Shine, R. 1999, *ApJ*, **523**, 450

Zhugzhda, Y. D., Bromm V., & Ulmscheider P. 1995, *A&A*, **300**, 302

Zirin H. 1966, *The Solar Atmosphere*, (Waltham, Toronto, & London: Blaisdell Publishing Company)